COLLOIDAL MANIPULATION OF NANOSTRUCTURES:

STABLE DISPERSION AND SELF-ASSEMBLY

A Dissertation

by

DAZHI SUN

Submitted to the Office of Graduate Studies of
Texas A&M University
in partial fulfillment of the requirements for the degree of

DOCTOR OF PHILOSOPHY

May 2009

Major Subject: Materials Science and Engineering

COLLOIDAL MANIPULATION OF NANOSTRUCTURES:

STABLE DISPERSION AND SELF-ASSEMBLY

A Dissertation

by

DAZHI SUN

Submitted to the Office of Graduate Studies of
Texas A&M University
in partial fulfillment of the requirements for the degree of

DOCTOR OF PHILOSOPHY

Approved by:

Chair of Committee,	Hung-Jue Sue
Committee Members,	Xing Cheng
	Zhengdong Cheng
	Winfried Teizer
Chair of Intercollegiate Faculty	Tahir Cagin

May 2009

Major Subject: Materials Science and Engineering

ABSTRACT

Colloidal Manipulation of Nanostructures: Stable Dispersion

and Self-assembly. (May 2009)

Dazhi Sun, B.S., Tsinghua University;

M.E., Tsinghua University

Chair of Advisory Committee: Dr. Hung-Jue Sue

This dissertation work addresses two important aspects of nanotechnology – **stable dispersion** and **self-assembly** of colloidal nanostructures. Three distinctly different types of nano-scaled materials have been studied: 0-dimensional ZnO quantum dots (QDs), 1-dimensional carbon nanotubes (CNTs), and 2-dimensional α-zirconium phosphate (ZrP) nanoplatelets. Specifically, highly crystalline ZrP layered compounds with differences in diameters have been synthesized and fully exfoliated into monolayer platelets with uniform thickness, followed by their self-assembly into liquid crystalline structures, *i.e., nematic and smectic*. A novel colloidal approach to debundle and disperse CNTs has been developed by utilizing nanoplatelets to gather and concentrate sonication energy onto nanotube bundles. In such a fashion, CNTs are fully exfoliated into individual tubes through physical means to preserve their exceptional physical properties. Moreover, monodisperse ZnO QDs with high purity have been synthesized through a simple colloidal approach. Exfoliated ZrP nanoplatelets are used to tune the dispersion of ligand-free ZnO QDs from micron-sized aggregates to an individual QD

level depending on the ratio between nanoplatelets and QDs. Dynamic analysis suggests that the dispersion mechanism mainly involves the change of QD dispersion free energy due to the presence of nanoplatelets, so that QDs can interact favorably with the surrounding media. In addition, the nanoplatelet-assisted dispersion approach has been utilized to disperse QDs and CNTs into polymeric matrices. Dispersion – property relationship in polymer nanocomposites has been systematically investigated with emphasis on optical properties for QDs and mechanical properties for CNTs.

ACKNOWLEDGEMENTS

TABLE OF CONTENTS

LIST OF FIGURES

FIGURE   Page

FIGURE   Page

FIGURE   Page

FIGURE   Page

LIST OF TABLES

CHAPTER I

INTRODUCTION

1. 1.   Background

Solution-based manipulation of materials is not only an important route for low-cost material and device fabrications, but also crucial to understanding of many fundamental phenomena, such as colloidal dispersion, aggregation, phase transition, crystal growth, etc. Colloidal manipulation of nano-scaled materials has gained enormous attention since the advent of nanotechnology. Through careful study of nano-colloids, new physics and chemistry at nano-scale have been discovered *[1-6]*; many types of novel nanomaterials have since been synthesized *[7-15]* and various nanomaterial-based devices have been fabricated *[16-27]*.

Based on their geometry, nanomaterials can be categorized as (**i**) simple nanostructures, such as (**a**) zero dimensional (0-D) quantum dots and nanoparticles, (**b**) one dimensional (1-D) nanorods, nanowires, and nanotubes, and (**c**) two dimensional (2-D) inorganic nanoplatelets, and (**ii**) complex nanostructures such as nano-scaled tetrapods and hyperbranches. Simple structured nanomaterials have been well studied and can be used as a model to understand many nano-scaled phenomena.

Among the vast variety of simple nanostructured materials, three representative nanostructures have been chosen for the current study: 0-D ZnO quantum dots (QDs), 1-D carbon nanotubes (CNT), and 2-D α-zirconium phosphate (ZrP) nanoplatelets.

_____

This dissertation follows the style of *Small*.

1. 2.   Colloidal Quantum Dots

Quantum dots (QDs) are semiconductor crystals with size ranging from 1 − 10 nanometers. They are normally made from the elements in the columns II and VI or III and V in the periodic table of elements, i.e., CdSe, CdS, ZnO, InP, InAs, etc. The most distinguished feature of QDs is that they exhibit size-dependent properties, that is, their properties especially optical and electronic properties vary with their sizes, also known as quantum size effects *[28]*. Since the properties of the bulk materials usually are not a function of their size, this unique size effect opens up a promising way to control the desired properties by using only one type of material. Therefore, in the past decade, extensive research efforts have been made to understand the fundamentals of QDs and their potential applications *[2, 6, 8, 29-41]*.

QDs can be synthesized by many methods, such as chemical vapor deposition (CVD) *[42]*, physical vapor deposition (PVD) *[43]*, and solution-based approaches. Colloidal synthesis has been a major method to prepare QDs because it is simple, low-cost, and reproducible. The size and size distribution of colloidal QDs can be well controlled by managing the experimental conditions, such as reaction time, reagent concentrations, surfactants and temperature *[7, 8, 44, 45]*. Moreover, colloidal QDs are also an important type of building blocks for fabricating many devices *[46, 47]*.

The stable dispersion of QDs in various solvents and polymers is not only important to control their structural uniformity but also crucial in realizing many of their practical applications. For example, dispersing QDs in water and integrating them with bio-molecules offer a promising and viable method to replace organic dyes for bio-

imaging because QDs are much more stable and highly luminescent *[48, 49]*. However, these inorganic nanocrystals tend to form large aggregates without proper functionalization, which dramatically compromises their excellent properties. The current methods to disperse QDs strongly rely on the use of surfactants and ligands, some of which, however, involve complex molecules and are expensive *[50]*. Moreover, when dispersing QDs in polymers, the existence of the surfactants may significantly weaken the matrix properties *[51]*. Therefore, it is desired to disperse QDs without using surfactants and ligands. In this dissertation, a novel colloidal approach to disperse ligand-free ZnO QDs down to an individual level in organic solvents and polymers is introduced. The dispersion − property relationship in polymer/QD nanocomposites is studied.

1. 3.   Colloidal Carbon Nanotubes

Carbon nanotubes (CNTs) are allotropes of carbon with a cylindrical structure that can have a length-to-diameter ratio larger than 1,000. According to the number of the walls they have, CNTs can be categorized as single-walled nanotubes (SWNTs) and multi-walled nanotubes (MWNTs). These cylindrically arranged carbon supermolecules have extraordinary electrical, mechanical, and thermal properties that make them potentially useful in many areas, such as electronics, optics, sensors, energy storage and harvesting, architectural, biological and aerospace applications *[52-66]*.

CNTs can be produced through arc charge*[67, 68]*, laser ablation*[69]*, CVD*[70]*, etc, but not in solutions. However, dispersing CNTs in solvents is a major step for

processing CNTs and fabricating CNT-based devices. After synthesis, CNTs form large aggregates and entanglements. In the case of SWNTs, small tubes naturally align themselves into large and long "bundles" or "ropes" through strong van der Waals forces *[65]*. These complex aggregate morphologies not only significantly suppress their superior properties but also make the CNT dispersion much more challenging than other particle aggregations *[71]*.

Methods to disperse CNTs mainly include (**i**) physical absorption of surfactants or polymers and (**ii**) covalently bonding functional groups onto CNT side-walls. However, these methods either have an extremely low yield (typically <5%) *[72]* or can severely damage the CNT side-walls so that their physical and mechanical properties are significantly compromised *[73, 74]*. Therefore, methods to disperse CNTs in large-scale without deteriorating CNT properties are highly desirable. In this dissertation, a new colloidal approach has been developed to completely disperse and de-bundle CNTs in aqueous suspensions without noticeable damage to their side-walls. A simple approach to prepare highly exfoliated polymer/CNT nanocomposites that show excellent mechanical properties is also introduced.

1. 4.   Colloidal Inorganic Nanoplatelets

Two-dimensional plate-like inorganic crystals normally have a layered structure where each layer is less than a few nanometers in thickness and above 100 nm to a few micrometers in diameters. In each crystal, the layers stack parallel with each other through secondary bonding such as van der Waals forces or hydrogen bonding while

within each layer, atoms are joined through chemical bonding *[75, 76]*. Inorganic compounds that have the layered plate-like structure include natural clays, synthetic clays, such as liponites, solid acid series $H_nM_nZ_2O_{3n+5}$ (with for example M = Sb, Nb, Ta; Z = P, As; n = 1,3); $H_2MZ_2O_8 \cdot H_2O$ (with for example M = Ti, Zr, Hf, Ge, Sn; Z = P, As), zeolites, layered double hydroxides, and many other mineral species. They have been widely used as ion exchangers, additives, fillers, catalysts, etc.

Studies on the colloidal behaviors of platelet materials can be traced back to one century ago. Among many of their interesting colloidal phenomena, self-assembly of these platelets into ordered structures has gained special attention because they could not only be potentially useful in optics but also help understand many thermodynamic and kinetic issues regarding anisotropic colloids, such as discotic liquid crystal phase transition *[77, 78]*. Due to the high impurity and complicated interactions in the natural clay systems, synthetic inorganic platelets have been suggested to serve as a model system *[79]*. In this dissertation, α-zirconium phosphate, $Zr(HPO_4)_2 \cdot H_2O$ (ZrP), is used as a model to study the self-assembling behaviors of 2-D nanoplatelets. The liquid crystalline phase transition of colloidal nanoplatelets is studied with an emphasis on their uniform thickness and aspect ratio characteristics.

1. 5.   Research Objectives and Significance

The primary objectives of this dissertation are to study the colloidal dispersion of 0-, and 1-D nanomaterials in various solvents and polymers, to understand their dispersion mechanisms, and to investigate the self-assembly phenomena of 2-D

nanoplatelets. The specific objectives include:

a) Exfoliation of pristine layered ZrP nanoplatelets and their self-assembly into liquid crystalline structures.

b) (i) Large-scale de-bundling and dispersion of CNTs with retained physical properties. (ii) Understanding the dispersion mechanisms of 1-D nanomaterials.

c) (i) Colloidal synthesis of monodisperse ZnO QDs and their stable dispersion in solvents and polymeric matrices. (ii) Understanding the QD/nanoparticle dispersion mechanisms.

d) Establish nanomaterial dispersion – property relationships.

ZnO QDs, CNTs, and ZrP nanoplatelets are chosen as model nano-systems because of their well-defined geometries, structural perfection, and chemical stability. The concepts employed in this dissertation can be easily generalized and should have widespread impacts on colloidal science. The accomplishments made in this dissertation would also greatly facilitate the large-scale solution-based processing of nanomaterials for many functional and structural applications.

1. 6.   Dissertation Layout

A brief problem statement and introduction on the dispersion and self-assembly of nanomaterials has been outlined in this chapter. In **Chapter II**, a detailed literature review will be given on the dispersion of QDs and CNTs in solvents and polymers as well as self-assembly of nanoplatelets into liquid crystalline structures.

Chapter III focuses on the self-assembly of 2-D nanoplatelets into ordered structures. ZrP nanoplatelets with different diameters are synthesized and exfoliated into monolayer platelets with various aspect ratios. Self-assembly of colloidal nanoplatelets into liquid crystalline nematic and smectic structures is studied. The liquid crystalline phase behaviors are also investigated.

In **Charter IV**, the dispersion of CNTs including SWNTs and MWNTs in water is studied. By using exfoliated ZrP nanoplatelets, CNTs are easily dispersed down to individual level without damaging the tube side-walls. After the separation of ZrP nanoplatelets, high-quality CNT suspensions are obtained. The mechanism on the CNT dispersion using exfoliated nanoplatelets is also discussed in this chapter.

Based on the nanoplatelet-assisted CNT aqueous dispersion, a simple colloidal method to prepare highly exfoliated polymer/CNT nanocomposites is introduced in **Charter V**. Polymer nanocomposites containing a small amount of well-dispersed CNTs show exceptional modulus and strength without compromising their ductility. A mechanism on the CNT dispersion in polymer matrices is proposed.

In **Chapter VI**, a simple and reproducible colloidal method is used to synthesize highly purified monodisperse ZnO QDs with a particle size of 5.0 nm. ZnO QDs are

characterized by various techniques such as transmission electron microscopy (TEM), UV-vis spectroscopy, X-ray diffraction, etc. The stability of colloidal ZnO QDs in organic solvents is also discussed.

By using exfoliated ZrP nanoplatelets, the dispersion of monodisperse ZnO QDs in organic solvents and polymers is found to be well controlled from micron-sized aggregates, to nano-clusters, and to individual particle level. In **Chapter VII**, this nanoplatelet-assisted QD dispersion is systematically studied by varying nanoplatelet-to-QD ratio, concentrations, and nanoplatelet surface properties, diameters, and exfoliation. A dispersion mechanism based experimental results and theoretical analysis is proposed.

Chapter VIII describes the dispersion – property relationship in polymer/QD nanocomposites. The dispersion of QDs in polymers in controlled by using exfoliated ZrP nanoplatelets. The optical properties of polymer/QDs nanocomposites such as optical absorption and photoluminescence are found to strongly depend on the QD dispersion. The physics behind the observed dispersion-dependent optical properties of polymer/QD nanocomposites is discussed.

Finally in the last chapter (**Chapter IX**), concluding remarks are given, recommendations for further studies are proposed, and references in this dissertation are documented.

CHAPTER II

LITERATURE REVIEW

Stable dispersion of nanomaterials in a desired medium and their self-assembly into ordered structures are both fundamental topics in colloidal science and have gained special interests recently due to the needs for designing functional hybrid composite materials for optics, electronics, and optoelectronics, biological, biomedical and structural applications. Nanoscaled materials generally possess superior physical and mechanical properties over their bulk counterparts. For instance, when the size of semiconductor particles is reduced to a few nanometers, they exhibit enhanced quantum size-/shape-dependent optical and electronic properties *[4]*, which greatly broaden their potential applications. Furthermore, when exfoliated, nanomaterials have extremely high surface-to-volume ratio, resulting in greatly improved transportation properties, mechanical properties, energy conversion efficiency, etc *[28]*. However, the above attractive nanoscaled properties will become significantly suppressed if uncontrolled nanoparticle aggregation takes place. Thus, ability to disperse nanoparticles in a medium of interest is a critical step for the large-scale commercial applications of nanomaterials.

In this chapter, the progress on the dispersion of quantum dots (QDs) and carbon nanotubes (CNTs) in solvents and polymers and the self-assembly of colloidal nanoplatelets into liquid crystalline structures is reviewed.

2.1. Dispersion of QDs

2. 1. 1. Dispersion of QDs in Solvents

QDs are insoluble in solvents. Various surfactants, polymers, ligands, or organic capping agents have been utilized to disperse these inorganic nanocrystals into organic solvents and water. For example, trioctylphosphine oxide (TOPO) is the most common ligand used to stabilize QDs during their synthesis and to disperse QDs in organic media *[8]*. The phophine oxide group is chemically bonded to the QD surface and passivates their surface defects, while the trioctyl group is soluble in many organic solvents. The solubilization of QDs in an aqueous solution is the key for their bio-applications, such as bio-sensors, bio-images, and cytotoxicity *[50]*. Many types of amphiphilic surfactants and ligands have been used and synthesized for this purpose, such as a cross-linked polymer shell *[80]*, triblock copolymers *[41]*, phospholipids *[81]*, mercaptoacetic acid *[49, 82]*, dithiothreitol *[82]*, dihydrolipoic acid *[83]*, oligomeric phosphines *[84]*, cross-linked dendrons *[85]*, and peptides *[86]*, etc. However, many of the above are expensive and need delicate chemistry to synthesize.

2. 1. 2. Dispersion of Quantum Dots in Polymers

Incorporation of inorganic nanocrystals into polymeric matrices to form polymer nanocomposites has been an important research subject in the past ten years because of their potentials for optical, electrical, photovoltaic applications, etc *[18, 24, 87]*. Ability to control good dispersion of nanocrystals in polymers is one of the key challenges to overcome for achieving optimal performance of these organic/inorganic hybrids.

Inevitably, inorganic nanocrystals often possess organophobic surface characteristics, resulting in significant phase segregation through direct mixing, such as melt or solution mixing of non-modified particles in polymers. This phase segregation dramatically hinders commercial applications of the organic/inorganic hybrids *[88]*. For instance, in photovoltaic devices, such as solar cells, when composed of nanocrystals and conjugated polymers, higher power conversion efficiency will usually be attained if a good dispersion of nanocrystals at the percolation concentration is achieved in polymers *[21, 22]*. The physical properties of polymer matrices, such as thermal stability, may be significantly improved by increasing interfacial areas between nanocrystals and polymer matrices *via* good dispersion of nanocrystals *[89, 90]*. It should be noted that highly aggregated nanocrystals in polymers inevitably cause substantial light scattering due to their size and refractive index mismatch, which impedes polymer nanocomposites for optical applications *[91]*.

Extensive research efforts have been devoted to improve the dispersion of inorganic nanocrystals into organic polymers for better performance. This has been done by surface modification of inorganic nanocrystals through organic capping agents, followed by solution mixing with polymers in favorable solvents *[92]*, by *in-situ* polymerization of polymer/inorganic nanocomposites *[93-95]*, or by *in-situ* synthesis of inorganic nanocrystals in polymers *[96, 97]*. Each of the method mentioned above can result in better dispersion of inorganic nanocrystals in polymers than direct melt mixing. However, tunable dispersion of nanocrystals in polymers down to individual particle dispersion has not yet been achieved. Moreover, using organic capping agents will

inevitably add cost to the finial products and may negatively impact the potential performance of the nanocomposites *[89, 98]*. It has been found that electrolytic salts can stabilize colloidal nanocrystals in solvents, which, in turn, may help to achieve better dispersion of nanocrystals in polymers *[99]*. However, the presence of electrolytes may dramatically compromise the physical properties of the polymer matrices, such as photoluminescence and thermal stability*[100]*. Therefore, it is desirable to utilize highly purified nanocrystals for the preparation of polymer nanocomposites with best performance.

2.2. Dispersion of CNTs

Two distinct methods have been utilized to disperse CNTs: (**i**) mechanically breaking CNTs aggregates and (**ii**) altering CNT surface energy. The mechanical method, including high shear mixing and ultrasonication, can break the large CNT aggregates into small segments. However, it can cut CNTs short, thus decreasing their aspect ratio. Due to the lack of thermodynamic stabilization, CNTs will immediately re-aggregate after the removal of mechanical agitation. Moreover, this method is unable to achieve individual dispersion of CNTs, but only macroscopically separating CNT aggregates and bundles. The second method can be sub-categorized into (**a**) physical and (**b**) chemical modifications. Both methods have demonstrated ability to effectively disperse CNTs. Therefore, the current literature review will focus on the above two methods, especially for obtaining individually dispersed single-walled nanotubes (SWNTs).

2. 2. 1. Dispersion of CNTs in Water

Achieving aqueous suspensions of individual CNTs, especially SWNTs, can have tremendous impacts on understanding CNT physical properties and realizing their full potentials in many areas of applications. A classical method to obtain individual SWNTs was developed by the Smalley's group, which can be summarized as ultrasonication-assisted surfactant dispersion, followed by isolation of individual nanotubes through ultracentrifugation *[101]*. In his original paper, an aqueous solution containing sodium dodecyl sulfate (SDS) was first mixed with pristine SWNTs under high-power ultrasonication (ultrasonication probe). Subsequently, the SWNT aqueous solution was centrifuged at > 100,000g for a few hours. After ultracentrifugation, the upper supernatant containing micelles of individual SWNTs (20-30 ppm) was decanted and then characterized, leaving behind the nanotube aggregates, bundles, and impurities remained at the bottom.

Figure 2.1 shows the mechanism of individual nanotube isolation from a bundle with surfactant absorption and the help of ultrasonication *[102]*. The role of the ultrasonication is proposed to provide highly localized shear force on the nanotube bundles. Once the nanotubes at the bundle ends open up, surfactant absorption onto the tube side-walls is facilitated, eventually leading to full exfoliation of individual nanotubes from the bundle.
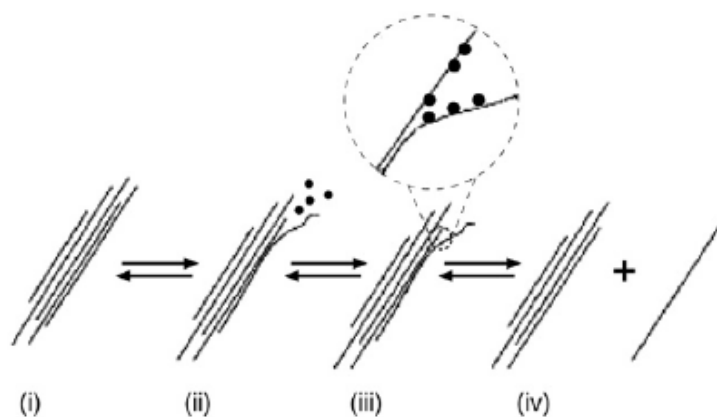
Figure 2.1 Mechanism of nanotube isolation from bundle obtained by ultrasonication and surfactant stabilization. (Reproduced from *[102]*)

Upon the separation of individual SWNTs from non-separated bundles, a micelle structure of surfactant (SDS in this case) coated SWNTs is proposed (Figure 2.2). The micelles containing individual SWNTs have a density similar to water (~1.0 g/mL) while nanotube bundle micelles are heavier (~1.2 g/mL), making the ultracentrifugation separation viable *[101]*.

UV-vis-NIR spectroscopy was performed to characterize individually dispersed and bundled SWNTs (Figure 2.3) *[101]*. The blue-shifted and more pronounced peaks from individual SWNTs are observed due to the disentanglement and de-coupling of tube-tube interaction after dispersion. This spectroscopy-based characterization has been widely adopted to identify individual SWNTs from their bundles. The UV-vis-NIR also demonstrates that the electronic structures of SWNTs are not significantly damaged by this dispersion approach.
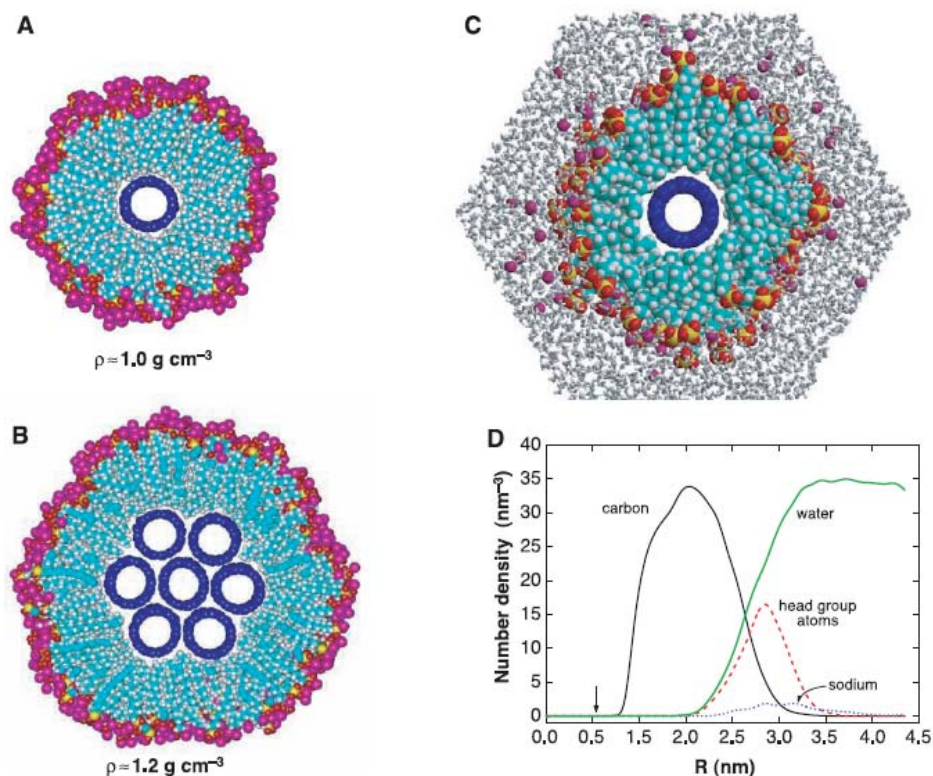
Figure 2.2 Cross-section model of (**A**) an individual fullerene nanotube in a cylindrical SDS micelle and (**B**) a seven-tube bundle of fullerene nanotubes coated by a layer of SDS. The approximate density of these species is 1.0 and 1.2 g/cm^3, respectively. A molecular dynamics simulation of water and the SDS micelle around an individual (8,8) nanotube (**C**) shows the nanotube as it would exist in a water-free hydrocarbon environment. (**D**) The number density profiles for SDS carbon atoms, sulfate head group atoms, water molecules, and sodium ions. The abscissa, R, is measured from the center of the nanotube. The arrow indicates the position of the nanotube wall. (Reproduced from *[101]*)
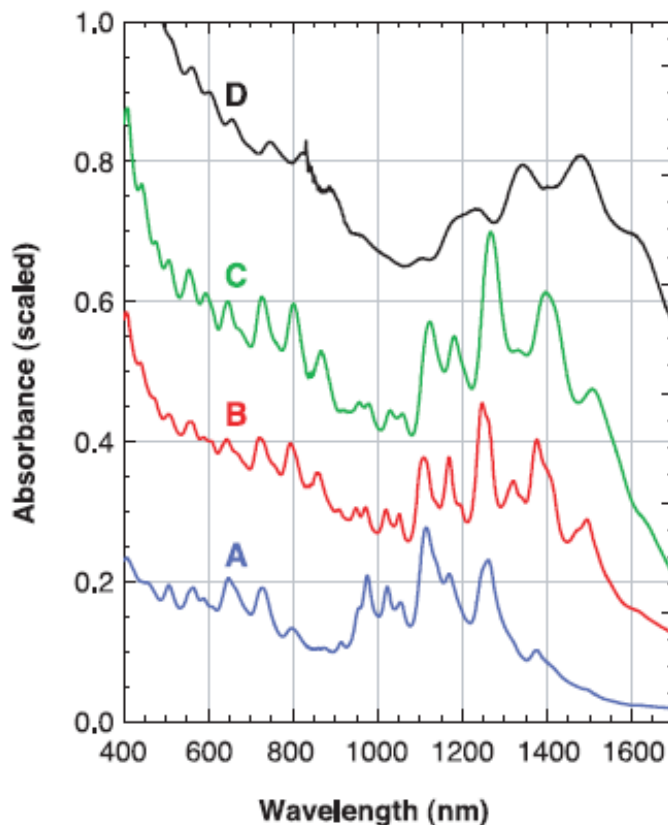
Figure 2.3. SWNT adsorption spectra in aqueous suspensions. Traces A, B and C are from individual nanotubes at different diameters, coated by SDS micelles. The top trace D is the spectrum of aggregated and bundled nanotubes in SDS micelles. (Reproduced from *[101]*)

Generally, ionic surfactants including cationic and anionic surfactants are preferred to achieve individual SWNTs in water *[72]*, such as SDS, sodium dodecylbenzenesulfonate (SDBS), sodium dodecylsulfonate (SDSA), sodium *n-*lauroylsarcosinate (Sarkosyl), sodium alkyl allyl sulfosuccinate (TREM), dodecyltrimethylammonium bromide (DTAB), cetyltrimethylammonium bromide (CTAB), etc.

Alternatively, nonionic surfactants, such as water soluble polymers, can also be used. Owing to the flexibility of the long polymer chains and their affinity to the CNT side-walls, a wrapping mechanism has been proposed for polymer-based CNT dispersion (Figure 2.4) *[103]*. Such nonionic polymers include polyvinyl pyrrolidone (PVP), polyethylene oxide (PEO), polypropylene oxide (PPO), and some water soluble bi- and tri-block copolymers, i.e., Pluronic series *[72]*. Moreover, polycations and polyanions such as polystyrene sulfonate (PSS) are also frequently utilized to achieve individually dispersed SWNTs to fabricate CNT films *[103, 104]*.
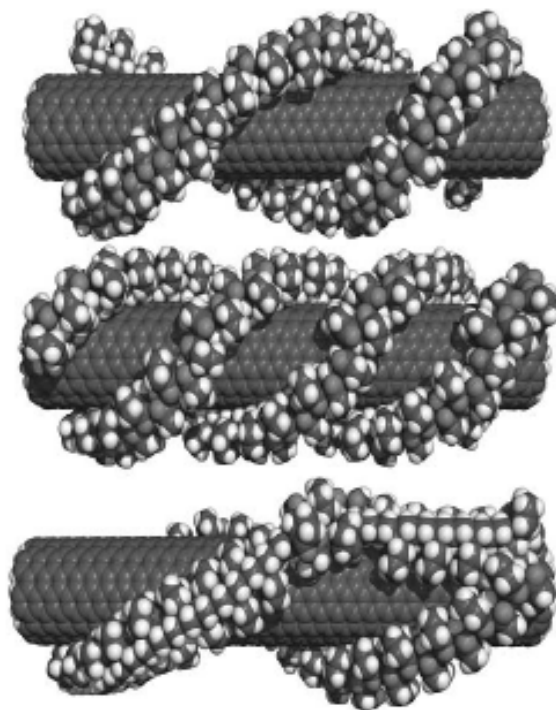
Figure 2.4. Some possible wrapping arrangements of PVP on a SWNT. (Reproduced from *[103]*)

The yield of the above method using a variety of surfactants and polymers to achieve individual SWNTs was also studied by the Smalley's group. The results show that only a small amount of SWNTs have been exfoliated (less than 10 %, generally 3 – 5 %) *[72]*. Despite of its low conversion, this general approach has been the major way to produce high-quality individual SWNTs for various fundamental studies and applications.

The above method has also been extended to bio-based surfactants. For example, Zheng et al utilized DNA as surfactant to stabilize SWNTs with help of ultrasonication and subsequent ultracentrifugation *[105]*. Individually dispersed SWNTs in water has been obtained as illustrated by the UV-vis-NIR (Figure 2.5). The dispersion mechanism is proposed to be DNA wrapping of CNTs similar to polymer wrapping.
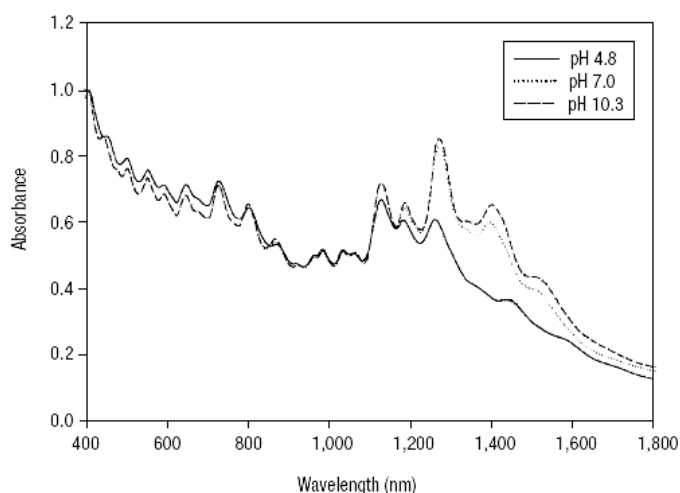
Figure 2.5. UV-vis-NIR of DNA-SWNTs at different pH values. (Reproduced from *[105]*)

Many other specific surfactants and polymers have also been used or synthesized to obtain individual SWNTs and MWNTs through a similar approach. Since the dispersion mechanism is the same and no significant improvement has been found, they will not be reviewed here.

To achieve a high solubility of SWNTs in water, chemical functionalization of nanotube surface has been developed. Different from the physical absorption of surfactants and polymers, the functional groups containing hydrophilic ends are covalently bonded with surface C atoms to increase the CNT solubility in water. For example, Liang et al functionalized SWNTs with phenyl groups, followed by a sulfonation process (Figure 2.6) *[106]*. The sulfonated SWNTs are highly exfoliated (Figure 2.7) and can maintain a stable dispersion over a few months. A major drawback of chemical functionalization of CNTs is the significant damage of nanotube side-walls such that the physical properties, especially electrical and optical properties, are compromised (Figure 2.8).
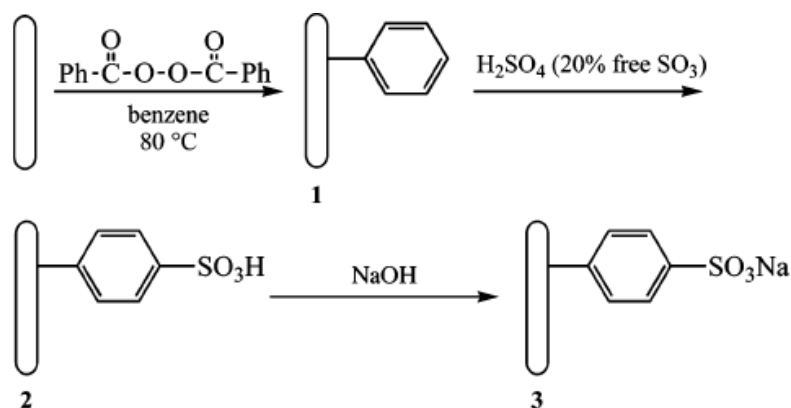
Figure 2.6. Sulfonation of SWNTs. (Reproduced from *[106]*)
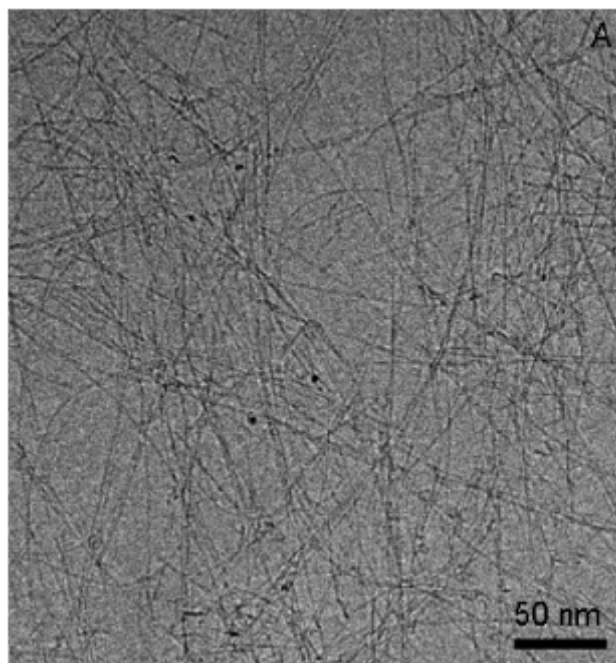
Figure 2.7. Cryo-TEM of sulfonated SWNTs in water. (Reproduced from *[106]*)
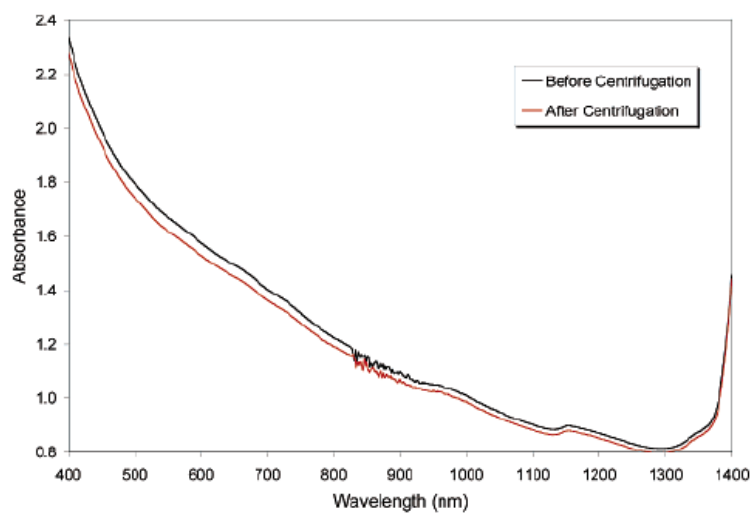
Figure 2.8. UV-vis-NIR of chemically functionalized SWNTs. (Reproduced from *[106]*)

2. 2. 2. Stabilization of CNTs in Organic Solvents

The sonication-assisted surfactant dispersion of CNTs has also been utilized to stabilize CNTs in various organic solvents, such as alcohols, amides, acetone, tetrahydrofuran (THF), DMSO, etc *[107-109]*. Various mono-, bi-, and tri-amines have been used as surfactants to achieve the CNT dispersion. However, similar to the aqueous dispersion, the conversion into individual nanotubes is low and the separation of individual tubes from small SWNT bundles is still challenging.

An effective method to achieve CNT dispersion in organic solvents is through chemical modification *[110-113]*. By covalently bonding functional groups on the CNT side-walls, high-concentration, individually suspended CNTs in various organic solvents have been achieved. For example, Michelson et al prepared "fluorotubes" by introducing fluorine onto the SWNT side-walls *[114]*. The resulting fluorinated SWNTs were found to highly soluble in short-chain alcohols, such as methanol, ethanol, and propanol. Based on the fluoro nanotubes, Saini et al further attached alkyl groups onto the tube side-walls *[115]*. These chemically modified SWNTs are soluble in THF and chloroform.

2. 2. 3. Dispersion of CNTs in Polymers

It has been found that better dispersion of CNTs in polymers leads to better properties *[116]*. Pristine CNTs are not soluble in polymers; therefore the dispersion of CNTs in polymers has been overwhelmingly dependent on the use of surfactants or

chemical modification. Three major fabrication methods have been utilized: (**i**) melt mixing, (**ii**) solution mixing, and (**iii**) in-situ polymerization.

Because of the high compatibility with current industrial processing of polymers, melt mixing appears to be an attractive method to prepare polymer/CNT nanocomposites. However, compared to other mixing methods, melt mixing shows much less effectiveness in dispersing CNTs in polymeric matrices. Moreover, owing to the high viscosity of polymer melts at high CNT concentrations, melt mixing is only limited for preparation of low-concentration nanocomposites. Both SWNTs and MWNTs have been incorporated into various polymers through melt mixing, such as nylon-6/MWNTs *[117]*, polypropylene/SWNTs *[118]*, polyimide/SWNTs *[119]*, etc.

Solution mixing is the most common method to achieve a good dispersion of CNTs in polymers. This method generally involves three steps to prepare the composite: (**a**) dispersion of CNTs in a solvent, (**b**) dissolution of a polymer in the CNT solution, and (**c**) evaporation of solvent or precipitation of the polymer with CNTs. For example, Zhang et al used PVP to disperse SWNTs in water through polymer wrapping, followed by dissolution of polyvinyl alcohol in the aqueous solution *[120]*. After solution casting and solvent evaporation, PVA/SWNTs/PVP films were prepared, which show greatly improved mechanical properties. Mitchell and Krishnamoorti dispersed SWNTs in poly(ε-caprolactone) with the aid of a zwitterionic surfactant *[121]*. The polymer nanocomposites show excellent mechanical and electrical properties. Zhu et al first functionalized SWNTs with alkylcarboxyl groups and diamines, and then solution mixing of such functionalized SWNTs with epoxy resin in organic solvents was

performed *[122]*. After solvent evaporation and epoxy curing, the epoxy/SWNT nanocomposites show highly improved mechanical property. Dalmas et al used ionic surfactant SDBS to disperse MWNTs in water, followed by mixing with poly(styrene-co-butyl acrylate) latex *[123]*. After drying, the polymer/MWNT nanocomposites exhibit enhanced mechanical and electrical properties.

The in-situ polymerization method starts with dispersing CNTs in monomers, followed by polymerization to prepare polymer/CNT nanocomposites. Clayton et al prepared polymethyl methacrylate (PMMA)/SWNTs nanocomposites through in-situ polymerization of the monomers with non-functionalized SWNTs *[124]*. Electron microscopy images show that bundled SWNTs are well-dispersed and the nanocomposites show a good dielectric property. Moniruzzaman et al synthesized nylon with the existence of SWNTs functionalized with Alkyl Acid Chloride *[125]*. Good dispersion of SWNTs in nylon has been observed and excellent mechanical property has been achieved. Preparation of epoxy/CNT nanocomposites can also be considered as an in-situ polymerization method. CNTs are first dispersed in epoxy resin (monomer), followed by adding hardeners and curing of epoxy. For example, Zhu et al incorporated the fluorinated SWNTs with epoxy resin. After curing, SWNTs were found to well-dispersed in the epoxy matrix. A great improvement in mechanical property has also been observed at a low nanotube loading *[126]*.

2.3. Self-assembly of Inorganic Nanoplatelets

Theoretical development has shown that colloidal anisotropic particles, such as rods or platelets, have the ability to self-assemble into liquid crystalline structures. Different from molecular or polymer liquid crystals where the phase transition is associated with temperature, the phase transition of colloidal liquid crystals mainly depends on the concentration *[127]*. Colloidal platelets can form three types of liquid crystalline structures: nematic (N), columnar (C), and smectic (S) (Figure 2. 9), and they exhibit birefringent characteristics under polarized lights (Figure 2.10) *[128]*.
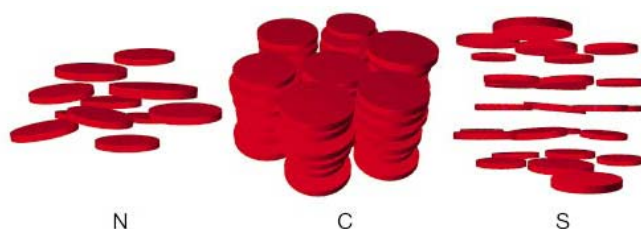
Figure 2.9. Liquid crystalline structures of colloidal platelets. (Reproduced from *[128]*)
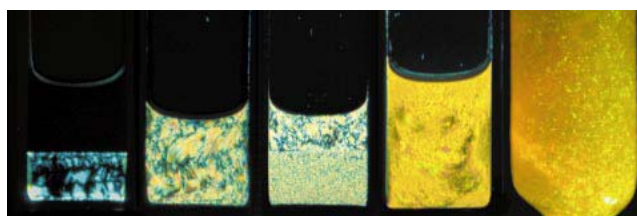
Figure 2.10. Liquid crystalline birefringence from self-assembled colloidal platelets. (Reproduced from *[128]*)

The first observation of the N phase from natural clay was reported in late 1930s *[129]*. However, the observed N phase was not stable and found to become amorphous gel within a few days. Moreover, this self-assembling phenomenon is not reproducible due to the complex nature of natural clay.

Although experimental observations from colloidal clays are limited, simulations have predicted the development of rich phase behaviors of colloidal platelets. For example, Veerman and Frenkel simulated the liquid crystalline phase transition of a model platelet – cut sphere with a small diameter-to-thickness ratio (aspect ratio) *[130]*. They showed that these model platelets exhibit phase transition from isotropic (I) to N to C upon increasing the sample volume fraction. Simulations on thin platelets (infinite aspect ratio) show similar phase transitions except that the volume fractions where each transition occurs are different *[131, 132]*. It has also been found that many characteristics of the platelets can affect their self-assembling behaviors, such as aspect ratio, polydispersity in diameter, interactions between platelets, etc *[133-135]*.

Experimental efforts have mostly been relying on the use of inorganic synthetic platelets in the past decade. Equilibrium phase transition into various liquid crystalline structures has been found using synthetic platelets, and new liquid crystalline phases have been discovered. For example, Brown et al studied the phase transition of colloidal plate-like nickel(II) hydroxide ($Ni(OH)_2$) *[136]*. N and C liquid crystalline structures have been found in this system. van der Kooij and Lekkerkerer built a platelet system with minimal interactions using colloidal Gibbites ($Al(OH)_3$) *[79]*. Their experimental results from this model system agree very well with the simulations. They further

studied the effect of polydispersity in diameter on the self-assembly of colloidal platelets and found that the C phase is significantly suppressed by a high polydispersity in diameter *[128]*. Zhang et al studied the self-assembly of colloidal layered double hydroxides (LDH). I – N transition has also been found *[137]*. Gabriel et al synthesized a type of solid acids with a layered structure. By swelling the layered sheets, they discovered a new type of liquid crystalline phase – lamella phase, which can extend their layer distance up to a few hundred nanometers *[138]*. This lamella phase was also observed in the LDH system *[139]*.

2.4. Concluding Remarks

This chapter has reviewed the current progresses on (**i**) the stabilization of 0-D QDs in various solvents and polymers, (**ii**) the debundle and dispersion of 1-D CNTs in water, organic solutions and polymer matrices, and (**iii**) the self-assembly of 2-D nanoplatelets into ordered structures. Through the use of surfactants and surface modifications, stable dispersion of inorganic nanostructures in different media has been achieved. Many material properties have been measured and many potential applications have been addressed. However, fundamental and practical issues regarding the colloidal dispersion of nanostructures are yet to be resolved, such as dispersion of inorganic nanoparticles in organic media without using organic surfactants or ligands, large-scale full exfoliation of SWNTs without damaging tube side-walls, and achieving individually dispersed CNTs in polymeric matrices. Meanwhile, self-assembly of colloidal platelets

is a less-studied field. Model system investigation using synthetic platelets needs to be established.

CHAPTER III

EXFOLIATION AND SELF-ASSEMBLY OF TWO-DIMENSIONAL NANOPLATELETS

3. 1.　Introduction

Two-dimensional plate-like nanomaterials, including natural and synthetic clays, Gibbsites, layered double hydroxides, layered phosphates, etc, have been widely used as ionic exchangers, colloidal additives, catalysts and supporting templates. Plate-like materials generally have a layered structure where each layer stacks with each other through van der Waals attractions or hydrogen bonding. The exfoliation of these layered nanomaterials into individually dispersed nanoplatelets in various media especially in polymers has attracted enormous attention in the past decade. For example, due to their 2-D nature and extremely large surface area, it is believed that polymer nanocomposites containing fully exfoliated nanoplatelets would show exceptional mechanical, thermal, and barrier properties.

Colloidal nanoplatelets also show ability to self-assemble into ordered structures under certain conditions. The disorder – order transition has been an active research area since the observation of the liquid-crystalline nematic phase in clay suspensions by I. Langmuir in 1938*[129]*. Theoretical development on the phase transition of anisotropic colloids has shown that over a critical concentration, rod- or plate-like colloids self-assemble into nematic structure – a liquid crystalline configuration that possesses long-range orientational order due to the entropic volumetric effect.　In the past decade,

synthetic platelets have been used extensively to investigate the liquid crystal phase transitions *[128, 130, 136]*, such as the isotropic (I) to nematic (N) and nematic to columnar (C) transitions. A detailed literature review can be found in the last chapter. It should be noted here that colloidal layered nanoplatelets possess high polydispersity both in diameters and in thicknesses, which dramatically modify their liquid crystal phase transitions. Although controlling the polydispersity of the platelet diameter has not yet been achieved, by exfoliation, a uniform thickness can be obtained. Here, plate-like α-zirconium phosphate (ZrP) with various diameters was synthesized and exfoliated in water. The exfoliated monolayer platelets have an identical thickness. An unusual arrangement of platelets into smectic (S) structure has been found. Phase transitions such as isotropic − nematic (I − N) and nematic − smectic (N − S) are studied. The experimental results also demonstrate that the smectic crystals self-assemble at low volume fractions when large-aspect-ratio disks are used. Possible criteria on the formation of the smectic phase of colloidal platelets are also proposed.

3. 2   Experimental

3. 2. 1. Synthesis and Exfoliation of ZrP Platelets Containing Various Aspect Ratios

Small-diameter ZrP platelets were synthesized through a refluxing method. Briefly, 15.0 g of $ZrOCl_2 \cdot 8H_2O$ (Fluka, 99%) was refluxed in 150.0 mL of 3.0 M H_3PO_4 in a Pyrex glass flask with stirring at 100 °C for 24 hours. This sample is designated as ZrP-R-3M.

Large-diameter ZrP platelets were synthesized through a hydrothermal method. Four grams of $ZrOCl_2 \cdot 8H_2O$ were mixed with 40.0 mL of 3, 6, 9, and 12.0 M H_3PO_4 in an autoclave, followed by reaction at 200 °C for 24 hours. These samples are designated as ZrP-HT-3M, ZrP-HT-6M, ZrP-HT-9M, and ZrP-HT-12M, respectively.

After synthesis, the products were washed three times through centrifugation and resuspension, dried at 85 °C in an oven for 24 hrs, and then gently ground with a mortar and pestle into a fine powder. The ZrP powders were exfoliated with tetra-n-butylammonium hydroxide (TBA^+OH^-, Aldrich, 1 mol/L in methanol) at a molar ratio of ZrP:TBA = 1:1 in water containing various volume fractions. The exfoliated samples are designated as Ex_ZrP-HT-3M, Ex_ZrP-HT-6M, Ex_ZrP-HT-9M, and Ex_ZrP-HT-12M, respectively.

3. 2. 2. Characterization

Transmission electron microscopy (TEM) of pristine ZrP platelets was taken using a JEOL 2010 high-resolution transmission electron microscope operated at 200 kV. A drop of diluted suspension of ZrP platelets in water was placed on a copper grid coated with carbon support film and then dried at room temperature. Dynamic light scattering (DLS) of TBA-exfoliated ZrP platelets was performed on a ZetaPals analyzer (Brookhaven Instrument Corp., NY) with diluted aqueous solutions. Optical images were obtained using an Olympus microscope BX60.

The aqueous ZrP suspensions were directly characterized by X-ray diffraction (XRD) in a wet state. A drop of the aqueous suspension was placed onto a glass holder

and covered by a Mylar film (Complex industries, Inc., Palm city, FL) to minimize evaporation during XRD experiments. The XRD patterns were recorded by a Bruker D8 Diffractometer with Bragg-Brentano $\theta - 2\theta$ geometry (40 kV and 40 mA), using a graphic monochromator with Cu-K$_\alpha$ incident radiation (λ=1.5418 Å).

3. 3.   Results and Discussion

3. 3. 1. Characteristics of Pristine and Exfoliated ZrP Nanoplatelets

Figure 3.1 shows the TEM images of pristine ZrP nanoplatelets with various diameters synthesized at different conditions. Refluxing method at low acid concentration (sample ZrP-R-3M) produces the smallest ZrP nanoplatelets with an average diameter of around 100 nm. ZrP nanoplatelets synthesized through hydrothermal method have larger diameters, and the higher the acid concentration, the larger the diameters of the platelets are produced. When the acid concentrations are 3M, 6M, 9M, and 12M, the diameters are around 300nm, 500nm, 1μm, and 2 μm, respectively.

The pristine ZrP nanoplatelets contain different amount of layers in each crystals depending on the synthesis conditions, but have the same layer distance (d-spacing) as shown in the XRD patterns (Figure 3.2). Therefore, the thickness (t) of each crystal sample varies. Estimation on the thickness of each sample based on Debye-Scherrer formula $t = 0.89\lambda /(\beta \cos\theta)$ (θ, the diffraction angle; t stands for the average dimension of a crystal at certain direction corresponding to θ; λ, the X-ray wavelength, 1.5418 Å; and β, full width at half maximum, FWHM, of the diffraction peak.) using (002) peaks

shows $t_{\text{ZrP-R-3M}} < t_{\text{ZrP-HT-3M}} < t_{\text{ZrP-HT-6M}} < t_{\text{ZrP-HT-9M}} < t_{\text{ZrP-HT-12M}}$, similarly to the diameter

trend from different samples.

A   B   C

D   E
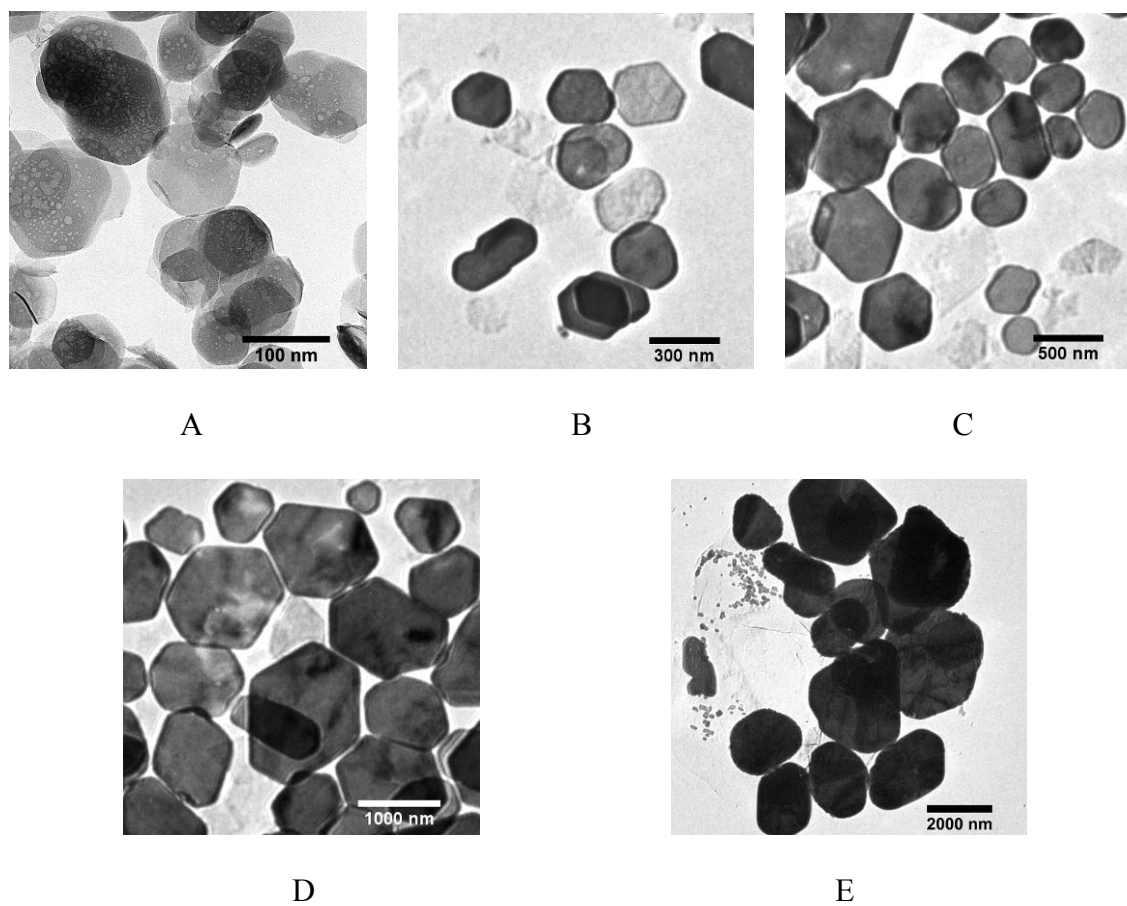
Figure 3.1. TEM images of pristine ZrP nanoplatelets. (A) ZrP-R-3M, (B) ZrP-HT-3M, (C) ZrP-HT-6M, (D) ZrP-HT-9M, and (E) ZrP-HT-12M.
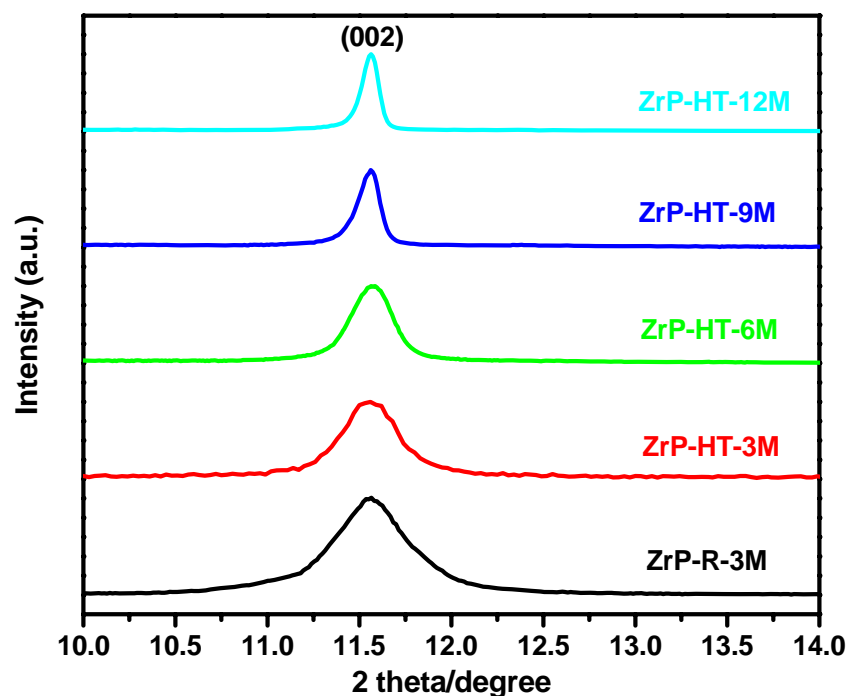
Figure 3.2. XRD patterns of pristine ZrP nanoplatelets

To obtain exfoliated ZrP nanoplatelets with uniform thickness, TBA$^+$OH$^-$ was used to achieve the full exfoliation of layered ZrP crystals into monolayers. As opposed to pristine ZrP, which is a weak acid, TBA$^+$OH$^-$ is a strong base and highly hydrophilic. It has been shown that when TBA$^+$OH$^-$ is reacting with pristine ZrP nanoplatelets in water, the acid-base reaction drives TBA$^+$ to intercalate into the ZrP layers, followed by exfoliation through hydrolation *[140, 141]*. Figure 3.3A-E show the TEM of a typical monolayer platelet of each sample after exfoliation. According to their chemical structures, the TBA-ZrP monolayer platelet, which contains two TBA monolayers, has an identical thickness of 2.68 nm (Figure 3.3F).

A

B

C

D

E

F
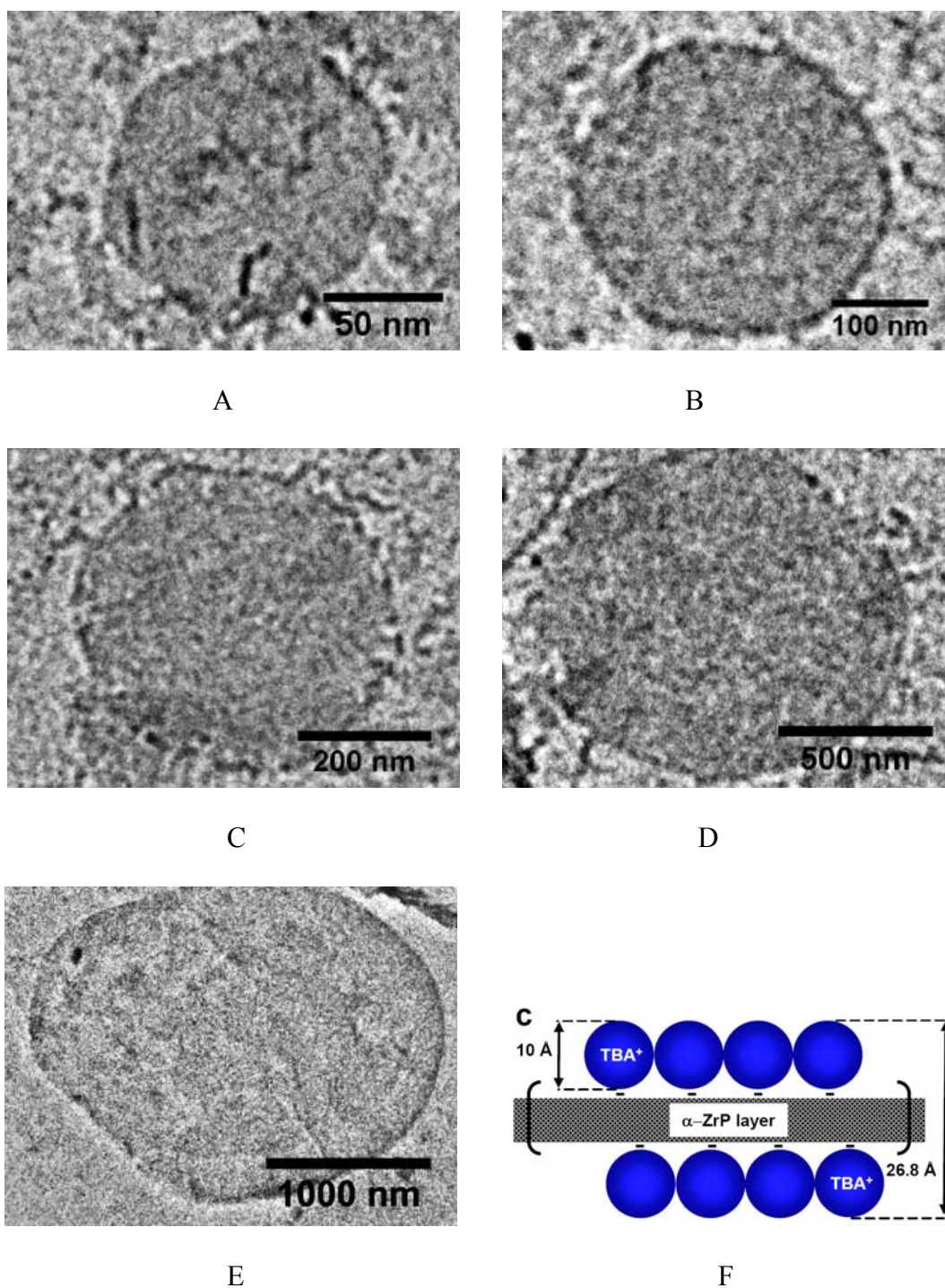
Figure 3.3 (A)-(E) TEM images of exfoliated ZrP monolayer platelets. (F) Thickness profile of the ZrP monolayer platelet. The length is not drawn to scale.

To obtain a more accurate estimation of the platelet diameter of each sample and their diameter polydispersity, DLS was performed on the exfoliated ZrP monolayer platelets (Figure 3.4). The average effective sphere diameters ($D_{eff.}$) of samples Ex_ZrP-HT-3M, Ex_ZrP-HT-6M, Ex_ZrP-HT-9M, and Ex_ZrP-HT-12M are 72.9, 210.5, 359.0, 814.5, and 1461.8 nm, respectively. The polydispersity (σ) of each sample from Gaussian simulation is 29%, 33%, 26%, 30%, and 32%, respectively, which are consistently about 30% throughout. The conversion of D_{eff} to platelet diameter can be obtained through the following equation:

$$2t = \frac{k_B T}{3\pi\eta D_{eff}} \frac{1}{\sqrt{(D/t)^2 - 1}} arctg\sqrt{(D/t)^2 - 1} \tag{1}$$

Where t is the thickness of the platelet, k_B is Boltzmann's constant, T is absolute temperature, η is the viscosity of water, D_{eff} is the effective sphere diameter obtained from DLS. The calculations based on this equation yield the platelet diameters of 113, 328, 562, 1277, and 2295 nm, respectively, for samples Ex_ZrP-R-3M, Ex_ZrP-HT-3M, Ex_ZrP-HT-6M, Ex_ZrP-HT-9M, and Ex_ZrP-HT-12M, which are close to the TEM estimations. Since the exfoliated ZrP monolayer platelets have an identical thickness, each value on the polydispersity of D_{eff} from DLS can also represent the diameter polydispersity of the exfoliated and pristine ZrP platelets, σ_D. The characteristics of the exfoliated ZrP monolayer platelets are summarized in Table 3.1.
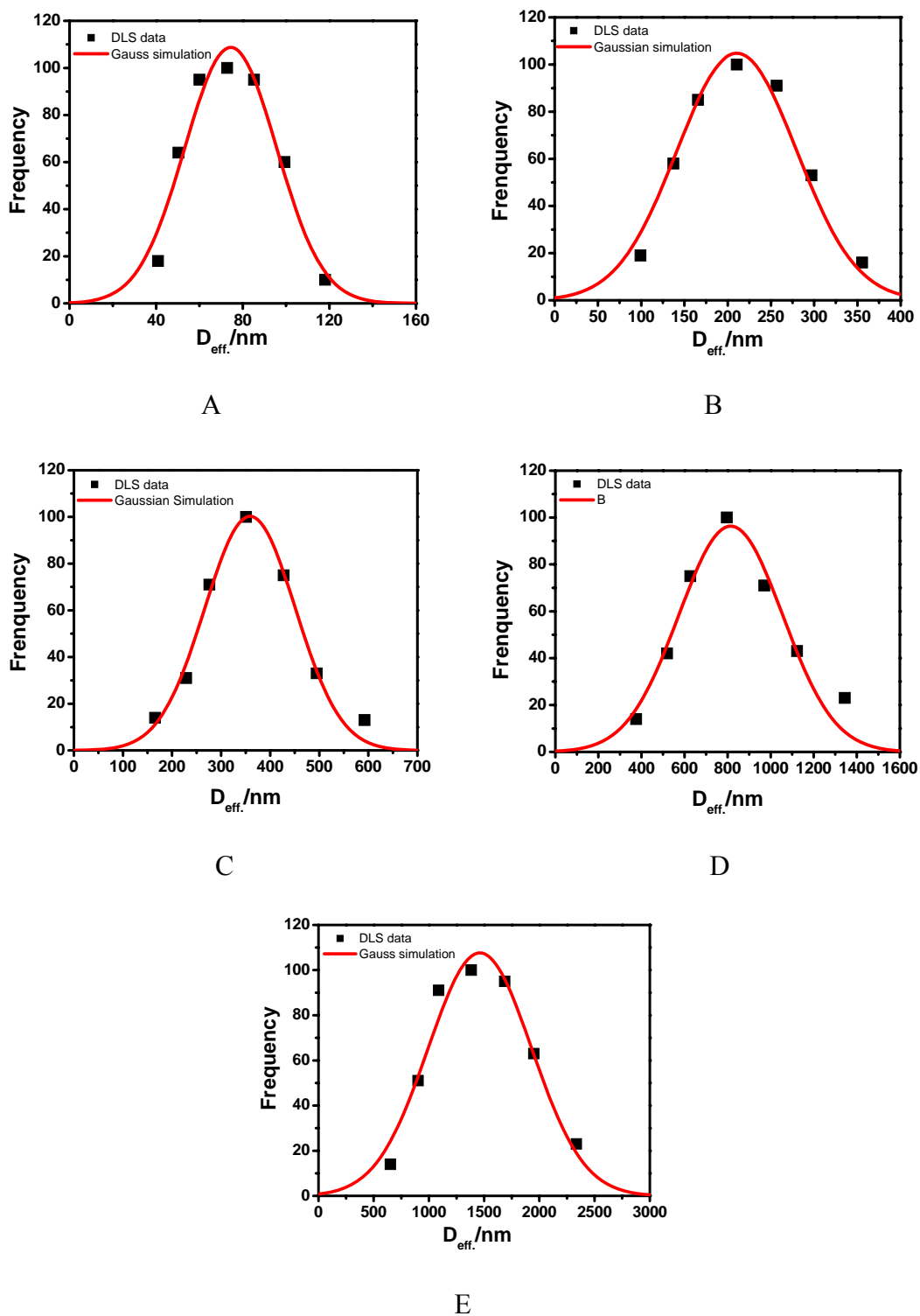
Figure 3.4. DLS of exfoliated ZrP nanoplatelets. (A) Ex_ZrP-R-3M, (B) Ex_ZrP-HT-3M, (C) Ex_ZrP-HT-6M, (D) Ex_ZrP-HT-9M, and (E) Ex_ZrP-HT-12M.

Table 3.1. Characteristics of exfoliated ZrP monolayer platelets

Sample	D(nm)	σ_D(%)	t(nm)	$\rho = D/t$
Ex_ZrP_R_3M	113	29	2.68	42
Ex_ZrP_HT_3M	329	33	2.68	123
Ex_ZrP_HT_6M	562	26	2.68	210
Ex_ZrP_HT_9M	1278	30	2.68	477
Ex_ZrP_HT_12M	2295	32	2.68	856

3. 3. 2. Self-assembly of Exfoliated ZrP Nanoplatelets with High Aspect Ratio

Figure 3.5 shows the optical images of aqueous suspensions of sample Ex_ZrP_HT_12M (ρ = 856) with various concentrations. At $\phi <$ 0.001, ZrP nanoplatelets form a random stable dispersion – isotropic (I) phase – in water. Upon increasing sample volume fraction, a clear phase transition can bee seen. Birefringent features under crossed-polarized imaging reveal that sample Ex_ZrP_HT_12M self-assemble into liquid crystalline nematic (N) structures at volume fraction > 0.001. At $\phi =$ 0.001 – 0.03, I and N phases coexist with each other. A full nematic phase is obtained at at $\phi =$ 0.03 – 0.06. The macroscopic phase separation is completed within 24 hours. The disorder – order transition at such a low concentration with such a wide I – N coexistence region (Figure 3.6) can be interpreted by the large aspect ratio *[127]* and the high polydispersity *[132]* of the current system.
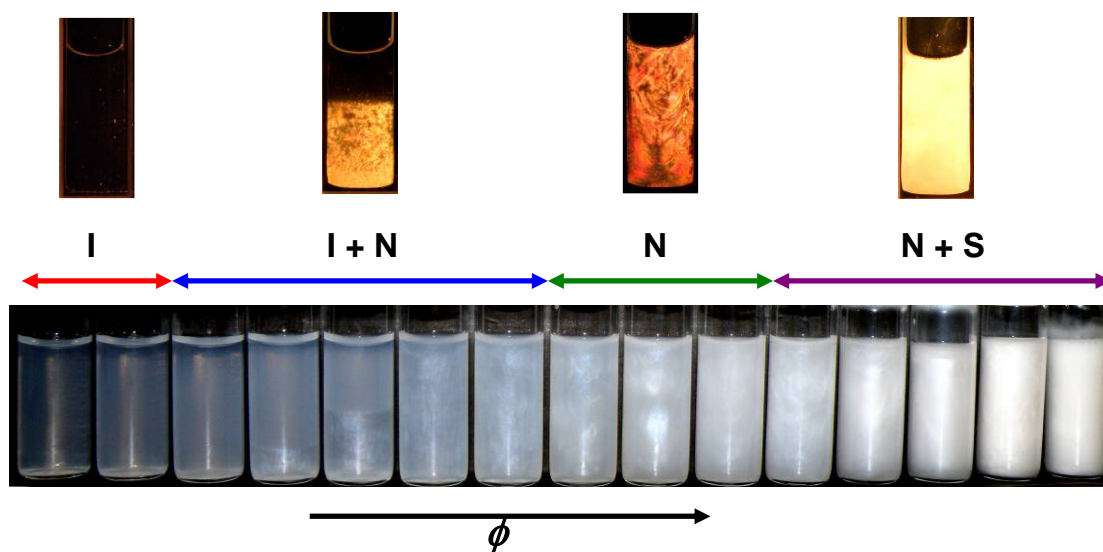
Figure 3.5. Aqueous suspensions of sample Ex_ZrP_HT_12M with various concentrations. The images on the bottom are taken under white lights with ϕ = 0.004, 0.007, 0.009, 0.013, 0.017, 0.021, 0.031, 0.041, 0.048, 0.054, 0.059, 0.074, 0.10, 0.16, and 0.20 from left to right. The top images are samples of representative phases under crossed-polarizers.
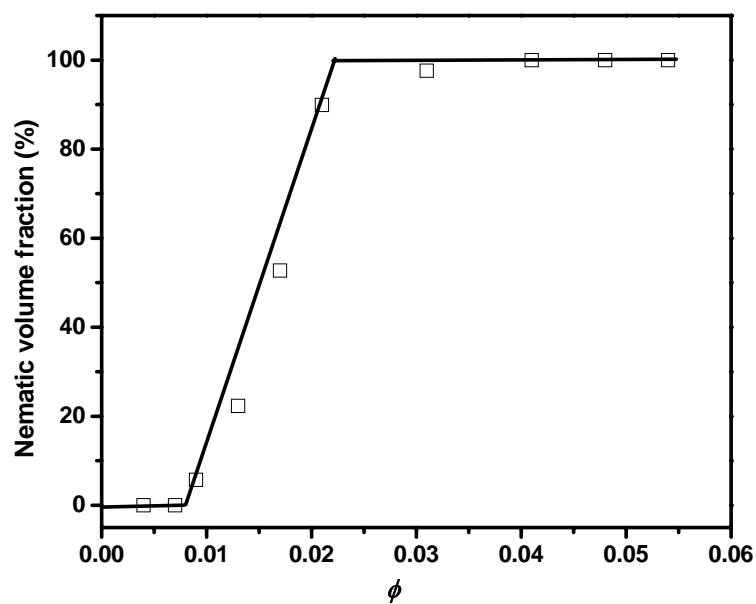
Figure 3.6. I – N transition of sample Ex_ZrP_HT_12M.

The smectic (S) phase of liquid crystals has a layered structure where each layer is a two-dimensional liquid *[127]*. This one – dimensionally ordered phase has a degree of ordering between nematic (only long-range orientational order, no positional order) and columnar (two – dimensional positional order). The S arrangements of anisotropic colloids such as rod- and disk-like particles are illustrated in Figure 3.7. The S phase is commonly observed from the rod-like colloids and molecules that have a low polydispersity in length and has been considered to be a thermodynamically stable phase. However, the S phase from plate-like colloids and molecules has rarely been observed experimentally. However, it is suggested that colloidal platelets with uniform thickness may lead to a smectic-like arrangement *[128]*.
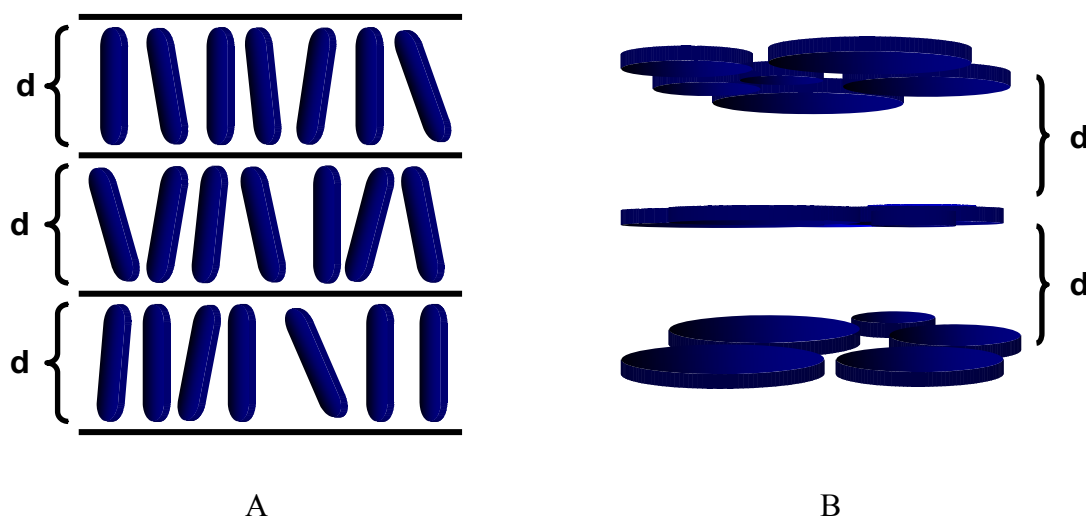
Figure 3.7. The smectic phase of liquid crystals. (A) Rods (only smectic A is shown), and (B) Disks. The smectic phase exhibits a one – dimensional layered structure with each layer is in a liquid state.

In the current experiments, upon further increasing the sample volume fraction, a layered arrangement of exfoliated ZrP nanoplatelets is found, as characterized by XRD (Figure 3.8). Multiple scattering peaks are observed for samples above $\phi = 0.06$, indicating their strong layered ordering. This is a characteristic of smectic liquid crystals. Since nematic liquid crystals do not possess positional order, only a long-range orientational order, no XRD peaks can be observed in the N phase.

Optical microscopic and TEM images (Figure 3.9A and B) show that the crystalline domains, at an early stage of their formation, are about $10 - 40$ μm in size. High-resolution TEM image (Figure 3.9C) also suggests that these crystalline domains have a layered structure, which agrees with the XRD results. By considering the fact that the individual platelets have a diameter of around 2 μm, each layer in these crystalline domains should contain multiple individual platelets. Therefore, microscopy and XRD evidence indicate that the crystalline domains observed are smectic liquid crystals as shown in Figure 3.7B. Moreover, these small smectic domains can further coalesce into a ribbon-like smectic mesophase (Figure 3.9D – F).
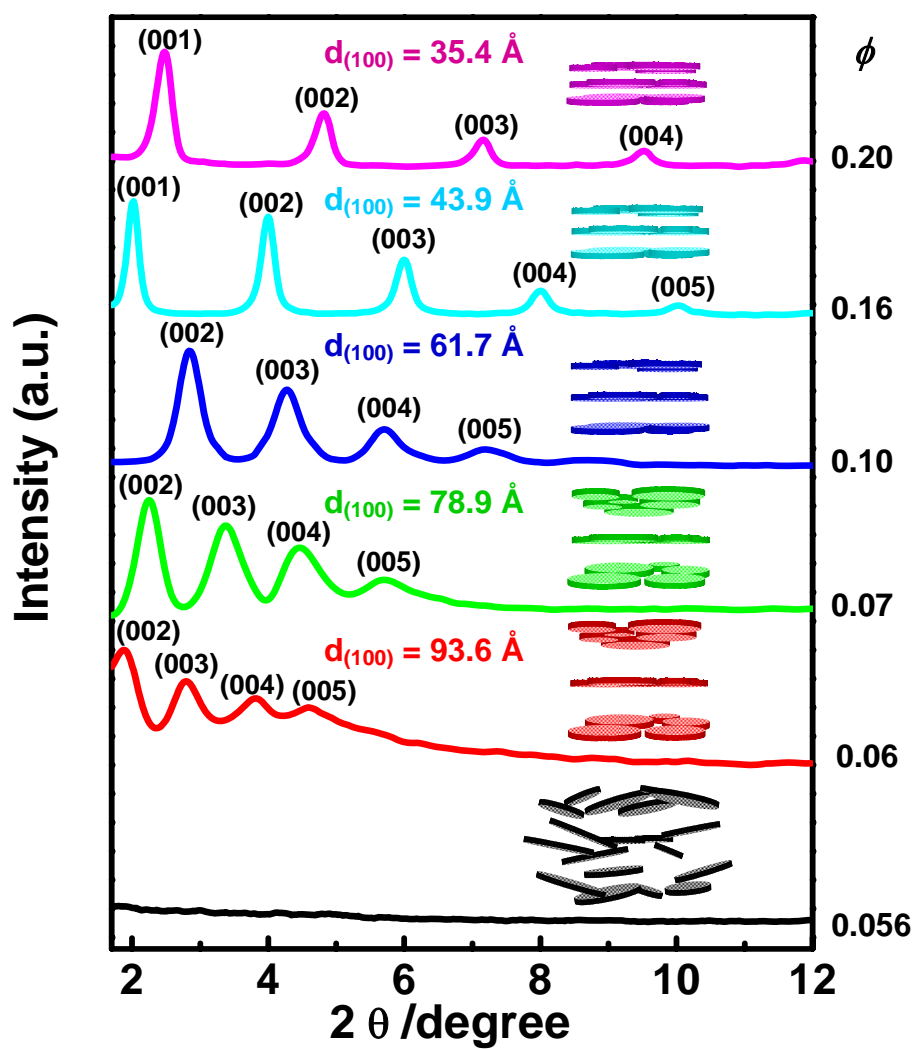
Figure 3.8. XRD patterns of sample Ex_ZrP_HT_12M at high volume fractions.
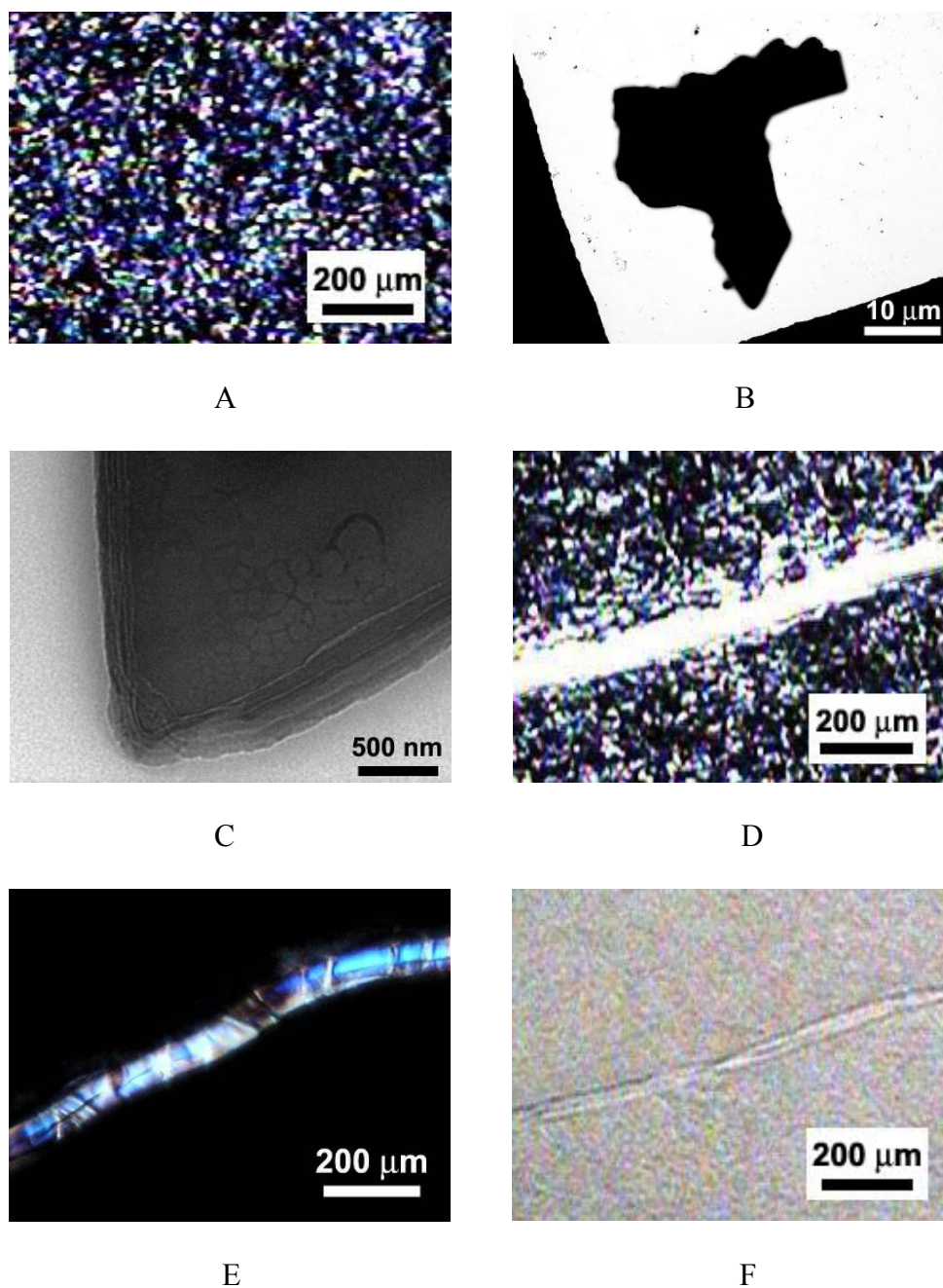
Figure 3.9. Smectic liquid crystals of sample Ex_ZrP_HT_12M at ϕ = 0.20. (A) Crossed-polarized image of the sample prepared after 1 day. (B) TEM image of a crystalline domain. (C) High-magnification TEM image of (B) showing the layered structure. (D) and (E) Crossed-polarized images of the sample prepared after 1 week. The image in (D) is taken under dimmed lights. (F) Optical image of sample (D) under white lights.

Interestingly, from the XRD patterns in Figure 3.8, the smectic interlayer spacing (d-spacing) decreases continuously as ϕ increases. Estimation of the volume fraction of the observed smectic phase based on the d-spacings shows that a much higher sample volume fraction is needed to form a pure smectic phase (Table 3.2). This indicates that the suspensions with $\phi \geq 0.06$ contain both smectic and nematic phases, confirming the optical observations that the smectic domains are dispersed in the nematic phase (Figure 3.9A and D). Aqueous suspensions having higher volume fractions of exfoliated ZrP platelets ($\phi > 0.20$) are not experimentally accessible due to their extremely high viscosity. It should be noted that swelling of rigid layered sheets can extend the d-spacing up to a few hundred nanometers *[138]*. However, the lamellar structure is fundamentally different from the smectic phase of colloidal platelets observed here because it does not possess the characteristic two – dimensional liquid layers.

Table 3.2. Characteristics of the smectic phase of sample Ex_ZrP_HT_12M.

ϕ	$d_{(100)}$	ϕ_s
0.054	—	—
0.059	93.6 Å	0.286
0.074	78.9 Å	0.340
0.102	61.7 Å	0.434
0.161	43.9 Å	0.610
0.199	35.4 Å	0.757

Note: ϕ is the volume fraction of the samples. ϕ_s is the calculated volume fraction of the smectic phase based on the corresponding d-spacing.

3. 3. 3. Self-assembly of Exfoliated ZrP Platelets Possessing Various Aspect Ratios

Figure 3.10 and Table 3.3 show the I – N transition of the exfoliated ZrP nanoplatelets with various aspect ratios. As the aspect ratio decreases, the disorder – order transition occurs at higher volume fractions and the I – N coexistence region becomes wider. The volume fractions at the I – N transition, ϕ_{I-N}, of samples Ex_ZrP-R-3M ($\rho = 42$), Ex_ZrP-HT-3M ($\rho = 123$), Ex_ZrP-HT-6M ($\rho = 209$), Ex_ZrP-HT-9M ($\rho = 485$), and Ex_ZrP-HT-12M ($\rho = 858$) are 0.042, 0.026, 0.020, 0.013, and 0.010, respectively. The width of the I – N coexistence region of corresponding samples, $\Delta\phi_{I-N}$, are 0.013, 0.014, 0.017, 0.020, and 0.037, respectively.
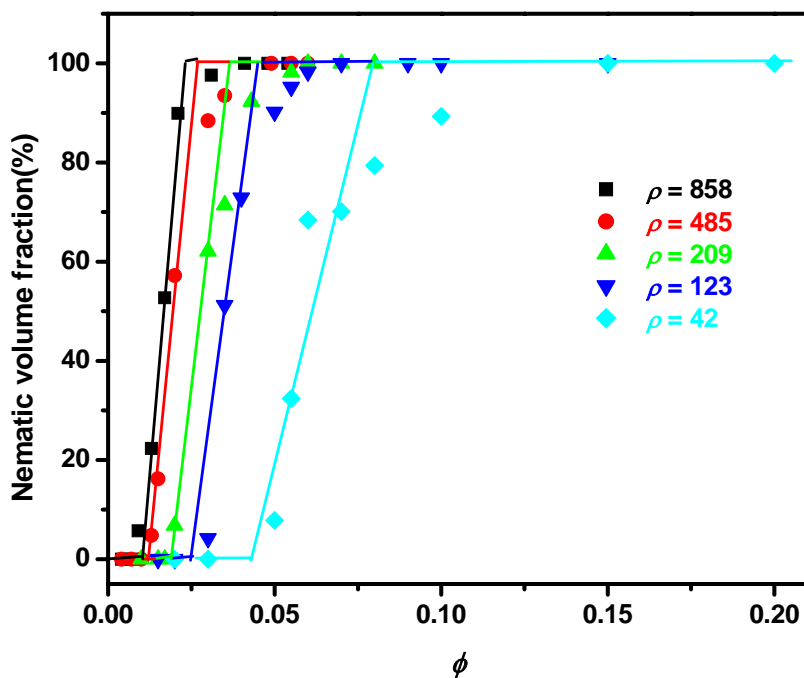
Figure 3.10. I – N transition of exfoliated ZrP nanoplatelets possessing various aspect ratios.

Table 3.3. I – N transition of exfoliated ZrP nanoplatelets possessing various aspect ratios.

ϕ (%)	0.4	1.0	1.5	2.0	3.0	4.0	5.0	6.0	7.4	10.2
Ex_ZrP-R-3M $\rho = 42$	–	–	–	I	I	I	I+N	I+N	I+N	I+N
Ex_ZrP-HT-3M $\rho = 123$	–	–	I	I	I+N	I+N	I+N	I+N	N	N
Ex_ZrP-HT-6M $\rho = 209$	–	I	I	I+N	I+N	I+N	I+N	N	N	S
Ex_ZrP-HT-9M $\rho = 485$	I	I	I+N	I+N	I+N	N	N	N	S	S
Ex_ZrP-HT-12M $\rho = 858$	I	I+N	I+N	I+N	I+N	N	N	S	S	S

The formation of the nematic phase of non-interacting, thin, hard disk-like colloids can be analyzed by a simple model *[127]*:

$$b^3 c_N = 0.9 \qquad\qquad (2)$$

$$b^3 c_I = 0.67 \qquad\qquad (3)$$

Where b is the radius of the disks and c_N and c_I are the numbers of the disks per volume for the coexisting nematic and isotropic phases, respectively. The volume fractions of the disks for the coexisting nematic and isotropic phases, ϕ_N and ϕ_I, can be deduced from Eq. (2) and (3):

$$\phi_N = \frac{9t}{\pi b} \tag{3}$$

$$\phi_I = \frac{6.6t}{\pi b} \tag{4}$$

where t is the thickness of the disks. In the current experiments, $t = 2.68$ nm for all the exfoliated ZrP nanoplatelet samples. It should be noted that the sample volume fraction at I – N transition, ϕ_{I-N}, approximately equals the volume fraction of the I phase at I – N coexistence region, ϕ_I, because the I – N transition is a first order transition.

Table 3.4 lists ϕ_{I-N} and $\Delta\phi_{I-N}$ (ϕ_N - ϕ_I) from the experimental observation using exfoliated ZrP nanoplatelets and hard disk model. The ϕ_{I-N} can be affected by many factors, such as diameter, diameter polydispersity, aspect ratio, particle interaction, etc. Simulations and experimental observations using colloidal Gibbsites nanoplatelets have shown that polydispersity in diameter has a profound effect on the phase transition of colloidal platelets and that platelets with a higher polydispersity in diameter show a wider I – N coexistence region *[128, 131, 132]*. The exfoliated ZrP nanoplatelets used in this study have a diameter polydispersity of around 30% (Table 3.1), which explains the wide $\Delta\phi_{I-N}$ observed in the current study.

Table 3.5 and Figure 3.11 show the N – S transition and the smectic d-spacing of the exfoliated ZrP nanoplatelets having different aspect ratios. Similar to the I – N transition, ϕ_{N-S} shifts to a higher volume fraction when the aspect ratio of exfoliated ZrP nanoplatelets is decreased. No smectic phase is observed, even at $\phi = 0.3$, for the exfoliated ZrP nanoplatelets with $\rho = 42$, as indicated by the absence of the XRD peaks.

However, the sample with the largest aspect ratio ($\rho = 858$) shows a smectic order at only $\phi = 0.06$. These experimental observations clearly suggest that a large aspect ratio is responsible for the formation of the smectic phase of colloidal platelets at a low volume fraction. In fact, a smectic-like ordering in Gibbsites platelets with an aspect ratio of 10 – 30 and diameter polydispersity of 25% occurs at $\phi > 0.60$ after the formation of the columnar phase *[128]*. Interestingly, a columnar phase has not been observed in our system. This discrepancy might be explained by the facts that our platelets possess a larger polydispersity in diameter, which suppresses the formation of the columnar phase.

Table 3.4. Comparison of experimental results and hard disk model on the I – N transition.

Sample		Ex_ZrP-R-3M	Ex_ZrP-HT-3M	Ex_ZrP-HT-6M	Ex_ZrP-HT-9M	Ex_ZrP-HT-12M
Radius (b, nm)		57	165	280	650	1150
Experimental	ϕ_{I-N}	0.042	0.026	0.02	0.013	0.01
	$\Delta\phi_{I-N}$	0.037	0.02	0.017	0.014	0.013
Hard disk model	ϕ_{I-N}	0.099	0.034	0.02	0.0087	0.0049
	$\Delta\phi_{I-N}$	0.03	0.013	0.007	0.003	0.0018

Table 3.5. N – S transition of exfoliated ZrP nanoplatelets with various aspect ratios.

ϕ	0.059	0.074	0.092	0.102	0.161	0.199	0.3
Ex_ZrP-R-3M $\rho = 42$	I+N	I+N	I+N	I+N	N	N	N
Ex_ZrP-HT-3M $\rho = 123$	I+N	N	N	N	N	S (d=34.1Å)	S (d=27.8Å)
Ex_ZrP-HT-6M $\rho = 209$	N	N	S (d=69.0Å)	S (d=61.4Å)	S (d=42.8Å)	S (d=36.9Å)	–
Ex_ZrP-HT-9M $\rho = 485$	N	S (d=80.2Å)	–	S (d=64.4Å)	S (d=40.1Å)	S (d=38.0Å)	–
Ex_ZrP-HT-12M $\rho = 858$	S (d=93.6Å)	S (d=78.9Å)	–	S (d=61.7Å)	S (d=43.9Å)	S (d=35.4Å)	–
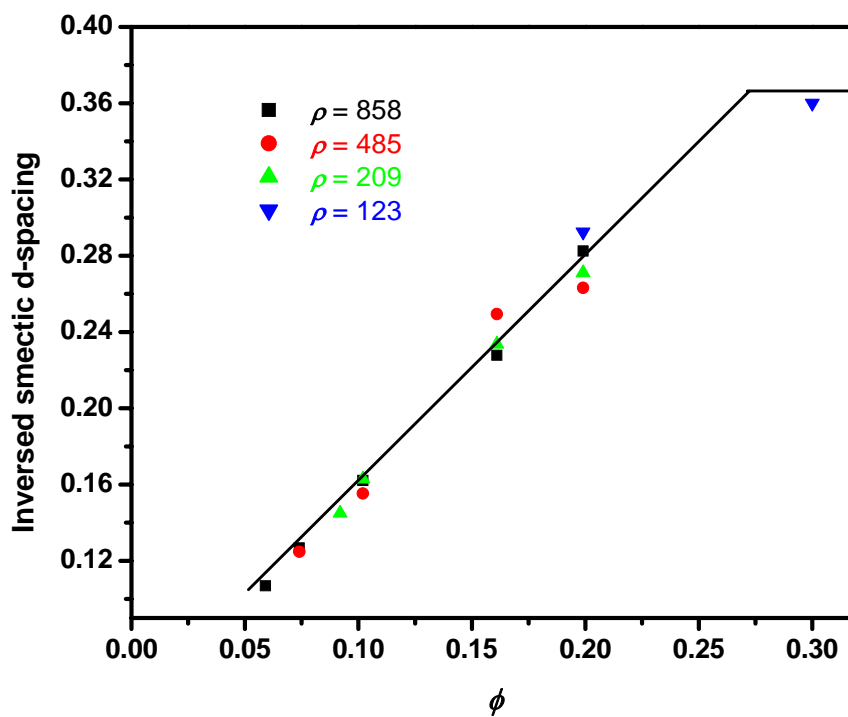
Figure 11. Smectic phase of exfoliated ZrP nanoplatelets with various aspect ratios.

3. 4.   Conclusions

In this chapter, self-assembly of colloidal nanoplatelets into liquid crystalline structures has been systematically studied. Monolayer ZrP nanoplatelets possessing a uniform thickness and various aspect ratios were obtained by fully exfoliating layered ZrP crystals with different diameters. Upon increasing volume fractions, aqueous suspensions of exfoliated ZrP nanoplatelets undergo a disorder – order transition to form a liquid crystalline nematic phase. At higher concentrations, a usual smectic arrangement of colloidal platelets was found using exfoliated ZrP nanoplatelets possessing high aspect ratios. The self-assembled liquid crystalline nematic and smectic structures were investigated by optical microscopy, TEM, and XRD. It has been found that the aspect ratio has a profound effect on the phase transition of colloidal nanoplatelets: the high-aspect-ratio nanoplatelets exhibit the liquid crystalline structures at low concentrations.

The experimental observations also demonstrate a set of possible conditions for disks/platelets to form a smectic liquid-crystalline phase: 1) uniform disk thickness to regulate the interlayer spacing, 2) large aspect ratio to achieve smectic phase formation at low volume fraction, and 3) high polydispersity in diameters to suppress the columnar phase formation. Simulations should be carried out in the future to verify the experimental observations and the possibility of the formation of the smectic phase in disk-like molecular systems.

CHAPTER IV

DISPERSION AND DEBUNDLING OF 1-DIMENSIONAL CARBON

NANOTUBES

4. 1. Introduction

Since their discovery in 1991, carbon nanotubes (CNTs) have drawn enormous attention due to their remarkable mechanical, electrical, and thermal properties. However, one of the remaining hindrances to the widespread use of CNTs is the absence of a robust, efficient, and innocuous method to completely debundle nanotube aggregates into an individually dispersed state. Once achieved, it is believed that the excellent properties shown from CNTs can be maximized and many existing technologies can benefit greatly. For example, CNTs are being used as highly efficient radio-frequency receivers *[62]*, to create nanotransistors and nanoscale electronics to move beyond silicon-based devices *[26, 53]*, integrated into light-harvesting cells as electrodes for fast carrier transfer *[142]*, and for controlling thermal and electrical conductivity and enhancing the strength and modulus of polymer composites. This obstacle to dispersion CNTs, especially for single-walled CNTs (SWNTs) arises because, immediately following their synthesis, the tubes readily assemble into a parallel configuration, commonly referred to as bundles or ropes, resulting in formidable tube-tube van der Waals (vdW) binding energies of ~20 $k_{B}T$ for every nanometer of tube overlap *[143]*. These bundled and aggregated states significantly undercut the superior physical and

mechanical properties of nanotubes, and impede the separation and sorting of nanotubes according to their length, diameter, and chirality.

Various strategies have been developed to disperse CNTs (See detailed literature review in **Chapter II**). It should be noted here that, among all the dispersion methods, non-covalent surface functionalization using surfactants, polymers, and bio-molecules with short sonication time followed by ultracentrifugation can achieve individually dispersed SWNTs in aqueous suspensions with preserved physical properties *[72, 101, 105]*. However, this method has an extremely low yield (~ 3-5 %) for producing individual SWNTs. Most of the tubes maintain bundled and aggregated.

Here, a simple and exceptionally effective method for physically pulling SWNT bundles apart by utilizing exfoliated nanoplatelets is introduced in this chapter. This approach yields a substantial fraction of individually dispersed SWNTs. Following dispersion, the SWNTs can be separated from the nanoplatelets by screening electrostatic interactions, after which they can be resuspended into single tubes through routine surfactant stabilization. This colloidal approach to dispersing SWNTs obviates the need to drastically modify nanotube surface chemistry to achieve full exfoliation, thereby preserving their intrinsic properties.

4. 2.   Experimental

4. 2. 1. Materials

α-zirconium phosphate (ZrP) nanoplatelets were synthesized and exfoliated according to the experimental methods described in **Chapter III**. In particular, ZrP

nanoplatelets with a mean diameter of ~100±45 nm were synthesized through a refluxing method and the nanoplatelets with an average diameter of ~550±130 nm were prepared through a hydrothermal method. Both pristine nanoplatelets were exfoliated using tetra-*n*-butylammonium hydroxide (TBA$^+$OH$^-$, Aldrich, 1 mol/L in methanol) in water at a molar ratio of ZrP:TBA = 1:0.8. Nanoplatelet size and polydispersity were measured with dynamic light scattering (See **Chapter III** for details).

Purified HiPco SWNTs were obtained from Carbon Nanotechnologies, Inc. (Houston, TX). The carbon content was nearly 100% HiPco SWNTs, which was purified to remove the large catalyst particles. The ash content of the HiPco SWNTs was less than 15%. For pre-treatment, about 50 mg of CNTs were first added to a mixture of 9 mL of concentrated sulfuric acid (EM Science) and 3 mL of concentrated nitric acid (EM Science). This mixture was sonicated (Branson 2510) for either 0.15, 3, 6, or 9 hr at a fixed temperature of 25 ºC, then 38 mL of deionized (DI) water was added to the flask to diminish the oxidative process and the mixture was sonicated for an additional three hours. After this process, the oxidized SWNTs were isolated using a polyvinylidene difluoride filter membrane (Millipore, 0.45 μm pore size) with the help of a vacuum pump. The CNTs were washed thoroughly with DI water during filtration to remove all traces of the acid. Nanotubes were then resuspended in DI water through another 3 hours of sonication (designated as pre-treated SWNTs).

4. 2. 2. Mixing of SWNTs and ZrP Nanoplatelets

Two aqueous solutions of pre-treated SWNTs and exfoliated ZrP nanoplatelets were directly mixed with various weight ratios and concentrations. Subsequently, the mixtures were sonicated in a sonication bath (Branzon) maintained at room temperature for 30 min. An aqueous solution containing only oxidized CNTs was also prepared for comparison purposes.

4. 2. 3. Characterization

Transmission electron microscopy (TEM) was performed using a JEOL 2010 high-resolution transmission electron microscope operated at 200 keV. The samples were first diluted to 2–5 ppm SWNT, and then a drop of each sample was placed onto a discharged carbon grid and dried at room temperature in a class-1000 clean room before imaging. X-ray photoelectron spectroscopy (XPS) data of the pre-treated SWNTs were obtained using a Kratos Axis Ultra. A non-monochromatic MgK_α photon source (1486 eV) was used for measurements. Data were fit using XPSPEAK 4.1 by applying a Shirley-type background correction. The binding energy of the C 1s peak was shifted to 284.5 eV as a reference for all curves. The position and full width at half maximum (Lorentzian-Gaussian) of the peaks for the C–O, carbonyl, and carboxyl groups and the $\pi \rightarrow \pi^*$ transition were allowed to float during the fit optimization. Test samples were prepared in a class-1000 cleanroom by evaporating 1 mL of 20 ppm SWNTs onto 10×10 mm^2 silicon wafers that had been cleaned with a 3:1 mixture of H_2SO_4:H_2O_2 (piranha solution) for 20 min and rinsed thoroughly with DI water. The absorption spectra of the

SWNTs in water were recorded on a Hitachi (model U-4100) UV-vis-NIR spectrophotometer. The reference spectrum for the measurements was DI water. All samples (bundled and individually dispersed) for UV-vis-NIR were stabilized with sodium dodecyl sulfate (SDS) at a concentration of 25 mg/mL prior to data collection.

4. 3.   Results and Discussion

4. 3. 1. Pre-treatment of SWNTs

SWNTs were oxidized in a 3:1 mixture of H_2SO_4:HNO_3 under sonication and at a fixed temperature (25 ºC) to impart a negative charge[144]. Figure 4.1 shows the TEM images of SWNTs after pre-treatment. SWNTs remained in bundles and aggregates after pre-treatment. Moreover, nanotubes are still too hydrophobic and the surface charge is insufficient to sustain a stable dispersion.

Previous work has demonstrated that this moderate pre-treatment merely opens, and then saturates the ends of the nanotubes with carboxylic acid groups (COO^-) and results in negligible damage to tube sidewalls, while the sever sidewall damage normally occurs at elevated temperatures and after prolonged periods of sonication in the oxidative acids[71, 145]. X-ray photoelectron spectroscopy (XPS) confirmed that, while the ratio of oxidized to non-oxidized carbon remained relatively constant, the ratio of COO^- to C–O was, indeed, a function of treatment time, with non-treated SWNTs having (COO^-)/(C–O) = 0.22 and 0.15, 3, 6, and 9 hour treatments yielding (COO^-)/(C–O) = 0.36, 0.45, 0.61 and 0.76, respectively (Figure 4.2). Additionally, comparisons of optical absorption data from non- and pre-treated SWNTs suggest a minor reduction in

the electronic integrity of the nanotubes treated for 0.15 and 3 hours, respectively; however, more harsh pre-treatments of 6 and 9 hours in the oxidative acids result in significant reduction of absorption intensity due to the substantial amount of damages of on the tube sidewalls (Figure 4.3).
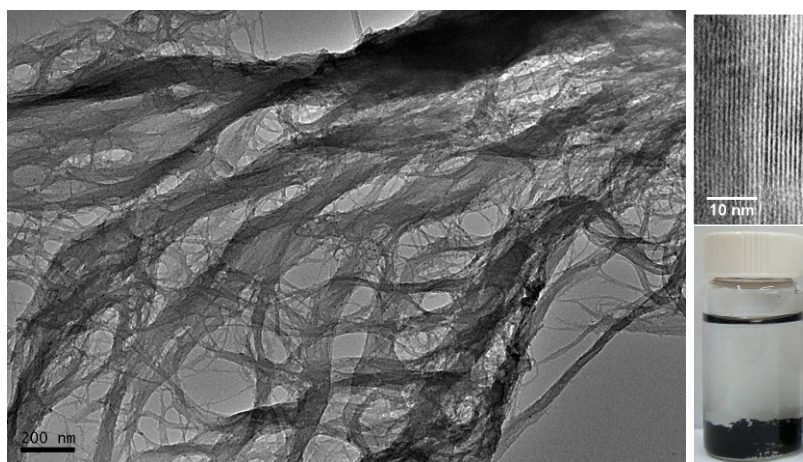
Figure 4.1. (A) Low-magnification and (B) high-magnification TEM image of pre-treated SWNTs. (C) Photographic image of pre-treated SWNTs in water.
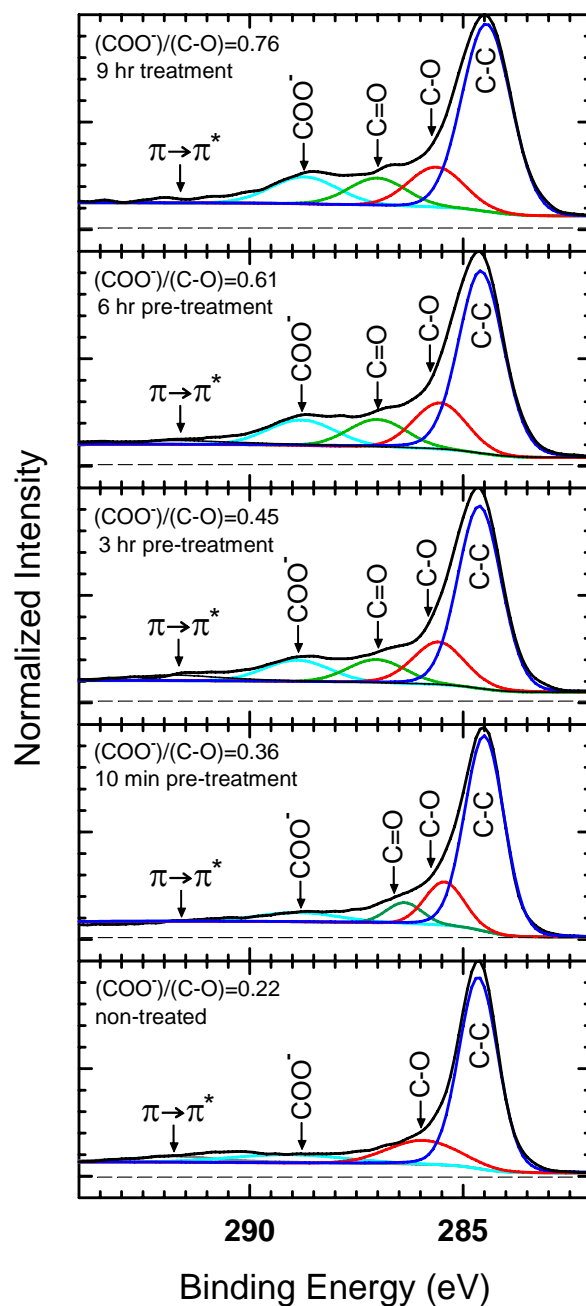
Figure 4.2. XPS spectra of C1s peaks for various oxidative pre-treatment regiments. As oxidation time increases, the ratio of oxidized to non-oxidized carbon remains relatively constant, however the concentration of carboxylic acid groups relative to C–O groups steadily increases with treatment time.
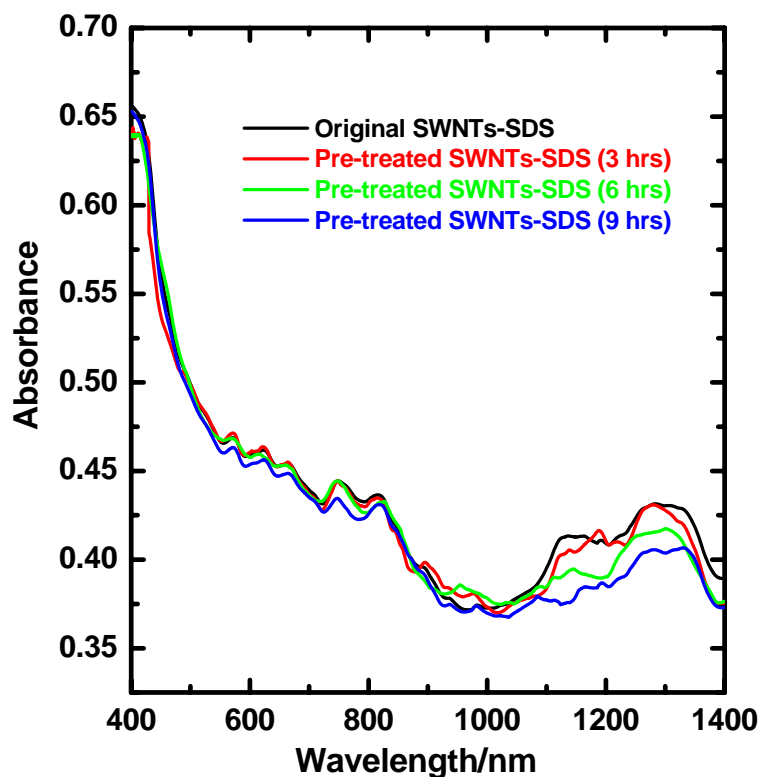
Figure 4.3. UV-vis-NIR absorption spectra of SWNTs with varying degrees of oxidation, showing progressive degradation in electronic properties in the NIR range for longer pre-treatment times. The tubes do not show significant damage for pre-treatments of 3 hours or less.

4. 3. 2. SWNT Debundling and Dispersion using Exfoliated Nanoplatelets

The degree of SWNT dispersion was investigated using 100-nm ZrP nanoplatelets with weight ratios of SWNTs:ZrP = 1:0, 1:0.5, 1:1, 1:3, 1:5, 1:7, and 1:10 and shown through TEM images in Figure 4.4. As can be easily seen, the degree of exfoliation is highly dependent on the number of nanoplatelets available to act on the nanotube aggregates. A full SWNT exfoliation can achieved when SWNTs:ZrP ≤ 1:5. The complete dispersion is highly stable for at least one year (inset in Figure 4.4D).

Larger nanoplatelets with an average diameter of 550 nm were also utilized to investigate the platelet size effect on SWNT dispersion and debundle. A ratio of SWNTs:ZrP ≤ 1:3 was found to attain a completely dispersed state, suggesting a higher efficiency for the larger platelets to disperse SWNTs.
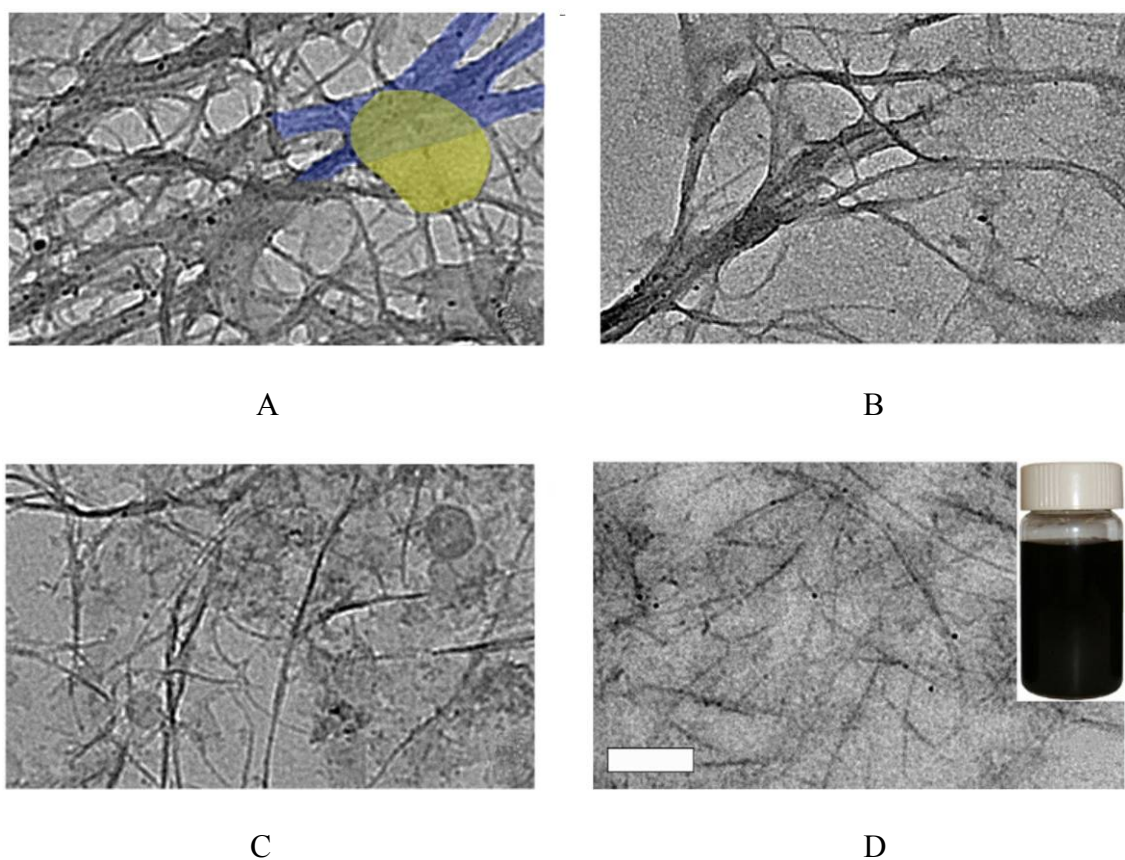
Figure 4.4. TEM images of SWNTs dispersed with 100 nm ZrP platelets at nanotube-to-nanoplatelet weight ratios of (**A**) 1:0.5, (**B**) 1:1, (**C**) 1:3, and (**D**) 1:5. In all cases, ultrasonication was performed for 30 min to pull bundles apart. Scale bar: 200 nm. Shaded regions in (**A**) highlight nanotube bundles (blue) and a single ZrP nanoplatelet (yellow). Inset in (**D**) shows the 1:5 fully exfoliated dispersion after one year of undisturbed suspension.

4. 3. 3. SWNT Debundling and Dispersion Mechanism

The generalized concept behind using exfoliated nanoplatelets to debundle and disperse SWNTs is schematically illustrated in Figure 4.5. The pre-treated SWNTs possess both a negative charge (Figure 4.2). Highly positively charged and exfoliated ZrP nanoplatelets, functionalized with TBA^+, are added to the medium and readily bind to the surface of the negatively charged SWNT bundles through both electrostatic (primarily) and vdW interactions (Figure 4.5B). Due to the large electrostatic binding affinity between these two constituents, the nanoplatelets act in a surfactant-like manner to maximize electrostatic attraction, thereby breaking the large, disordered aggregates (as illustrated in Figure 4.5A) into smaller bundles comprised of highly oriented nanotubes (Figure 4.5C and D). Direct evidence of this surfactant-like stabilization phenomenon is given by the fact that our suspensions of SWNT bundles remain stable for much longer periods after the introduction of positively charged, exfoliated nanoplatelets at lower ionic strengths (<0.1mM) than they do at higher ionic strengths (>1.0 mM), where screening of electrostatic interactions suppresses the magnitude of nanoplatelet binding to nanotube bundles. Furthermore, controlled experiments using pristine ZrP nanoplatelets of the same diameter verified that the addition of negatively charged nanoplatelets functionalized with OH^- surface groups did not affect the stability of the nanotube bundles, due to like-charge repulsion between the SWNTs and nanoplatelets.
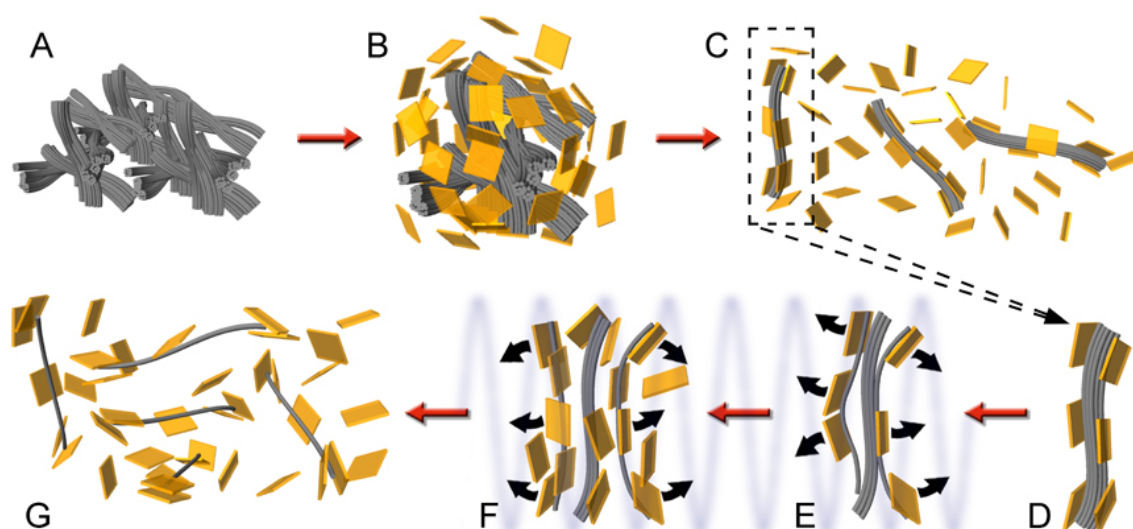
Figure 4.5. Cartoon of proposed mechanism for debundling and dispersing SWNTs with exfoliated nanoplatelets.

In the next step, the dispersion of SWNT bundles with adsorbed ZrP nanoplatelets is sonicated for 30 min and the nanoplatelets absorb the local energy generated by collapsing cavitation bubbles*[146]*, which forces the bound nanoplatelets to translate rapidly and transfer the absorbed energy to the SWNTs. As the average separation between the outer SWNTs tethered to the nanoplatelets and the inner portion of the SWNT bundle increases and approaches a few nanometers, the proximal tube-tube attractive interaction rapidly vanishes*[143]* and the tethered nanotubes are freed from their large bundle (Figure 4.5E and F). Non-adsorbed nanoplatelets in the bulk then bind to the newly exposed SWNT surfaces within the bundle and on the pulled nanotubes (Figure 4.5F). Provided the dispersion is under sonication for at least 30 min, this

process continues until nanotube bundles are broken up into individual tubes or small SWNT bundles (Figure 4.5G), depending on the ratio of nanoplatelets to nanotubes, nanoplatelet diameter, ionic strength of the medium, and duration of the nanotube oxidative pre-treatment. Once the nanotubes are exfoliated they remain stable in the co-dispersion indefinitely, even without the aid of further sonication.

Larger ZrP nanoplatelets (550 nm) are more effective in dispersing the nanotubes into a single-tube state than smaller ones (100 nm). This difference is attributed to the fact that larger nanoplatelets will absorb more sonication energy and that the relatively coordinated, as opposed to fragmented, translation of a longer length of the nanotube is more effective at pulling the tube from the bundle.

4. 3. 4. Characterization of Individual SWNTs

Normally, many spectroscopy techniques such as UV-vis-NIR, photo-luminescence and Raman, electron microscopy such as TEM, and atomic force microscopy are reliable for demonstrating the degree of SWNT dispersion and verifying the individual tubes. In this work, UV-vis-NIR, Raman, and TEM were utilized to demonstrate the existence of individually dispersed SWNTs.

The exfoliated SWNTs were successfully suspended with a wide range of anionic and non-ionic surfactants including polyvinyl pyrrolidone, sodium dodecyl sulphate (SDS), and F108 Pluronic. Cationic surfactants were unsuccessful as hydrophilic stabilizers because the positive head group directly associated with the negative charge on the nanotubes, thus forming a hydrophobic shell with the exposed non-polar tails. In

non-polar media such as chloroform and toluene, however, cationic surfactants functioned well, readily dispersing the nanotubes after nanoplatelet exfoliation. UV-vis-NIR spectra were gathered from multiple samples stabilized with SDS, a small anionic surfactant. The more pronounced, narrower, and blue-shifted absorption peaks of the debundled and SDS-stabilized SWNTs, relative to the spectra of non-exfoliated but pre-treated SDS-stabilized nanotube aggregates (Figure 4.6), strongly suggests the existence of individually dispersed SWNTs*[101]* obtained when this nanoplatelet-assisted dispersion technique is applied. As the degree of packing and aggregation is reduced in SWNT dispersions/suspensions, absorption peaks begin to appear in the NIR range. The more effective the exfoliation, the more pronounced, higher, and blue-shifted the NIR peaks become. Compared to previous literature *[101]*, the UV-vis-NIR spectra here strongly suggest the existence of individually dispersed carbon nanotubes. Moreover, An additional improvement in peak definition within the spectra is observed following the separation of SWNTs from the nanoplatelets with ionic tuning in Figure 4.6.
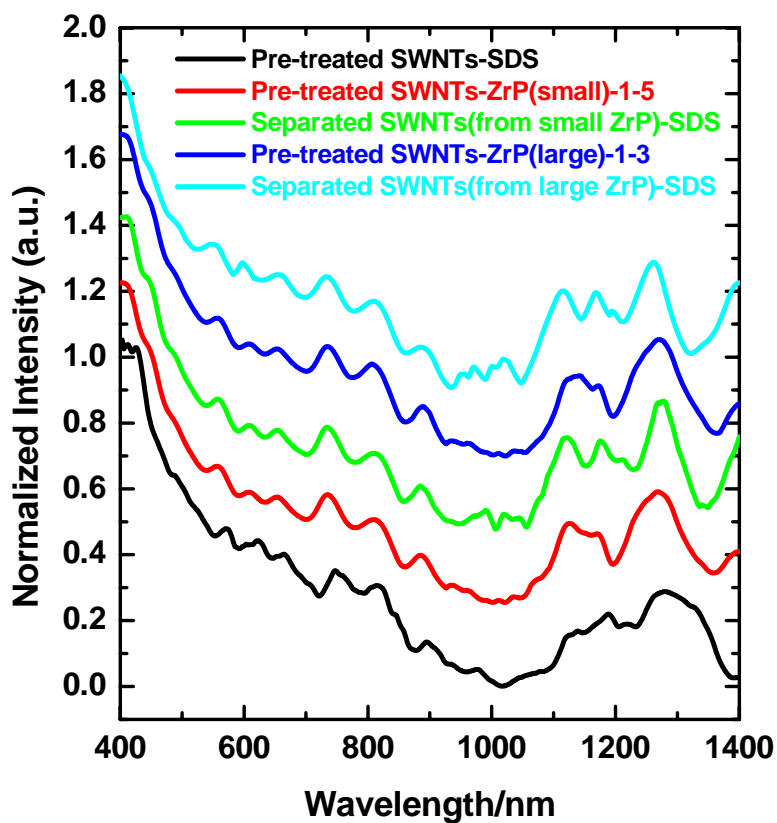
Figure 4.6. UV-vis-NIR spectra of SWNTs

Absorption spectra in Figure 4.7 reveal the differences in magnitude of absorption between 100 and 550 nm ZrP alone and ZrP bound to SWNTs. As can be seen, there is a negligible difference in the spectra of the 100 and 550 nm nanoplatelet-assisted dispersion, and ZrP absorbs very little throughout the entire range.
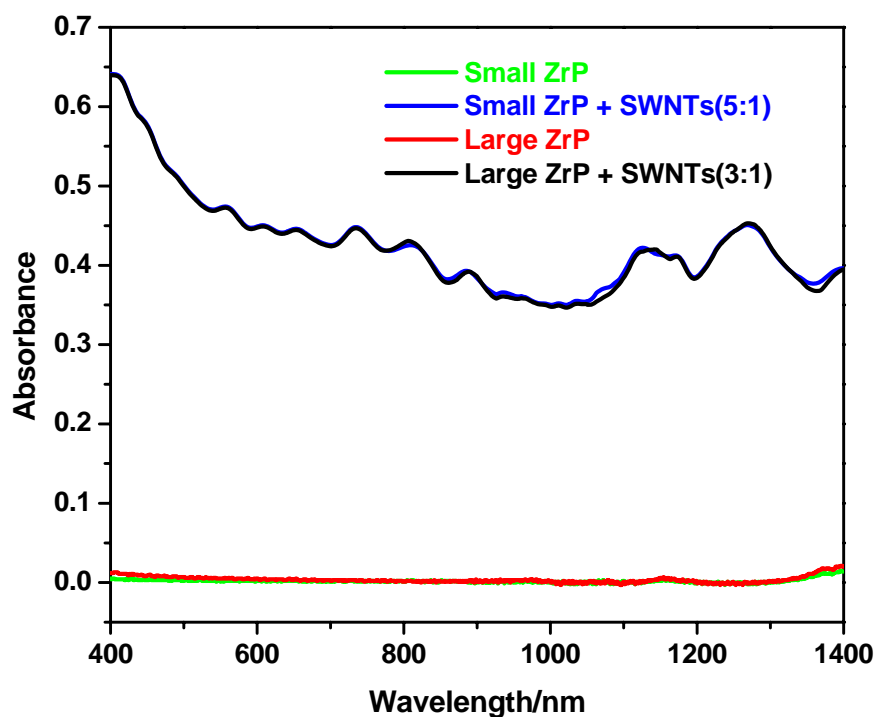
Figure 4.7. UV-Vis-NIR absorption spectra of ZrP and ZrP+SWNTs.

Raman spectroscopy is one of the most widely used tools to study SWNTs. The Raman spectra of SWNTs comprises three distinguished regions: $180 - 300$ cm^{-1}, the Radial Breathing Modes (RBM); ~ 1300 cm^{-1}, defect band (D-band); and 1600 cm^{-1}, tangential G-mode (G-band). D-band indicates the defects on side-walls of SWNTs. Figure 4.8 shows the Raman spectra of SWNTs before and after debundling. The D-band of SWNTs after debundling and separation does not show any obvious change, suggesting that our dispersion and separation process does not cause detectable damage in SWNTs. Therefore, the electronic and mechanical properties are preserved after

debundling. This finding agrees with the XPS (Figure 4.2) and UV-vis-NIR spectroscopic results (Figure 4.6).

When SWNTs are exfoliated, the side-walls are relatively free of vibration compared with their bundle form. This leads to a blue – shifting of G-band in Raman spectrum for individual SWNTs. In Figure 4.8A, the G-band of the debundled and purified SWNTs is found to have blue-shifted by around 10 cm^{-1}, compared to the untreated and pretreated SWNTs. This also demonstrates the effectiveness of this approach to debundle SWNTs.

RBM is a complicated region of Raman spectrum. However, as pointed out in literature for HiPco SWNTs, when bundled, SWNT shows a distinguished peak at around 220 cm^{-1}, which is not the case for individual SWNTs[147]. After debundling through the current approach, the 220 cm^{-1} peak disappears (Figure 4.8B). This experimental observation also demonstrates that this nanoplatelet-assisted dispersion approach can fully exfoliate SWNT bundles into individual tubes.
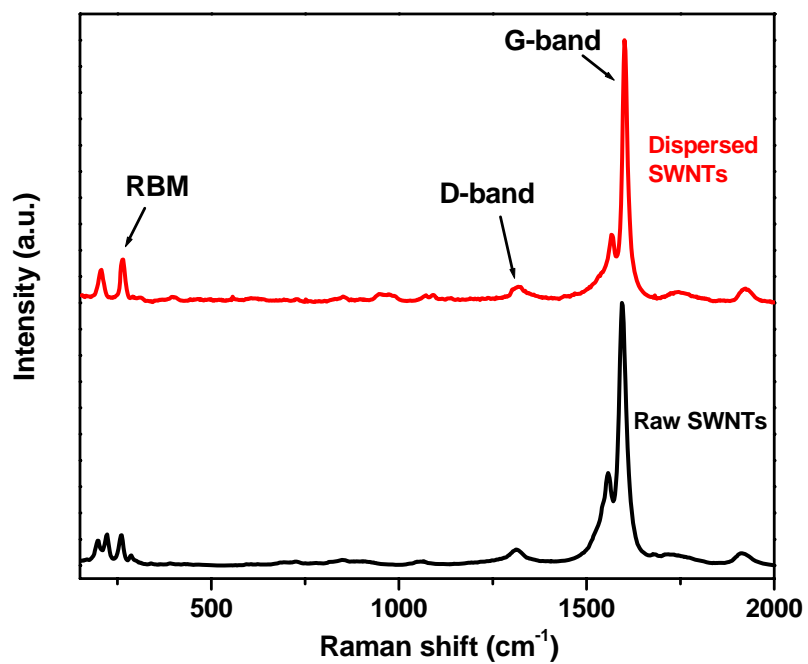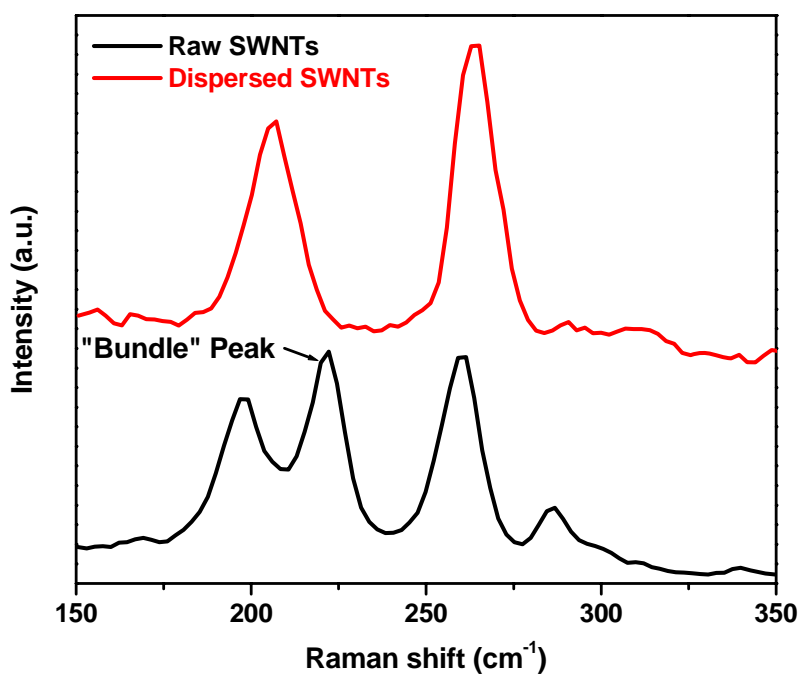
Figure 4.8. (A) Raman spectra of SWNTs. (B) The Radial Breathing Mode (RBM) region of (A).

The difficulty with TEM characterization is that once the nanotubes become more dispersed, their local electron density decreases in the absence of nearby nanotubes, making it difficult to locate individual tubes. By studying TEM images in Figure 4.9a and b, the presence of individual SWNTs is shown. As mentioned before, a key aim in the dispersion process is to minimize or eliminate the damage to tube sidewalls, since it is the primary contributor to the degradation of electrical and physical properties of carbon nanotubes. One clear indicator of tube damage is a reduction in the mean tube length due to scission of C–C bonds. During TEM analysis, the length of individual tubes was verified by tracing the tube under very high magnification. A rough length distribution was generated to validate the lack of damage from our dispersion process in Figure 4.9d. Although a length distribution for the non-treated (as received) SWNTs is not provided because tubes came in tight, aggregated bundles, the estimated lengths are slightly larger those found in previous reports of modified tubes *[148]*.

A log-normal distribution with a probability density function of the form $f(y) = A\left(\sqrt{2\pi}\sigma x\right)^{-1} \exp\left[-\left(\ln\left(x/x_0\right)\right)^2 \Big/ 2\sigma^2\right]$ was used to fit the length data collected from TEM images of 185 tubes, where x_0 is the center of the distribution and was found to be 298 nm for the population in Figure 4.9 c.
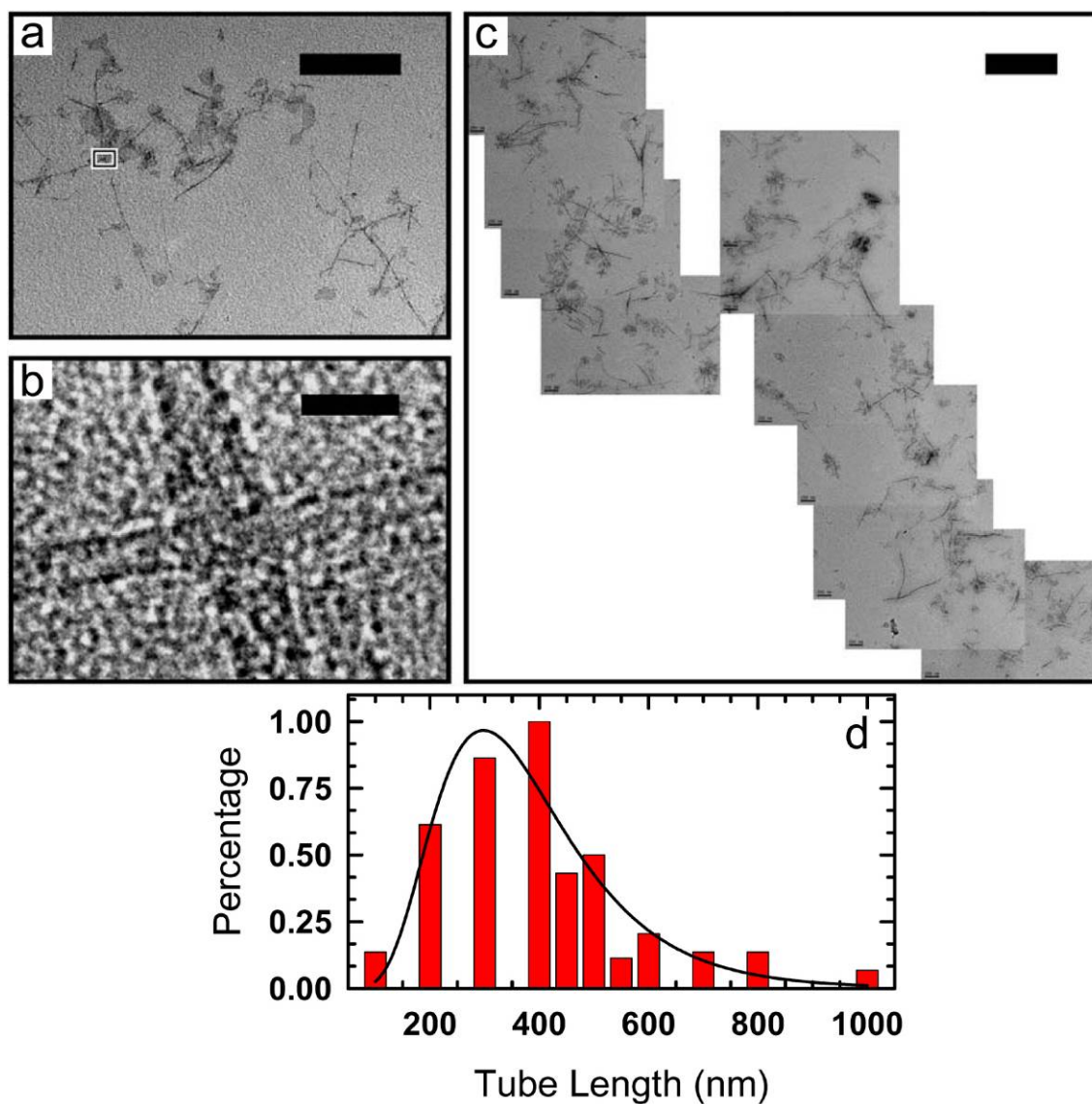
Figure 4.9. TEM image showing dispersed SWNTs. Darker regions in the image are ZrP nanoplatelets that remained after nanotube bundling. **b**, High-magnification image, demarked by the box in **a**, illustrating the overlap of two perpendicular tubes between 1.5 and 2.0 nm in diameter. **c**, Composite created from eleven TEM images showing individually dispersed SWNTs over a large area. **d**, Histogram of 185 tube lengths determined by TEM observations. Scale bars are 500 nm in **a**, 2 nm in **b**, and 1 μm in **c**.

4. 4.   Conclusions

By using exfoliated nanoplatelets, a simple and effective colloidal method has been developed to achieve full exfoliation of SWNTs into individual tubes with preserved physical properties. SWNTs and exfoliated nanoplatelets are first made to bond with each other through electrostatic attraction. In this fashion, nanotubes bundles are physically pulled off into individual tubes by utilizing the nanoplatelets to gather and concentrate the sonication energy onto the nanotube aggregations in a short period of time. The degree of dispersion and debundling is found to depend on the weight ratio between nanoplatelets and SWNTs. Since nanotube side-walls are not chemically modified, this colloidal approach produces fully exfoliated nanotubes with exceptional optical and electrical properties.

CHAPTER V

CARBON NANOTUBE DISPERSION IN POLYMERIC MATRICES

5. 1.   Introduction

Functional polymer nanocomposites containing a small portion of carbon nanotubes (CNTs) have attracted substantial attention in the past decade due to their observed remarkable enhancements in mechanical properties,*[116, 149, 150]* thermal conductivity,*[151]* flame retardancy,*[152, 153]* electrical property,*[154, 155]* and light weight. Similarly to polymer nanocomposites containing other types of nanofillers such as nanoparticles and nanoplatelets, the properties of polymer/CNT nanocomposites strongly depend on the dispersion state. In case of mechanical properties, CNTs are small but known to be stiff and have an extremely high aspect ratio (>1000). Therefore, CNT-containing nanocomposites, when well-dispersed, are expected to be much tougher and stronger than the neat polymer matrices. However, CNTs are insoluble in any known solvents or polymers. Without further modification, they inevitably entangle with each other due to their one-dimensional nature and form large aggregates when mixed with polymers, which dramatically reduces the interfacial area between CNTs and polymer matrices and can even create defects. In such a fashion, significant improvements in mechanical properties of the polymer composites would not be observed. As for the electrical properties, aggregation of CNTs in polymers results in a high tube concentration to reach the conductivity threshold (percolation). Because of this dispersion challenge and the potential benefits of well-dispersed CNT-based polymer

nanocomposites for functional and structural applications, a considerable amount of research effort has been made to improve the dispersion of CNTs in polymers over the past ten years.

Methods to disperse CNTs in polymer matrices include direct melt-mixing of polymers with raw or stabilized/functionalized CNTs, solution-mixing of dissolved polymers with dispersed CNTs, in-situ polymerization of monomers with functionalized CNTs. A detailed literature review on these methods can be found in **Chapter II**. It should be noted that the melt-mixing method is most straightforward and economical, but the quality of dispersion is limited; usually better dispersion can be achieved by solution-mixing and by in-situ polymerization. It has been demonstrated that CNTs can be well dispersed in water through ultrasonication-assisted surfactant stabilization or polymer wrapping.*[72, 103]* This facilitates the incorporation of CNTs in water-soluble thermoplastics. Surface-functionalization of CNTs with organo-philic groups has been shown to be an effective method to achieve good dispersion of CNTs in hydrophobic polymers.*[122, 156]* Significant improvements in mechanical and electrical properties have indeed been observed in well-dispersed polymer/CNT nanocomposites prepared through these methods. For example, water-soluble polyvinyl alcohol reinforced by surfactant-stabilized and polymer-wrapped single-walled CNTs (SWNTs) at 5 weight % (wt.%) shows an around 100 % increase in both tensile strength and modulus.*[120]* Polyacrylonitrile/SWNT nanocomposites (up to 10 wt%) prepared through solution spinning exhibit 100 % higher tensile modulus than the neat matrix.*[157]* In-situ polymerization of nylon with surface-functionalized SWNTs also results in over 100%

increase in both tensile strength and modulus.*[125]* Incorporation of fluorinated SWNTs (1 wt.%) into an epoxy matrix exhibits 30% increase in Young's modulus and 18% increase in tensile strength.*[126]*

However, the aqueous mixing and organophlic-functionalization methods are not suitable for large-scale preparation of polymer/CNT nanocomposites, especially for structural applications. Firstly, most of the thermoplastics and almost all commonly used epoxies are hydrophobic. Secondly, surface-functionalization of CNTs normally involved complex steps and can be expensive. Therefore, it is not practical to prepare polymer/CNT nanocomposites for structural applications. Moreover, literature results show that, to achieve a meaningful reinforcing effect on the polymer matrices, relatively high CNT concentrations of >1 weight % (wt.%) are generally needed. Therefore it is highly desirable to improve the CNT dispersion in polymer matrices so that high performance polymer/CNT nanocomposites can be obtained at low CNT concentrations, thus at low cost. In this chapter, based on the nanoplatelet-assisted CNT dispersion described in the last chapter, a simple and cost-effective approach to disperse CNT in polymer matrices especially in epoxy is introduced. This method can easily transfer the aqueous dispersion of CNTs to organic solvents so that well-dispersed epoxy/nanocomposites can be prepared. Individually dispersed CNTs including SWNTs and multi-walled CNTs (MWNTs) have been observed. Epoxy nanocomposites containing well-dispersed MWNTs show exceptional mechanical properties at low CNT loadings. High-performance polymer nanocomposites can therefore be prepared at low cost and are suitable for engineering applications.

5. 2.   Experimental

5. 2. 1. Materials

ZrP nanoplatelets were synthesized using a refluxing method and exfoliated according to the methods described in **Chapter III**. The diameter of ZrP nanoplatelets used in this study is around 100 nm.

XD grade SWNTs with contains 1/3 of few-walled CNTs and 2/3 SWNTs (XD-CNTs) were obtained from Carbon Nanotechnologies, Inc. (Houston, TX). MWNTs were purchased from Aldrich. XD-SWNTs were pre-treated using the same approach for HiPCO SWNTs described in the previous chapter. MWNTs were pre-treated similarly except that they were oxidized for only 2 hours.

5. 2. 2. CNT Dispersion in Water and Organic Solvents

Two aqueous solutions containing oxidized CNTs (both XD-SWNTs and MWNTs) and fully exfoliated ZrP nanoplatelets were directly mixed with various weight ratios of CNTs to ZrP nanoplatelets. The mixtures were sonicated in a sonication bath (Branson 2510) maintained at room temperature for 30 min. After dispersion, the aqueous mixtures were dried on a hot plate at 100 °C for several hours with stirring until all water was removed. The residues were then redispersed in acetone or THF by ultrasonication for 5-10 min with concentrations up to 5 mg/mL.

5. 2. 3. Preparation of Epoxy Nanocomposites

Epoxy nanocomposites containing MWNTs were prepared using solution mixing. The acetone suspensions with ZrP-to-MWNT (ZrP/MWNT) weight ratio of 5 were mixed with epoxy monomer (diglycidyl ether of bisphenol-A, D.E.R.™ 332 epoxy resin, The Dow Chemical Company) to achieve a finial CNT concentration of 0.2 and 0.4 wt% in epoxy nanocomposites. The ZrP concentrations were 1.0 and 2.0 wt.%, respectively. The solvents were then removed *via* rotary evaporation in a water bath at 80 °C and curing agent, 4,4'-diamino-diphenyl sulfone (DDS, Aldrich) was added at a stoichiometric ratio. This mixture was heated up rapidly to 130 °C until the DDS was dissolved and then poured into a pre-heated glass mold with mold release agent on the glass mold surfaces. The epoxies were cured in an oven at 180°C for 2 hours, followed by 2 hours of post-cure at 220°C. For comparison purposes, neat epoxy sample was also prepared using the same curing procedure.

Epoxy/XD-SWNTs were prepared using the same approach except for the curing agent and curing condition. EPICURE W (Miller – Stephenson, Inc.) , a liquid curing agent at room temperature, was mixed with the epoxy resin containing MWNTs and ZrP at 80 °C after solvent evaporation. The curing temperature was 120 °C for 2 hours, followed by 2 hours of post-cure at 175°C. A neat epoxy samples was also prepared using the same curing procedure.

5. 2. 4. Characterization

Transmission electron microscopy (TEM) was performed using a JEOL 2010 high-resolution transmission electron microscope, operated at 200 kV. The solution samples were coated onto carbon grids and were then dried at room temperature. A Reichert-Jung Ultracut-E microtome was utilized to prepare thin sections of epoxy nanocomposites with thickness of 70-100 nm for TEM imaging. SEM was acquired using a Zeiss Leo 1530 VP Field Emission-SEM (FE-SEM). X-ray diffraction (XRD) patterns were recorded using a Bruker D8 Advanced Powder X-ray Diffractometer with Cu-K$_\alpha$ incident radiation ($\lambda = 1.5418$ Å).

5. 2. 5. Mechanical Testing

Tensile properties of the epoxy samples were obtained through the ASTM D638-98 method. The tensile tests were performed using an MTS$^\circledR$ servo-hydraulic test machine at a crosshead speed of 5.08 mm/min at ambient temperature. Young's modulus, tensile strength, and elongation at break of each sample were obtained based on at least five specimens and the average values and standard deviations were reported.

5. 3.   Results and Discussion

5. 3. 1. Dispersion of CNTs Using Exfoliated ZrP Nanoplatelets in Water

The methodology and mechanism of dispersing XD-SWNTs in water using exfoliated ZrP nanoplatelets are the same as the case of HipCo SWNTs dispersion discussed in the last chapter. In the case of MWNTs, the mechanism is slightly different

because normally MWNTs do not form bundles; therefore, the MWNT dispersion using exfoliated ZrP nanoplatelets only involves the disentanglement of MWNT aggregates. Figure 5.1 shows the TEM images of XD-SWNTs and MWNTs after pre-treatment. Similar to the HipCO SWNTs used in the last chapter, XD-CNTs form large bundles or ropes that entangle with each other while MWNTs only form large entanglements.
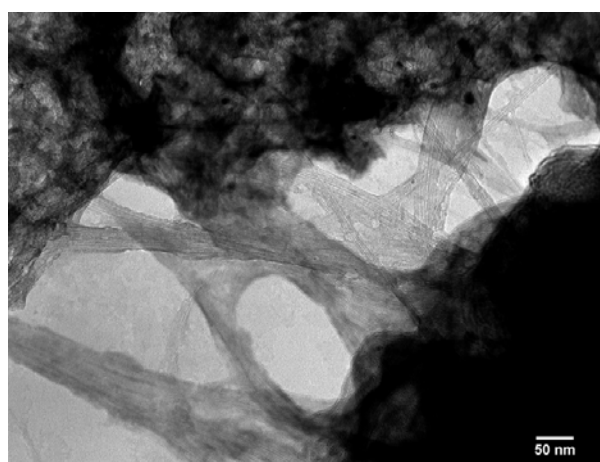
A
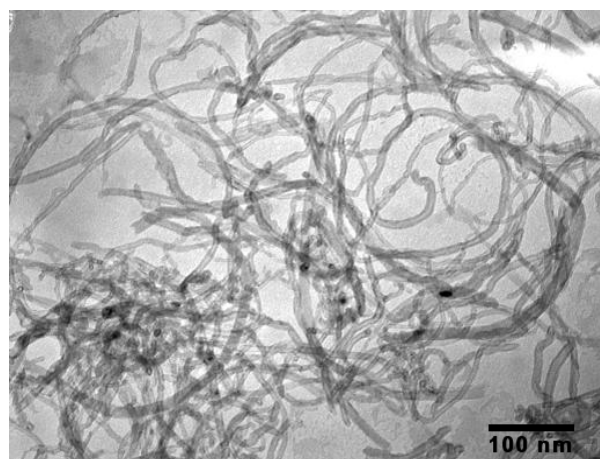
B

Figure 5.1. TEM images of (A) pre-treated XD-CNTs and (B) MWNTs.

Figure 5.2 shows the TEM images of XD-CNTs after dispersion using exfoliated ZrP nanoplatelets. SWNTs in XD-CNTs have been fully exfoliated into individual tubes and MWNTs have been completely disentangled with the ZrP/CNT weight ratio = 5. It should be noted that after dispersion and debundling, XD-CNTs tubes become straight due to less defects present on the nanotube side-walls.
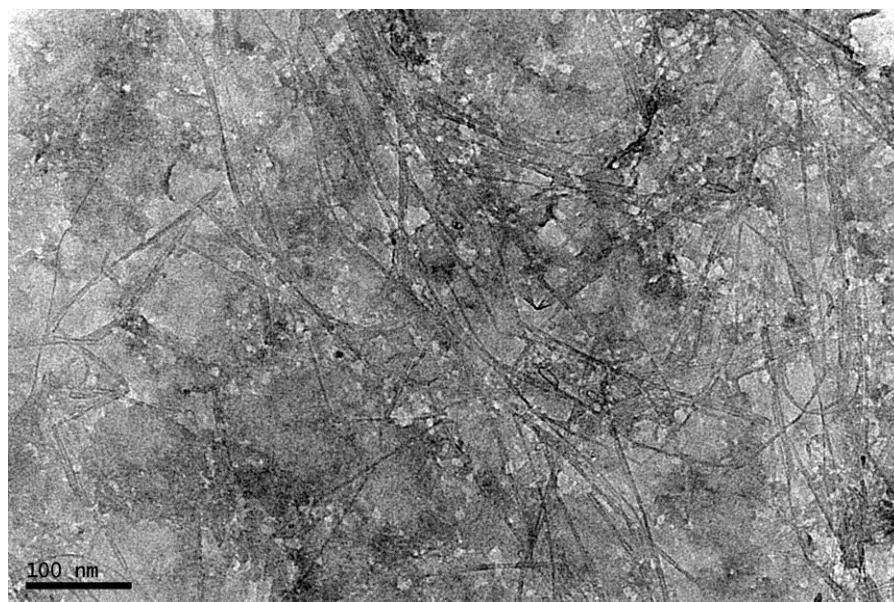
Figure 5.2. TEM images of XD-SWNTs after dispersion using exfoliated ZrP nanoplatelets

5. 3. 2. Redispersion of CNTs into Organic Solvents

A simple drying-redispersion approach was developed to transfer the CNT from aqueous suspension to organic solvents. Homogeneous dispersions of CNTs and ZrP

nanoplatelets with the weight ratio higher than 5 were obtained and can maintain stability for over 1 year in the organic solvents, such as acetone and THF.

The redispersion mechanism and the optimal ZrP/CNT weight ratio to achieve a full redispersion were obtained by performing XRD on the dried hybrid solids with ZrP/CNT weight ratios and are depicted in Figure 5.3. It is well-known that exfoliated nanoplatelets irreversibly restack into a layered structure upon drying (curve **a** in Figure 3). However, with the presence of CNTs, the nanoplatelet restacking process can be significantly disrupted, as suggested by the XRD of the dried hybrid mixture of ZrP nanoplatelets and CNTs with a weight ratio of 5 (curve **b** in Figure 5.3). The absence of the diffraction peaks from the layered structure is caused by a full inter-mixing between the exfoliated ZrP nanoplatelets and the dispersed CNTs through electrostatic attraction. The hybrid solids with the weight ratio of ZrP/CNT < 5 cannot lead to full redispersion of CNTs as illustrated by the observation of the CNT aggregates after mixing with acetone or THF. When the weight ratio of ZrP/CNT > 5, the diffraction peaks from the layered structure of the restacked ZrP nanoplatelets reappear (curves **c** and **d** in Figure 5.3), which is due to the presence of excessive exfoliated nanoplatelets. Therefore, a full exfoliation of ZrP nanoplatelets in the redispersed organic suspensions cannot be achieved from the hybrid solids with the weight ratio of ZrP/CNT higher than 5 under the current preparation condition. The possible morphologies of the dried solids containing different weight ratios between CNTs and ZrP nanoplatelets are depicted in the insets of Figure 5.3. The above results also demonstrate that a weight ratio of 5

between exfoliated ZrP nanoplatelets and CNTs is an optimal ratio to achieve full dispersion of both.
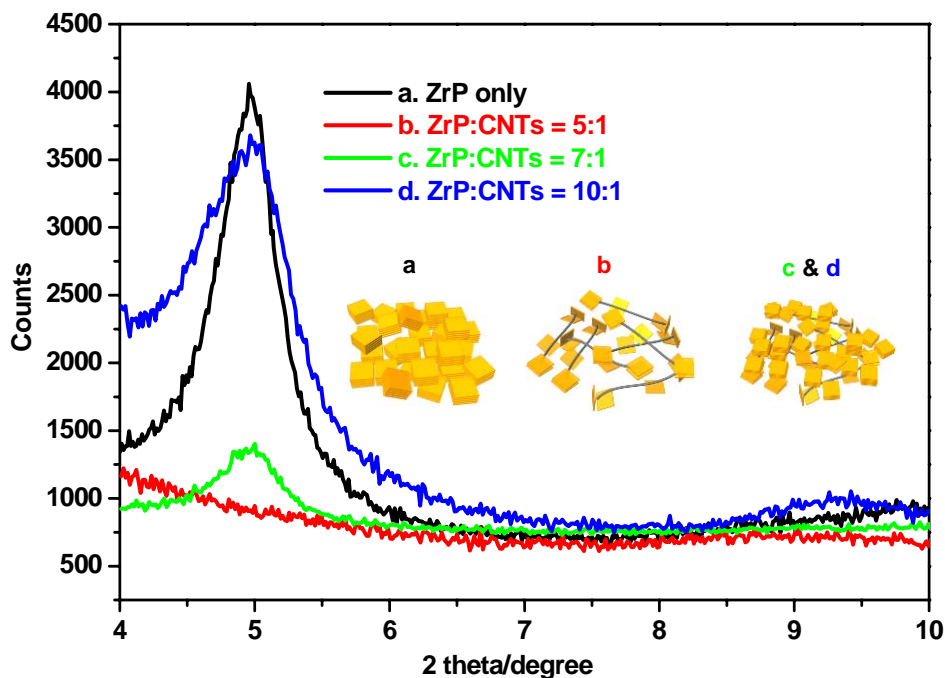
Figure 5.3. XRD patterns of the hybrid solids containing ZrP nanoplatelets and CNTs with different weight ratios prepared by drying aqueous suspensions. The inset cartoons show the possible morphologies of each hybrid solid.

5. 3. 3. Epoxy/CNT Nanocomposites

Epoxy nanocomposites containing full dispersion of both ZrP nanoplatelets and XD-SWNTs were prepared by solution mixing using the redispersed acetone suspensions at weight ratio of ZrP/CNT = 5. Figure 5.4 shows the TEM of the epoxy nanocomposites with different CNT concentrations. Both XD-SWNTs and ZrP

nanoplatelets are fully exfoliated and well-dispersed in the polymer matrix. It is interesting to note that XD-SWNT tubes appear to be straight inside epoxy matrix.
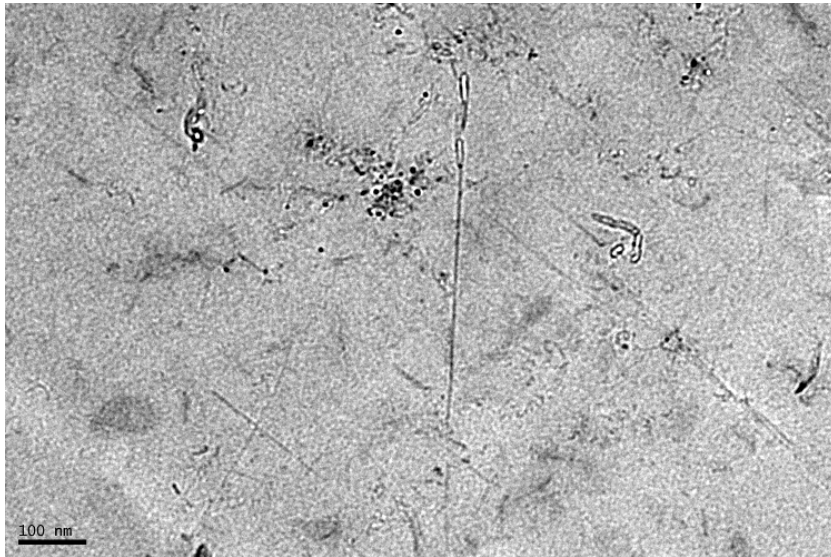
A
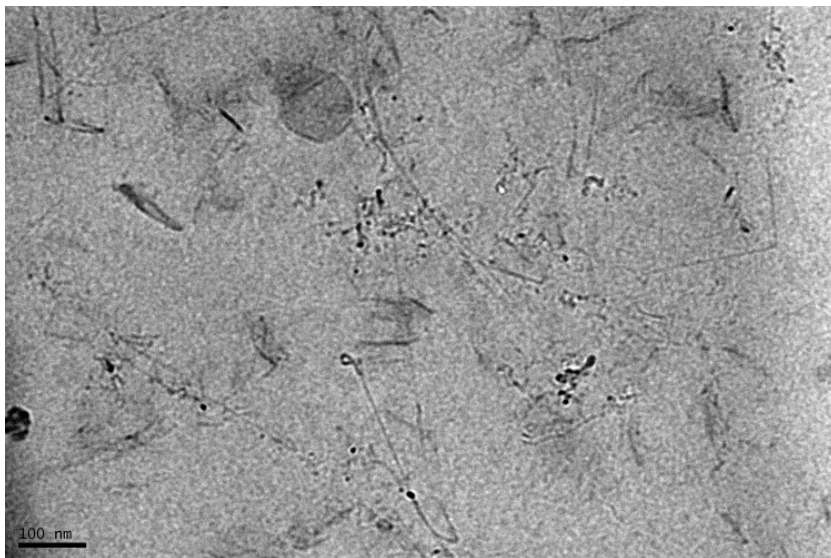
B

Figure 5.4. TEM of epoxy nanocomposites containing (A) 0.2 wt.% and (B) 0.4 wt.% of XD-CNTs.

Figure 5.5 shows the TEM images of epoxy nanocomposites with 0.2 and 0.4 wt.% of MWNTs. The concentrations of exfoliated nanoplatelets are 1.0 and 2.0 wt.%, respectively. Well-dispersed MWNTs and full exfoliation of nanoplatelets can be observed.

A few literature reports have shown the efficacy of using clay nanoplatelets to disperse CNTs into polymer matrices.*[158-160]* It was suggested that due to the interaction between CNTs and clay particles, large CNT aggregates would break into small segregates to become well dispersed in polymers. However, clay particles were still found to form stacked morphology and CNTs were also not completely disentangled. The TEM images shown here clearly suggest that through the aqueous dispersion – drying – organic redispersion approach, both CNTs and nanoplatelets can be fully dispersed down to individual tube level in epoxy matrices. The most important reason for achieving such a good dispersion is the proper manipulation of the surface characteristics of both CNTs and nanoplatelets such that they exhibit strong affinity with each other due to the electrostatic attraction between opposite charges.
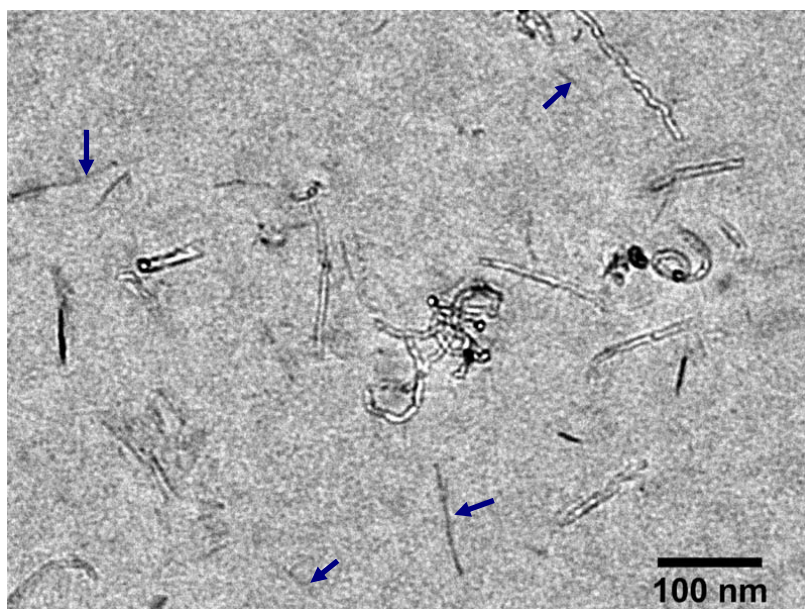
A
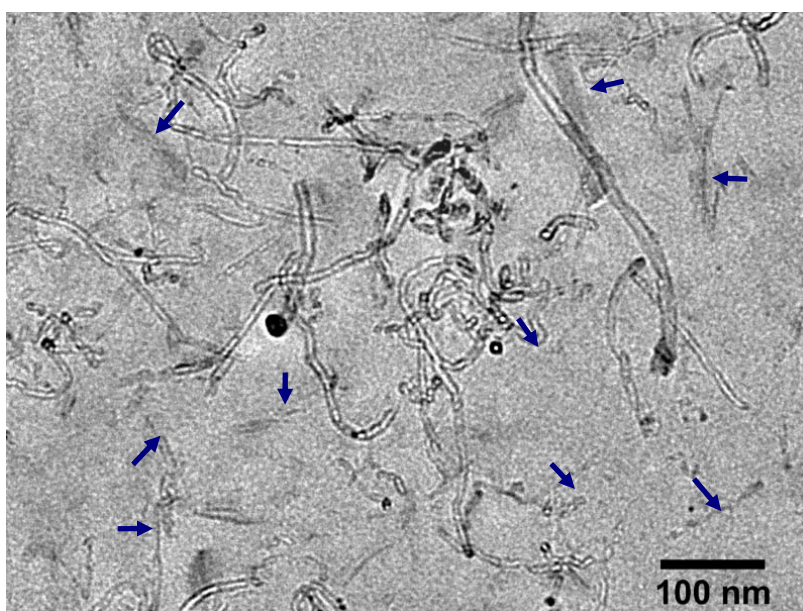
B

Figure 5.5. TEM of epoxy nanocomposites containing (A) 0.2 wt.% and (B) 0.4 wt.% of MWNTs.

5. 3. 4. Mechanical Properties of Epoxy/CNT Nanocomposites

CNT-reinforced polymer nanocomposites can show over 100% increasing in Young's modulus and tensile strength. However, such superior mechanical properties have only been observed in thermoplastic polymers. In the case of brittle thermosetting polymers, such as epoxy, the improvement in mechanical properties using CNTs is limited. For example, Epoxy/SWNT nanocomposites at 0.5 wt.% loading prepared through solution mixing only shows less than 20% and 10% increase in flexural modulus and strength, respectively.*[161]* One main reason is the lack of a simple and effective method to well disperse CNTs in the epoxy matrices, especially down to individual level.

The stress – strain curves of the neat epoxy and epoxy nanocomposites containing individually dispersed MWNTs and nanoplatelets from the tensile testing are shown in Figure 5.6. The Young's modulus, tensile strength, and elongation at break of the neat epoxy and epoxy nanocomposites are listed in Table 5.1. The neat epoxy has a Young's modulus of 3.04 GPa, a tensile strength of 75.3 Mpa, and an elongation at break of 3.7%. Both of the epoxy nanocomposites exhibit higher Young's modulus, tensile strength, and elongation at break. The epoxy nanocomposite containing 0.4 wt.% of MWNTs and 2.0 wt.% of exfoliated ZrP nanoplatelets exhibits an impressive improvement in mechanical properties, having 41% increase in Young's modulus, 55% increase in tensile strength, and 24% increase in elongation at break, respectively. The above findings are considered to be significant when compared against what have been shown in the literature; with 1-4 wt.% addition of CNT in brittle epoxy, only 10-30 % increase in modulus and strength were reported.
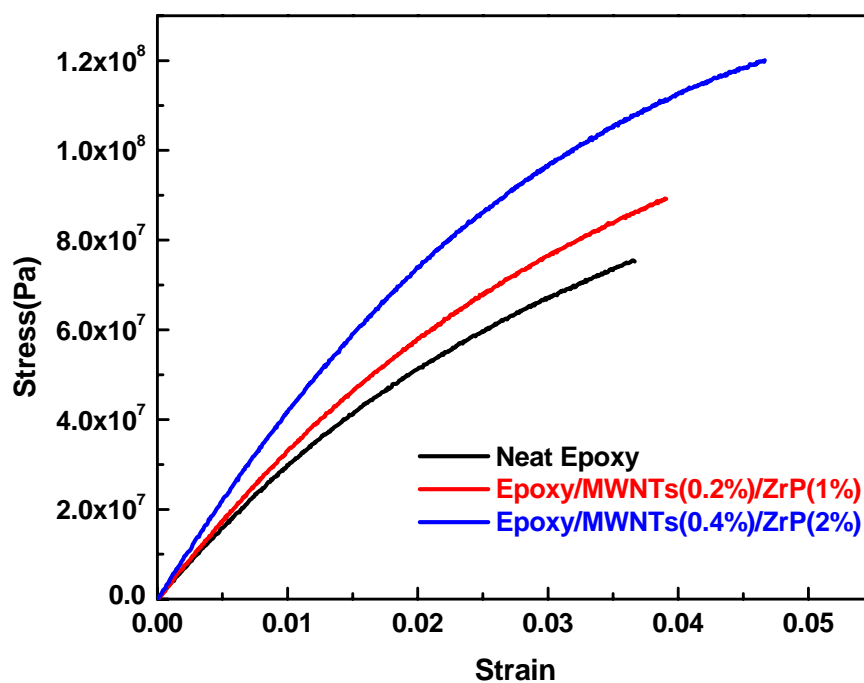
Figure 5.6. Stress – strain curves of the neat epoxy and epoxy nanocomposites containing exfoliated ZrP nanoplatelets and MWNTs.

Table 5.1. Mechanical properties of the neat epoxy and epoxy nanocomposites containing exfoliated ZrP nanoplatelets and MWNTs.

	Neat Epoxy	Epoxy/CNTs(0.2%) /ZrP(1.0%)	Epoxy/CNTs(0.4%) /ZrP(2.0%)
Young's Modulus (GPa)	3.04±0.04	3.40±0.06	4.27±0.07
Tensile Strength (MPa)	75.3±4.2	83.1±4.8	116±5.5
Elongation at Break (%)	3.7±0.1	3.9±0.3	4.3±0.4

Figure 5.7 shows the stress – strain curves of the neat epoxy and epoxy nanocomposites containing individually dispersed XD-CNTs and exfoliated ZrP nanoplatelets from the tensile tests. The mechanical data are listed in Table 5.2. Compared to epoxy/MWNTs nanocomposites, the improvements in Young's modulus and tensile strength using XD-CNTs is less effective with only 17 % increase in Young's modulus and 11 % increase in tensile strength at 0.4 wt.% of XD-CNTs and 2.0 wt.% of ZrP nanoplatelets. However, the epoxy nanocomposite shows up to 44% increase in elongation at break when 0.4 wt.% of XD-CNTs is incorporated , suggesting that C-SWNTs are more effective in improving the ductility of the epoxy matrix than MWNTs (24 % increase in elongation at break using the same CNT and ZrP concentrations).

The mechanical data in this study suggest that epoxy nanocomposites containing well-dispersed CNTs and exfoliated inorganic nanoplatelets show excellent mechanical strength and modulus without compromising their toughness and ductility. In many other reported polymer nanocomposite systems containing inorganic particles, especially for epoxies, an improvement of both modulus and strength concurs with a reduction of toughness and ductility. For example, studies on using ZrP nanoplatelets alone to strengthen epoxy shows that only a slight increase in modulus was observed, while reduction in ductility and strength was found.[162] Moreover, some literature results on polymer/CNT nanocomposites show an improvement in modulus and strength, but with the reduction of ductility, especially in epoxy.[126, 161] One possible reason why the epoxy nanocomposites containing CNTs and inorganic ZrP nanoplatelets can improve both strength and ductility is the synergistic effect from the 1-dimensional and 2-

dimensional inorganic fillers that are both well dispersed in polymer matrices down to nano-scale.

The mechanical results here also suggest that with the existence of exfoliated nanoplatelets, MWNTs are more effective in the strengthening of epoxy nanocomposites than SWNTs. One possible explanation is that MWNTs are generally much longer and have a higher aspect ratio than SWNTs, which are more effective in improving the mechanical properties of the matrices.
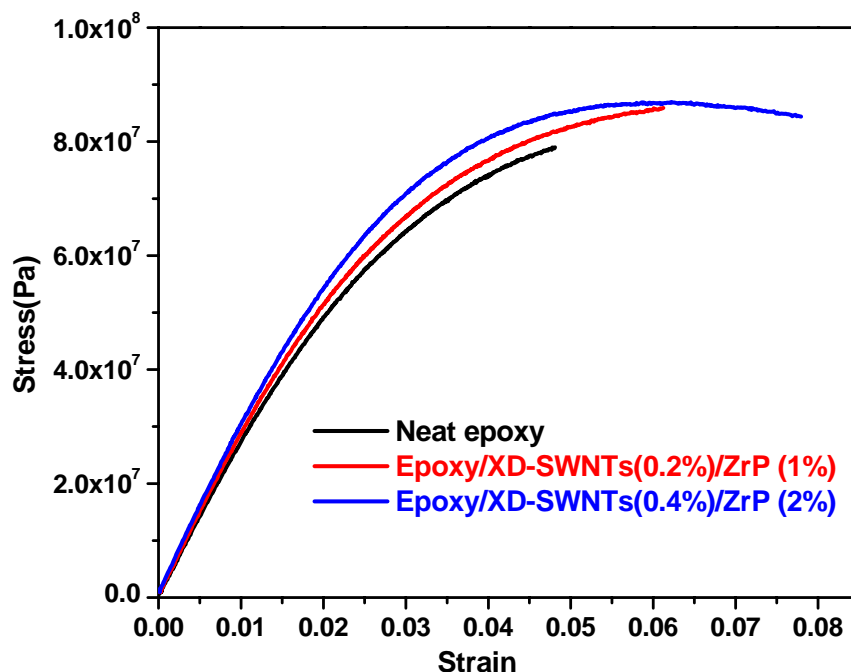
Figure 5.7. Stress – strain curves of the neat epoxy and epoxy nanocomposites containing exfoliated ZrP nanoplatelets and XD-CNTs.

Table 5.2. Mechanical properties of the neat epoxy and epoxy nanocomposites containing exfoliated ZrP nanoplatelets and XD-CNTs.

	Neat Epoxy	Epoxy/XD-CNTs(0.2%) /ZrP(1.0%)	Epoxy/XD-CNTs(0.4%) /ZrP(2.0%)
Young's Modulus (GPa)	2.71±0.04	2.89±0.08	3.19±0.05
Tensile Strength (MPa)	77.9±3.2	83.5±3.6	86.5±5.5
Elongation at Break (%)	4.8±0.1	5.6±0.2	6.9±0.3

5. 4.   Conclusions

By utilizing exfoliated inorganic nanoplatelets, a simple and effective method to fabricate epoxy nanocomposites containing CNTs has been introduced. Through the strong electrostatic affinity between exfoliated inorganic nanoplatelets and CNTs, the excellent dispersion of CNTs in aqueous suspensions can be easily transferred to organic solvents for the preparation of exfoliated epoxy nanocomposites. The epoxy nanocomposites containing well-dispersed CNTs and exfoliated inorganic nanoplatelets show superior modulus, strength and ductility at a low CNT loading. Such kind of low cost, high performance epoxy nanocomposites are ideal for engineering structural applications.

CHAPTER VI

SYNTHESIS OF 0-DIMENSIONAL MONODISPERSE ZNO QUANTUM DOTS

AND THEIR DISPERSION IN ALCOHOL AND WATER[*]

6. 1.   Introduction

Zinc oxide (ZnO) semiconductor has drawn enormous attention due to its unique properties in optics, photonics and electronics *[163]*. Its wide bandgap (3.4 eV) and high exciton binding energy (60 meV) at room temperature are ideal for short wavelength light-emitting applications. ZnO is a transparent semiconductor and can be widely doped with tunable electrical properties. Therefore, it has been considered to be a potential substitution for ITO. ZnO is also an excellent UV absorber, which can effectively absorb UVA and UVB from sunlights. It has been widely adapted in cosmetics, paintings, and coatings for UV protection. Moreover, as the size of ZnO is reduced to a few nanometers, it shows size- and shape-dependent properties, known as quantum size effects, which opens up a promising way to further tune its properties for broader potentials. Recent development on the ZnO nanostructure-based nanogenerators demonstrates its ability to convert mechanical vibrations into electricity due to the nanopiezotronical effect *[164]*. Furthermore, ZnO nanoparticles have also been shown to be promising for harvesting solar energy.

The methods to synthesize ZnO nanostructures include chemical vapor deposition (CVD), physical vapor deposition (PVD), molecular beam epitaxy (MBE), and solution-based synthesis *[165]*. Colloidal synthesis has many advantages over other methods such as simple, low temperature thus energy efficient, low cost, easy to control size and shape, and suitable for devicefabrication *[166]*. Recent progress on the synthesis of ZnO using the vapor deposition methods has demonstrated the richness in the diversity of its nano-structures such as spherical nano-sized particles or quantum dots, one-dimensional (1D) nanorods or nanowires, nanocombs, nanorings, nanohelixes/ nanosprings, nanobelts, and nanocages *[167]*. However, colloidal synthesis is still one major method to prepare simple and low-dimensional ZnO nanostructures such as spherical nanoparticles/QDs and nanorods.

Research on colloidal ZnO nanoparticles began in the late 1980s. Koch et al *[168]*, Bahnemann et al *[29]*, and Haase et al *[32]* first used the colloidal method to prepare ZnO QDs by hydrolyzing zinc salts in basic alcoholic solutions. In 1991, Spanhel and Anderson *[7]* systematically studied the growth of colloidal ZnO nanoparticles by using zinc acetate dihydrate $(Zn(Ac)_2 \cdot 2H_2O)$ and lithium hydroxide as the starting materials and ethanol as the solvent. Since then, this route has been widely adopted to prepare ZnO nanoparticles *[169-176]*.

In the current study, ZnO nanoparticles with sizes ranging from 2 to 8 nm (QDs) are prepared in methanol. The synthesis of colloidal ZnO nanoparticles can be carried out in different types of alcoholic solutions, i.e., methanol, ethanol, propanol or higher alcohols. The unique features of methanol over other alcohols in synthesizing colloidal

ZnO nanoparticles involve its high dielectric constant and low ligand affinity. The dielectric constant of a solvent primarily determines its polarity. Usually, the higher the dielectric constant is, the higher the polarity of the solvent. The dielectric constants of methanol, ethanol and isopropanol are 32.66, 24.55, and 19.92 *[177]*, respectively. On one hand, electrolytic salts have high solubility in high-polarity solvents, but are generally hard to be dissolved in non-polar solvents, known as "like dissolves like". For example, $Zn(Ac)_2 \cdot 2H_2O$, the most commonly used zinc salt for synthesizing colloidal ZnO nanoparticles, has a higher solubility in methanol than in other alcohols. On the other hand, methanol, with a higher polarity, gives rise to a faster formation of ZnO nanoparticles than in ethanol under non-basic condition *[178]*, which makes methanol very useful for the preparation of colloidal ZnO nanoparticles. During the growth of colloidal ZnO nanoparticles, the alcohols not only provide the medium for the reactions, but also act as ligands to help control the morphology of ZnO *[11]*, i.e., particles or rods. Under hydrothermal conditions, ZnO has a higher tendency to form rods in ethanol than in methanol *[179]*, which makes methanol a good solvent for growing spherical ZnO nanocrystals. Moreover, methanol is a good solvent for dissolving quite a few monomers and polymers *[180]*. Therefore direct handling of colloidal ZnO nanoparticles in methanol can offer more versatility for the preparation of polymer/ZnO nanocomposites.

It should be noted that QDs are a type of nanoparticles that show quantum size effect, that is, the properties of a semiconductor, especially optical and electrical properties, are a functional of the particle size. As for ZnO, it shows such effect when its size is smaller than 7-8 nm.

Dispersing QDs in water is one of the major efforts in the QD research area. QDs are known to be highly luminescent and have a high quantum yield (>95%). They are also environmentally stable because they are inorganic. These advantages make QDs ideal for biological detection and sensor applications. However, QDs are extremely hydrophobic; therefore, aqueous dispersion of QDs is a difficult task to overcome. Many types of amphiphilic surfactants and ligands have been used and synthesized for this purpose. A detailed literature review can be found in **Chapter II**. However, many surfactants and ligands are expensive and some of them are difficult to synthesize. Therefore, it is highly desirable to develop a simple and low-cost method to produce water-soluble QDs.

In the current study, highly crystalline ZnO QDs were synthesized by hydrolyzing zinc acetate dihydrate in the basic methanol solution. The particle size and distribution as a function of time were studied through UV-vis spectroscopy. Monodisperse ZnO QDs with an average particle size of 5.0 nm were prepared through a size-focusing mechanism by concentrating the reacted solutions. The by-products, such as zinc layered double hydroxide, were also found to be removed by the concentrating process. The impurity ions, including K^+, Ac^-, were effectively removed from the ZnO QDs through a modified precipitation-redispersion method. The purified ZnO QDs can be further stabilized in methanol by adding a small amount of hexane. Water-soluble ZnO QDs were prepared using polyvinylpyrrolidone (PVP). By adjusting the amount of PVP, individually dispersed ZnO QDs and controlled QD aggregate sizes were achieved as illustrated by dynamic light scattering.

6. 2.   Experimental

6. 2. 1. Synthesize of ZnO QDs in Methanol

Colloidal ZnO QDs were prepared by hydrolyzing zinc acetate dihydrate in the basic methanol solution. Sixteen mmol of KOH (99.99%, Sigma-Aldrich) was first dissolved in 150 mL methanol at 60 °C with refluxing and stirring for 30 minutes to get a homogeneous solution. Subsequently, another 50 mL methanol solution containing 0.16 M zinc acetate dihydrate ($Zn(Ac)_2 \cdot 2H_2O$, 99%, Fluka) was added directly into the basic methanol solution. The concentrations of $[Zn^{2+}]$ and $[K^+]$ were 0.04 and 0.08 M, respectively, with a molar ratio of $[Zn^{2+}] / [K^+] = 0.5$. This starting sol was then allowed to react at 60 °C with refluxing and stirring for various times. After reaction, the size-focusing reaction was performed by concentrating the ZnO solutions *via* a rotary evaporator operated at 40 °C under vacuum.

6. 2. 2. Purification of ZnO QDs

To purify ZnO QDs, the precipitation-redispersion procedure introduced by Meulemkamp [6] in ethanol was first performed in methanol. Hexane was added to the ZnO methanol colloids. The volume ratio of hexane to the ZnO methanol colloids ranged from 1:1 to 5:1.

Isopropanol was further added as a modification of the above precipitation-redispersion procedure with a volume ratio of hexane: the ZnO methanol colloids: isopropanol = 5:1:1. White ZnO QDs precipitated immediately after addition of hexane and isopropanol into the ZnO methanol colloids. The mixture was kept at 0 °C overnight

until the ZnO nanoparticles were fully precipitated and settled down on the bottom. After centrifugation and removal of the supernatant, the ZnO QD precipitate was redispersed in methanol by hand-shaking. The above operations were repeated several times to wash the ZnO QDs in methanol.

The unpurified ZnO solutions were divided into two equal parts. One was concentrated 10 times at 40 °C *via* rotary evaporation under vacuum (concentrated ZnO colloids). The other was kept intact (non-concentrated ZnO colloids) for comparison purposes. Both of them were purified through the modified precipitation-redispersion procedure described above.

6. 2. 3. Stabilization of Purified ZnO QDs in Methanol

Three samples of ZnO QDs were prepared and purified using the modified precipitation-redispersion procedure three times, and then redispersed in 200 mL methanol, designated as Sample **a**, 175 mL methanol + 25 mL hexane (7:1), designated as Sample **b,** and 150 mL methanol + 50 mL hexane (3:1), designated as Sample **c**, respectively, by hand shaking. Appearance of the above three solutions was photographed to examine the formation of the ZnO aggregates as a function of time for up to 3 days.

6. 2. 4. Preparation of PVP-capped and Water-soluble ZnO QDs

PVP-capped ZnO QDs were first synthesize by hydrolyzing $Zn(AC)_2 \cdot H_2O$ in the basic methanol solution with the presence of PVP. The synthesis and purification

procedures were the same as already described above, except that 1.332 g of PVP (MW 8,000, Sigma-Aldrich) were also dissolved in methanol containing KOH before the reaction. After purification, the PVP-capped ZnO QDs were redispersed in methanol again and then the methanol and remaining solvents were fully removed *via* rotary evaporation under vacuum to avoid any contamination. After dying, 5 ml of distilled and de-ionized water was added and a gel-like sample (Sample A) was obtained

From the above-mentioned gel-like sample, 0.1g of ZnO QDs was dispersed into 100ml of water. After sonication, the dispersion was cloudy due to scattering from ZnO aggregates (Sample B). PVP (at 10, 20, and 30g) was added to the dry sample (0.1g ZnO QDs), and water was then added to each sample until a total volume of 100ml was reached. These three samples are designated as Samples C, D, and E, respectively. For comparison, an aqueous solution containing only PVP was also prepared.

6. 2. 5. Characterization

ZnO QD powder X-ray diffraction (XRD) patterns were performed by a Bruker D8 Advanced Powder X-ray Diffractometer with Cu-K$_\alpha$ incident radiation (λ=1.5418 Å). The patterns were recorded at 0.04° per step and a step time of 6 seconds. After twice washing, the ZnO precipitates obtained from the concentrated and non-concentrated ZnO colloids were dried at 110 °C for 2 hours and the powders were grounded by using a set of mortar and pestle for the powder XRD study.

The purified ZnO precipitates obtained from the concentrated and non-concentrated ZnO colloids were redispersed in methanol, diluted, and then a droplet of

each solution was placed onto a 400-mesh carbon coated copper grid. PVP-capped ZnO QDs were first diluted in water and then a droplet of the solution was place onto the same type of copper grid. The grids were then dried in a desiccator for one day before imaging. Transmission electron microscopy (TEM) of the above samples was carried out using a JEOL 2010 high-resolution transmission electron microscope operated at 200 kV.

The purity of the ZnO QDs upon washing was determined by measuring the $[K^+]$ in the ZnO colloids through Atomic Absorption Spectroscopy (AAS, Varian SpectrAA-300). After each washing cycle, the ZnO QDs were redispersed in 20 mL methanol. One hundred μL of sample was taken out from the redispersed ZnO methanol solution, and was then diluted for the measurement. The $[K^+]$ standard solutions for AAS measurements were prepared by diluting the KCl standard solution using methanol to the desired concentrations.

Thermal gravimetric analysis (TGA) of the purified ZnO QDs was carried out on a Q500 Thermogravimetric Analyzer from TA instruments. The precipitate obtained from the concentrated ZnO colloids after twice washing was dried at 110 °C in an oven for 2 hrs. The yield of ZnO nanoparticles was calculated by weighing the dry ZnO powder. Afterwards, a small amount of the above sample (about 15 mg) was heated from room temperature to 600 °C at a constant heating rate of 5 °C/min under an air flow of 90 mL/min.

UV-vis spectra of the colloidal ZnO QDs were recorded on a Hitachi (model U-4100) UV-vis-NIR spectrophotometer under both absorbance and transmittance modes.

Photoluminescence (PL) spectra were recorded using a PTI QM-4/2006 spectrofluorometer. A photon counter was used for detection.

Dynamic light scattering (DLS) of PVP-capped ZnO QDs in water was carried with a ZetaPALS (Brookhaven Instruments). Colloidal samples were diluted to achieve the highest signal with minimum noise. The acquired autocorrelation function was fit with numerical methods, and the structure factor and time-dependent intensity was used to quantify average hydrodynamic mobility, which are directly related to aggregate/ single particle size.

6. 3.   Results and Discussion

6. 3. 1. Colloidal Growth of Monodisperse ZnO QDs

Figure 6.1 shows the UV-vis spectra of the growth of ZnO QDs as a function of time. The reaction was performed at 60 °C for 2 hours (120 min). Subsequently, the ZnO solution was concentrated by solvent evaporation and the UV-vis spectra of the ZnO solution during concentrating is also illustrated in Figure 6.1. The absorption from ZnO QDs shows red-shifting due to the growth of the particle.
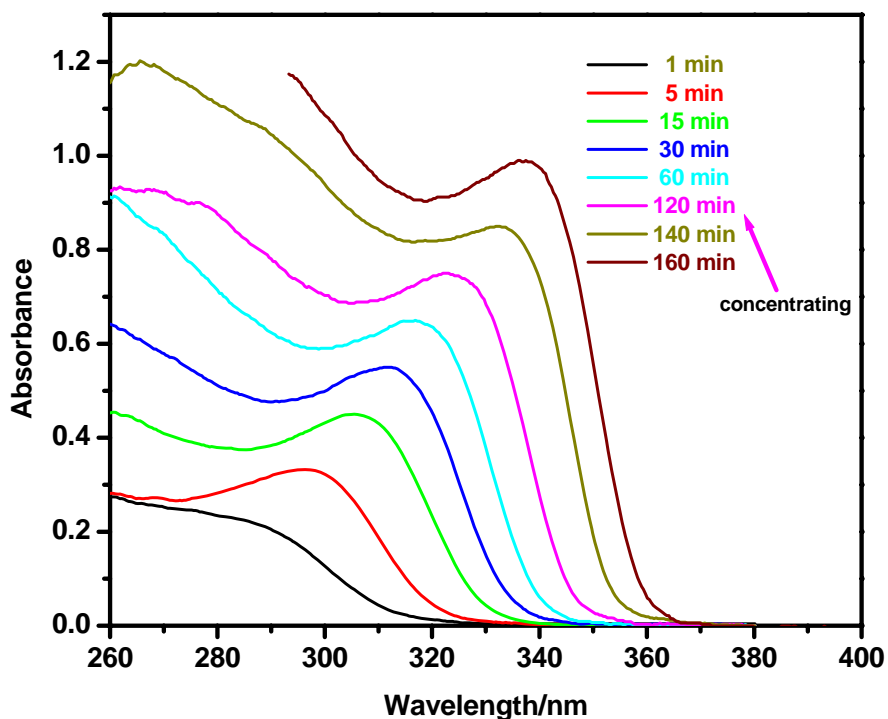
Figure 6.1. UV-vis spectra of the growth of colloidal ZnO QDs during the reaction and concentrating process.

Meulenkamp developed a semi-empirical equation to determine colloidal ZnO nanoparticles ranging from 1 to 7 nm using UV-vis absorption spectra *[169]*:

$$1240/\lambda_{1/2} = a + b/D^2 - c/D \tag{1}$$

Where $\lambda_{1/2}$ is the wavelength at which the absorption is 50% of that at the absorption peak (or shoulder); a, b, and, c are parameters where a = 3.301, b = 294.0, and c = -1.09. A simple and practical method to determine the particle size distribution is to use the full width at half maximum (FWHM) of the absorption peak. A small FWHW

number indicates a narrow size distribution. The particle size and FWHW of colloidal ZnO QDs during growth determined through the above methods are shown in Figure 6.2. The growth of colloidal ZnO QDs is fast at the beginning of the reaction due to the high reagent concentration, but is significantly slowed down by the consumption of the reagents. The particle size after the 2-hour reaction at 60 °C is around 3 nm in diameter. Further concentrating by 10 times causes a rapid growth to around 5 nm after around 40 min. FWHM drops rapidly at the beginning of the reaction indicating a narrow size distribution when the particle size is small. This is because of the size focusing mechanism at a high reagent concentration. However, as the particle grows, the reagents are depleted, thus the size distribution becomes wider as illustrated by the increase of FWHM. Further concentrating the solution leads to a drop of FWHM because the reagent concentration becomes higher during the concentrating process, thus causes the size re-focusing effect. The above analysis suggests that concentrating the ZnO solutions results in a rapid particle growth and a narrow size distribution.

Figure 6.3A shows the TEM image of the colloidal ZnO QDs prepared for the present study. ZnO QDs are highly crystalline (the inset of Figure 6.3A) and have a nearly uniform particle size of 5 nm, which agrees with the analysis from the UV-vis spectra. The statistical analysis in Figure 6.3B based on 250 QDs from the high-resolution TEM image yields an average particle size of 5.0 ± 0.3 nm ($\sigma = 6\%$).
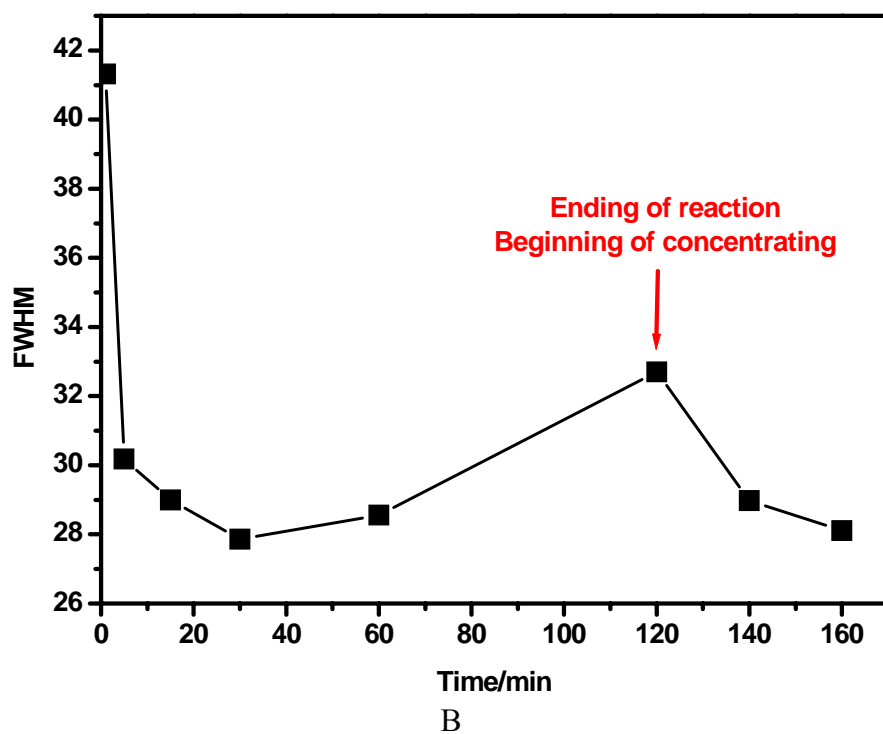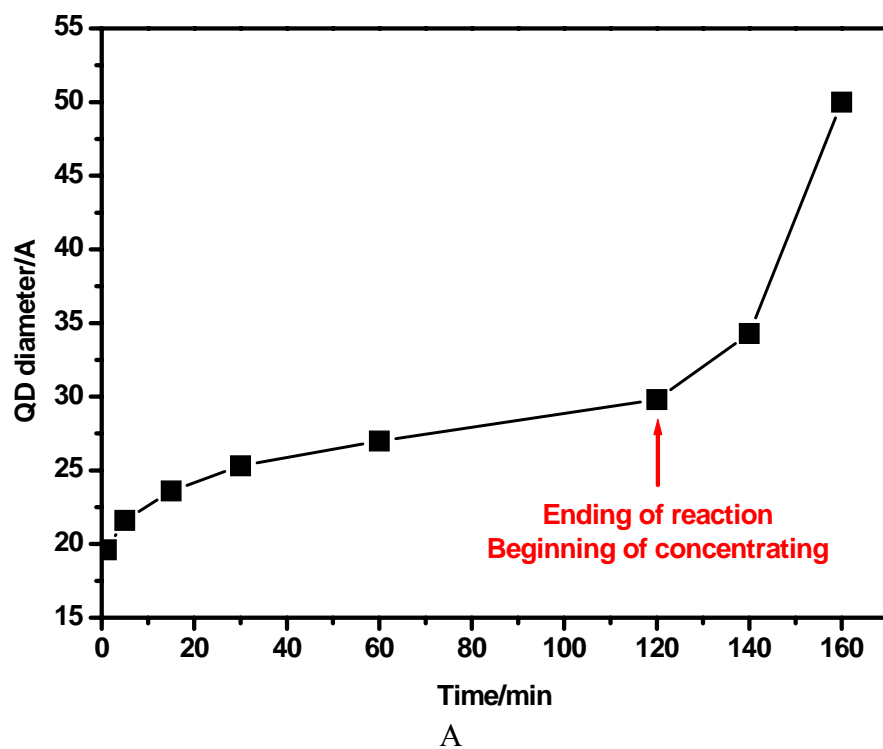
Figure 6.2. (A) particle size and (B) FWHM as size distribution of colloidal ZnO QDs during the colloidal growth.

A

B
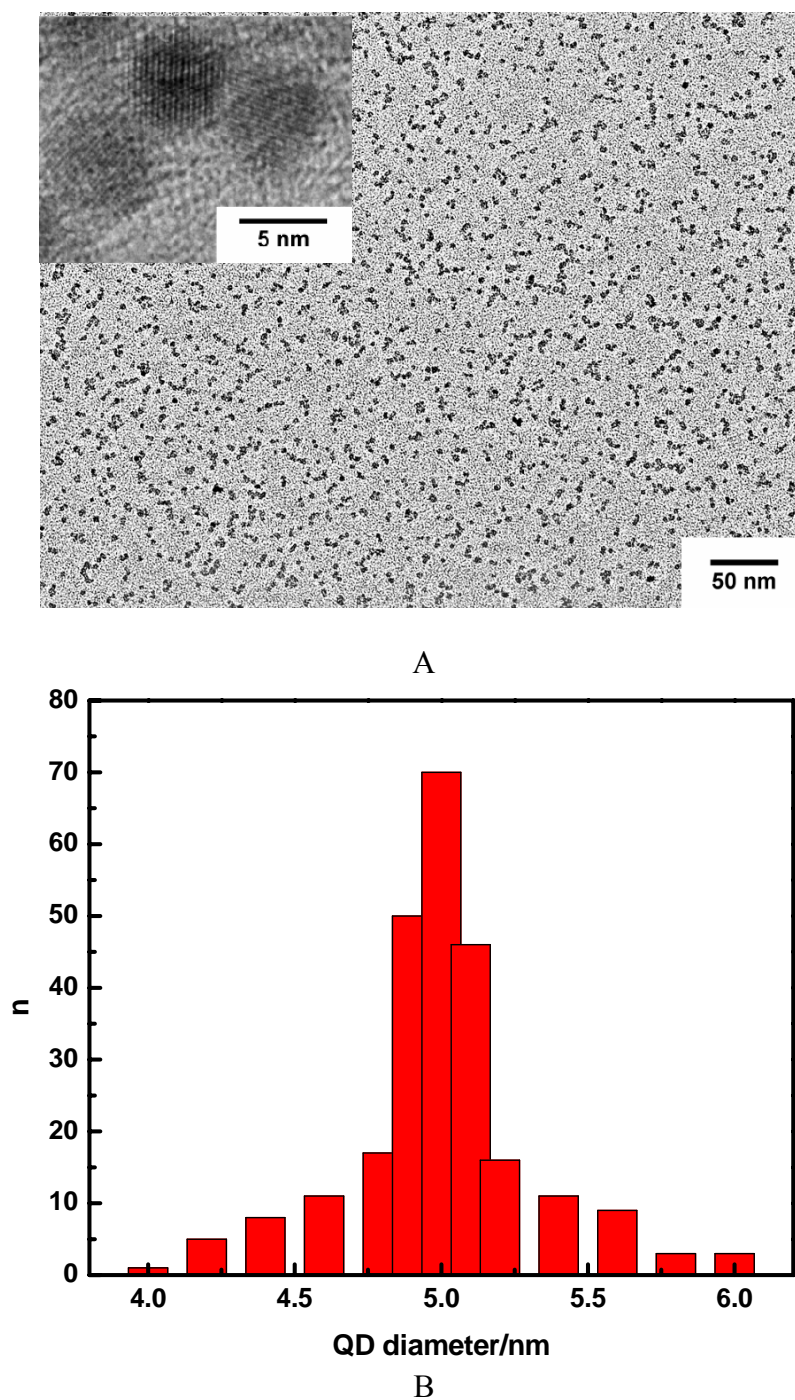
Figure 6.3. (A) HR-TEM image of colloidal ZnO QDs used in this study. Inset is a high-magnification image of ZnO QDs. (B) Size distribution of colloidal ZnO QDs. The particle size is 5.0 ± 0.3 nm.

6. 3. 2. Removal of Unwanted Ions from ZnO QDs

The removal of unwanted ions from ZnO QDs in ethanol was first performed by Meulenkamp *[169]* by using organic non-solvents such as hexane or heptane. It was reported that the required volume ratio of hexane (or heptane) to the ZnO ethanol colloids was between 1:1 and 2:1. The ZnO precipitates obtained were then redispersed in ethanol. By repeating this procedure, ZnO QDs could be purified after two washing steps.

However, in the case of colloidal ZnO QDs in methanol, two clear liquid phases coexist and no ZnO precipitate is observed after adding hexane into ZnO methanol colloids with the volume ratio of hexane to the ZnO methanol colloids ranging from 1:1 to 5:1. According to the density differences between hexane and methanol ($d_{methanol}$=0.792 g/mL and d_{hexane}=0.684 g/mL at 20 °C), the top phase is hexane-rich and the bottom phase is methanol-rich. These two liquid phases are quite stable either at room temperature or at 0 °C. When the volume ratio of hexane to the ZnO methanol colloids is reduced to 1:2, only one clear homogeneous phase is formed, indicating a complete mixing of the two solvents, but still no ZnO precipitate is formed either at room temperature or at 0 °C. Based on the above experiments, it is evident that hexane cannot be used for precipitating and purifying ZnO QDs in methanol. The similar phenomenon also occurs with heptane. This is because unlike ethanol, which is totally miscible with hexane or heptane at room temperature, methanol is only partially miscible with heptane or hexane at 25 °C due to its relatively short carbon chains.

To achieve the similar effect in purifying ZnO QDs in methanol, isopropanol is added into the mixture of hexane and the ZnO methanol colloids. The two pre-existing hexane-rich and methanol-rich liquid phases become one homogeneous phase and white ZnO precipitate is formed immediately. This precipitate can be easily redispersed in methanol. Therefore, by introducing isopropanol into hexane and the ZnO methanol colloids, ZnO QDs prepared in methanol can be purified by the same precipitation-redispersion procedure as in the ethanol case.

To estimate the ZnO purity, AAS was used to monitor the concentration of the main cation impurity, K^+. Figure 6.4 shows the concentration of K^+ in the redispersed ZnO methanol solution after washing. The main impurity, KAc, was greatly reduced after a few cycles of washing. Therefore, it confirms that the introduction of isopropanol into the hexane/methanol mixture can effectively purify ZnO nanoparticles in methanol. To be noted, in the AAS results, the concentration of K^+ decreases 95% after the first purification cycle. However, the reduction in K^+ becomes much slower after that. The second, third, and fourth cycles of washing remove only 83%, 48%, and 48% of K^+, respectively (see the inset in Figure 6.4). This is because after the first two cycles of purification, most of the free acetate anions in methanol have been removed. The remaining acetate anions are those attached on the ZnO QDs. After the ZnO QDs are redispersed twice, some of the acetates may still detach from the nanoparticles due to the dynamic equilibrium between ZnO and acetate. Both the third and fourth cycle of purification remove ca. 48% K^+, indicating that it has reached the purification efficiency

limit, which is determined by the dynamic equilibrium of the interaction between K^+, Ac^- and the ZnO QDs.

Washing cycle	Washing efficiency
1	95%
2	83%
3	48%
4	48%
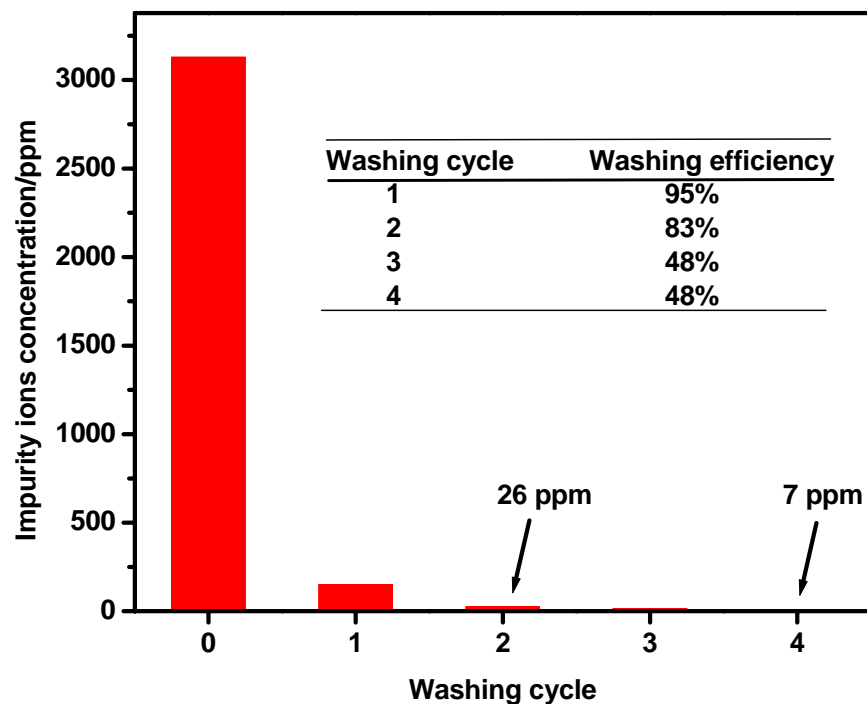
Figure 6.4. K^+ concentration of the redispersed ZnO methanol solution vs. washing cycle. The inset table shows the efficiency of each washing cycle.

The above modified purification process of extracting ZnO QDs from methanol is similar to the use of hexane to precipitate ZnO from ethanol. The metal ion impurities, i.e., Li^+ in Meulenkamp's method and K^+ in the current approach, are extracted together by a large volume of organic non-solvent, allowing the ZnO QDs to precipitate. In the

case of methanol, hexane cannot extract methanol and impurities due to its low solubility with methanol. Incorporation of isopropanol here helps to compatibilize between methanol and hexane, thus allowing the ZnO QDs to precipitate.

6. 3. 3. Removal of By-product from ZnO QDs

In Meulenkamp's report *[169]*, some kind of basic zinc acetate in the ZnO precipitate was observed when the ZnO QDs were precipitated from an early ZnO sol by using heptane or hexane. According to the result obtained by Tokumoto and co-workers *[171]*, this basic zinc acetate has a layered structure called zinc hydroxyl double salt (Zn-HDS) or zinc layered double hydroxide (Zn-LDH), $Zn_5(OH)_8(Ac)_2 \cdot 2H_2O$. The above findings are of particular importance in producing purified ZnO QDs through the sol-gel method and help to determine the optimal reaction conditions under which the best conversion of ZnO QDs could be attained.

Figures 6.5 and 6.6 show the XRD patterns and TEM images of the ZnO QDs obtained from the non-concentrated and concentrated ZnO colloids through the modified precipitation-redispersion procedure. In the XRD pattern of the precipitate obtained from the non-concentrated ZnO colloids (Figure 6.5A), two characteristic peaks at 6.7° and 33.3° stand for (001) and (100) planes of Zn-LDH, respectively. Wurtzite peaks around 31.7°, 34.6° and 36.9° from ZnO QDs are also present. However, they are overlapped with the peak at around 33.3° of Zn-LDH due to the extremely small particle size, which makes it difficult to calculate the particle size of ZnO by using the Debye-Scherrer formula. The TEM image of the precipitate containing ZnO QDs and Zn-LDH obtained

from the non-concentrated ZnO colloids is shown in Figure 6.6A. An average diameter

of approximately 3 nm of spherical nanocystalline ZnO particles (inset in Figure 6.6A)

and the sheets of Zn-LDH (see arrows) can also be observed.
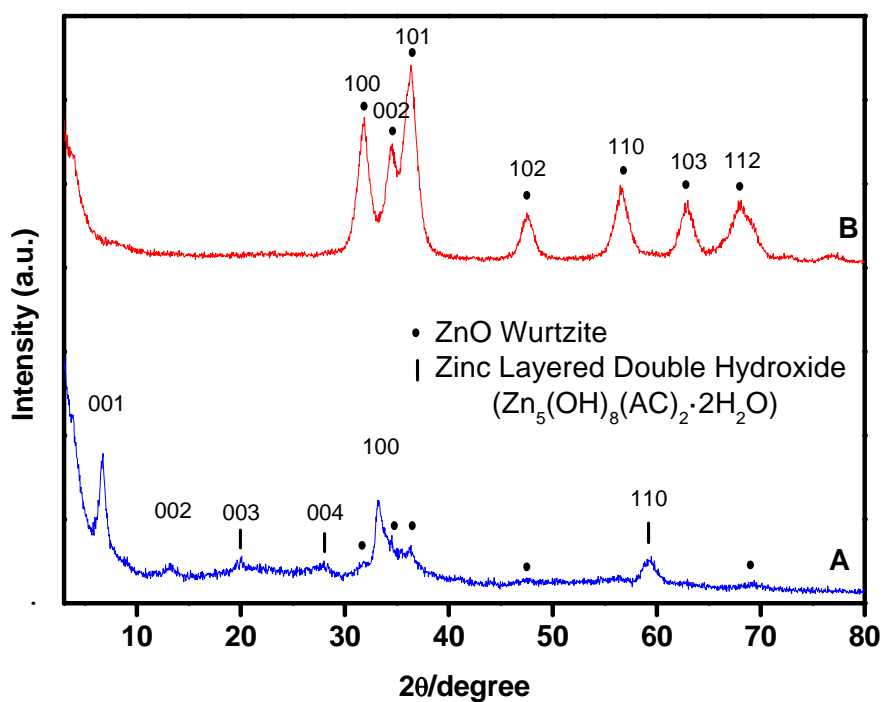
Figure 6.5. Comparison of (A) XRD powder pattern of the precipitate obtained from the non-concentrated ZnO colloids with (B) that obtained from the concentrated ZnO colloids.
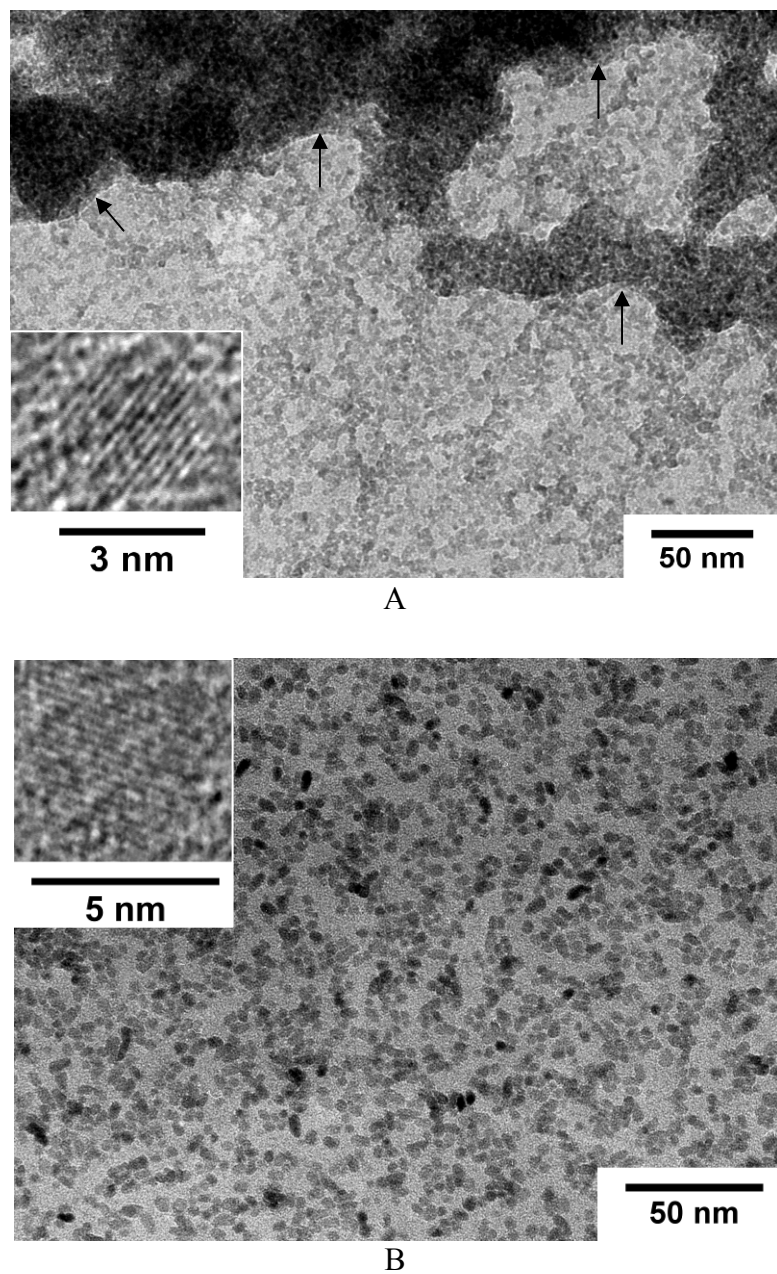
Figure 6.6. TEM images of (A) the precipitate obtained from the non-concentrated ZnO colloids and (A) that from the concentrated ZnO colloids. The mixture of ZnO QDs and Zn-LDH can be observed in A. The inset in A is the high-resolution image of a crystalline ZnO QD with the particle size of about 3 nm. The arrows in (A) point to the edges of the Zn-LDH sheets. The inset in (B) is the high-resolution image of a crystalline ZnO QD with the particle size of about 5 nm.

Zn-LDH is not detectable from XRD (Figure 6.5B) and TEM (Figure 6.6B) of the ZnO precipitate obtained from the concentrated ZnO colloids through the modified precipitation-redispersion procedure. The precipitate obtained from the concentrated colloids contains only ZnO QDs with a particle size of around 5 nm. High-resolution TEM (inset in Figure 6.6B) shows that the ZnO QDs are highly crystalline. The corresponding XRD powder pattern, which exhibits the Wurtzite structure, indicates that the average particle size based on the Debye-Scherrer formula $t = 0.89\lambda /(\beta \cos\theta)$ (t stands for the average diameter of the particles; λ, the X-ray wavelength, 1.5418 Å; β, full width at half maximum, FWHM, of the diffraction peak; and θ, the diffraction angle) is also around 5 nm. Consequently, concentrating the ZnO methanol colloids by a factor of 10 *via* solvent evaporation at 40 °C causes the removal of Zn-LDH from the ZnO precipitate and a particle growth from 3 nm to 5 nm. The calculated yield of ZnO QDs with respect to the initial Zn^{2+} concentration is around 90 %.

The growth of ZnO QDs due to solvent evaporation observed from XRD and TEM is consistent with the findings from the UV-vis spectra, and the removal of Zn-LDH can be explained using the reactions proposed by Spanhel *[166]* recently:

$$Zn_{10}O_4(Ac)_{12} + 16H_2O \rightarrow 2Zn_5(OH)_8(Ac)_2(H_2O)_2 + 8HAc \qquad (1)$$

$$Zn_{10}O_4(Ac)_{12} + 8H_2O + 8OH^- \rightarrow 2Zn_5(OH)_8(Ac)_2(H_2O)_2 + 8Ac^- \qquad (2)$$
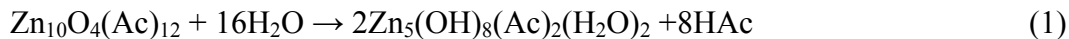
Where $Zn_{10}O_4(Ac)_{12}$ is the secondary precursor leading to the formation of ZnO. During solvent evaporation, the concentrations of HAc and Ac^- in the ZnO colloids have increased, while $Zn_{10}O_4(Ac)_{12}$ is reduced to form ZnO. Therefore, the reactions (1) and (2) take place conversely, leading to the removal of Zn-LDH.

6. 3. 4. Stabilization of Colloidal ZnO QDs in Methanol

Achieving uniform redispersion of purified ZnO QDs into a common solvent is a key step for practical applications of colloidal ZnO QDs. For example, mixing clear ZnO colloids with a compatible polymer solution can lead to the formation of homogeneously dispersed polymer/ZnO nanocomposites. However, in our study, the purified ZnO nanoparticles are unstable in methanol. At room temperature, the purified ZnO QDs become aggregated within several minutes. Interestingly, although hexane alone cannot cause the precipitation of ZnO QDs in methanol, it can help to stabilize and disperse the purified ZnO QDs in methanol.

The stability of the purified ZnO QDs redispersed in methanol and in methanol/hexane solutions is investigated (Figure 6.7). Sample **a** contains ZnO QDs redispersed in methanol alone, while sample **b** and **c** contain both hexane and methanol at different volume ratios (1:7 for sample **b** and 1:3 for sample **c**). Transparent solutions can be obtained immediately after the ZnO QDs are added in either pure methanol or methanol/hexane mixtures by hand shaking, indicating the formation of fully redispersed ZnO solutions at room temperature. However, Sample **a** turns bluish within 30 minutes which means that the ZnO QDs have begun to aggregate.

In the case of the redispersion of ZnO QDs in the mixture of methanol/hexane solutions, the solution retains its transparency for a much longer time. It is also shown that the higher concentration of hexane in the solution, the more stable the solution becomes. Even though the ZnO QDs would begin to agglomerate in the methanol/hexane solution mixture after a couple of hours (i.e., Sample **b**), the presence

of hexane in the solution can still prevent the aggregates from settling down. Sample **c**, which has the highest concentration of hexane, can maintain its transparency for at least one day at room temperature. Even after three days, it only turns to be slightly bluish. The volume ratio of hexane to methanol cannot be higher than 3:4 due to the limitation of the solubility of hexane in methanol. The above results confirm that hexane can stabilize the purified ZnO QDs in methanol.
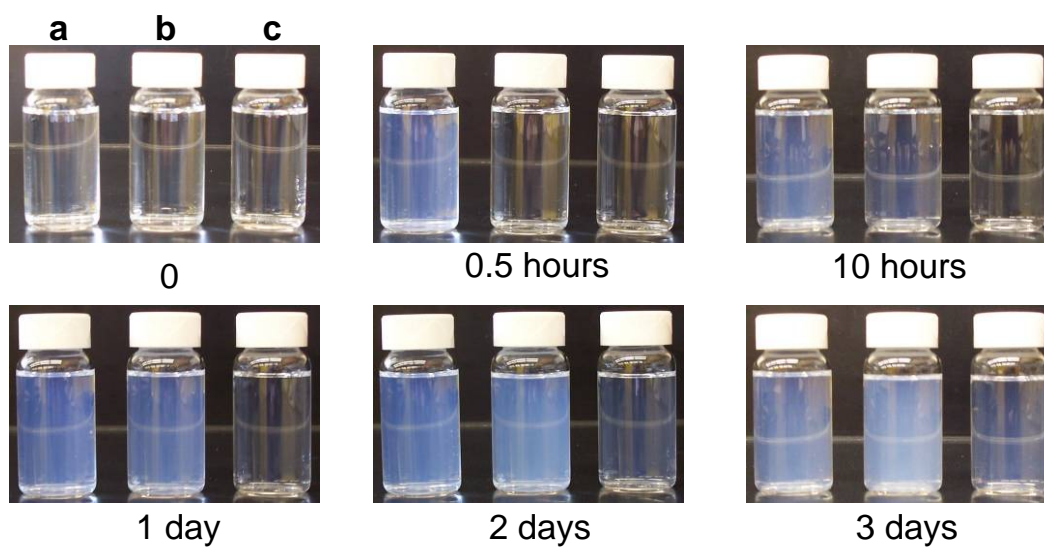
Figure 6.7. Visual observation of the aggregate formation from the purified ZnO QD solutions as time evolves: (a) methanol, (b) methanol: hexane = 7:1, and (c) methanol: hexane = 3:1.

Generally, colloidal ZnO QDs prepared from $Zn(Ac)_2$ have surface defects such as oxygen vacancies *[181, 182]*, which are passivated by acetate ions. The formation of bonding between surface Zn atoms and O atoms in carboxylic groups of acetate ions in colloidal ZnO QDs has also been found *[183]*. Sakohara and co-workers *[174, 176]*

suggest that the acetate groups on the particle surface affect the stability of ZnO colloids. The more acetate groups on the surface, the higher the stability of ZnO colloids. They reported that the colloids prepared at a high ratio of $Zn(Ac)_2$: LiOH=0.1M: 0.025M can maintain the transparency of the colloids in a refrigerator for more than one month. However, their colloids still contain LiAc. In our study, the concentrated ZnO colloids can maintain clarity at 0 °C for over two months. Even for the concentrated ZnO colloids, it can still maintain the colloid clarity at 0 °C after three weeks.

Contrarily, in the purified ZnO colloids, the reduced amount of acetate ions bound on the ZnO surface alone can no longer prevent the colloidal ZnO QDs from aggregating. Figure 6.8 shows the TGA results of the colloidal ZnO QDs. A total weight loss of 6 % was observed for the purified colloidal ZnO QDs dried at 110°C for 2 hours due to the effective removal of KAc by the modified precipitation-redispersion procedure. Sakohara and coworkers *[174]* have shown that heating colloidal ZnO QDs below 150°C does not lead to the decomposition of acetate. A small amount of weight loss (0.4 wt.%) observed at temperatures below 150 °C is considered to be dissociation of the weakly bound solvent molecules, such as methanol and water remaining in the sample. Therefore, the amount of acetate, which is likely to be bound to the surface defects of the colloidal ZnO QDs as ligand, is estimated to be 5.6 wt % (6 – 0.4 wt.%) and is hard to remove by washing. From the above analysis, it is evident that the acetate in the ZnO colloids has been greatly reduced by washing. This finding agrees well with our AAS results. The minimal amount of acetate ligand present is unable to maintain the stabilization of the purified ZnO QDs in methanol.
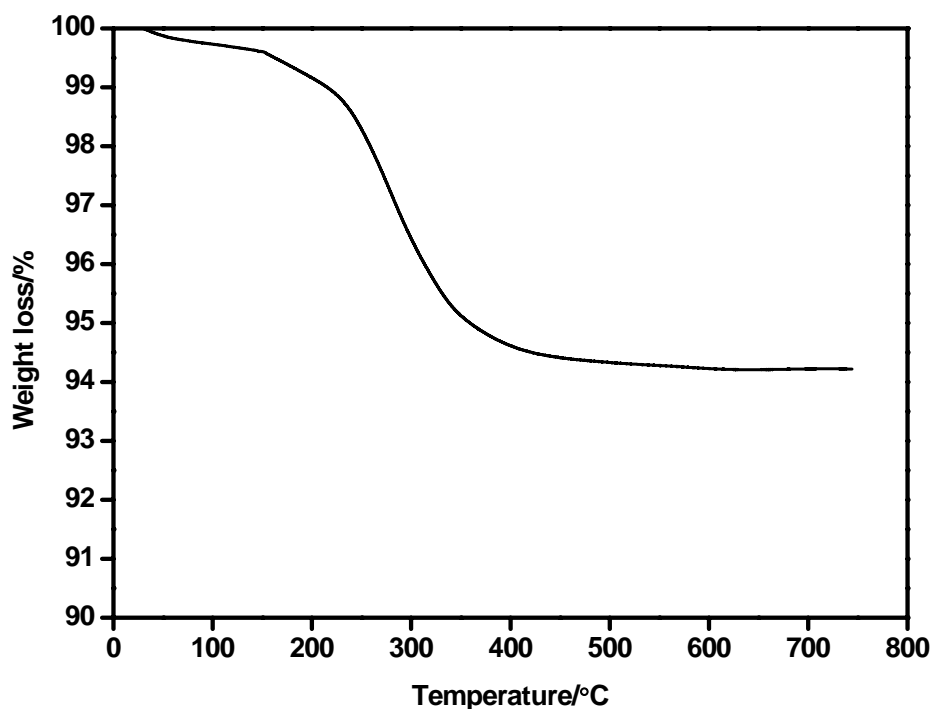
Figure 6.8. TGA curve of purified colloidal ZnO QDs.

In the case of the hexane-stabilized ZnO colloids in methanol, one reason why hexane can stabilize the purified ZnO QDs in methanol could be that a small amount of organic non-solvent, i.e., hexane, dissolved in methanol helps to reduce the polarity of the solvent around the acetate-containing ZnO QD surfaces, thus isolating the ZnO QDs from each other and preventing them from aggregation by enhancing the electrostatic repulsion between charged QDs.

6. 3. 5. Water-soluble ZnO QDs

PVP is an amphiphilic (having both hydrophobic and hydrophilic components) polymer and has been commonly used to modify QDs for the purposes of surface passivation and stabilization in non-aqueous systems. It is also known to be non-toxic to humans and has been used as a kind of food additive. Figure 6.9 shows the TEM image and XRD pattern of PVP-capped ZnO QDs. The TEM image reveals a uniform size distribution that is estimated to be around 4 to 5nm. The corresponding XRD pattern exhibits the Wurtzite structure of ZnO indicating a highly crystalline structure. The calculation based on the Debye-Scherrer formula yields an average particle size of around 4.2 nm, which is consistent with the TEM observation.

10 nm

A
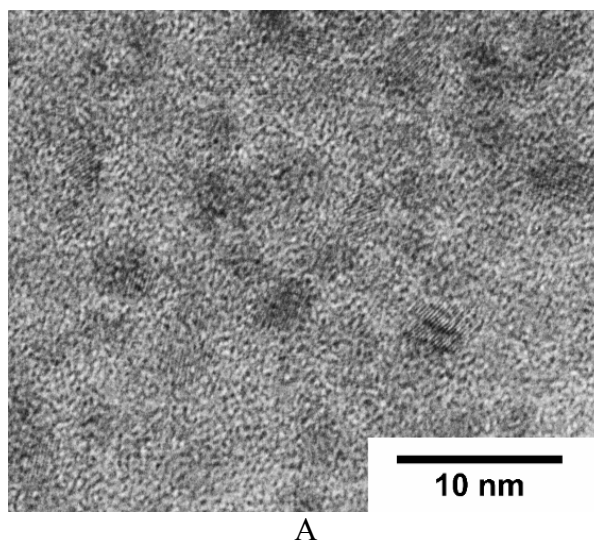
Figure 6.9. (A) TEM image and (B) XRD pattern of PVP-capped ZnO QDs.
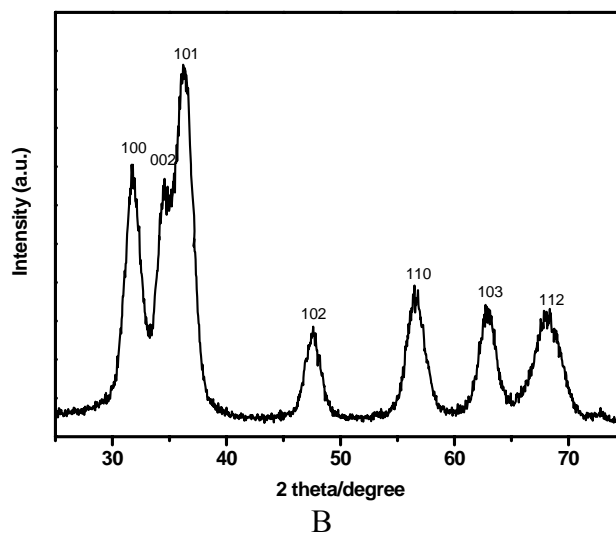
Figure 6.9. Continued.

Figure 6.10 shows the photographic images of the purified gel-like ZnO QDs (Sample A) and ZnO QDs dispersed in water using different amounts of PVP (Samples B-E). A gradual decrease in light scattering is seen as the amount of added PVP increases, which is consistent with a reduction in aggregate size. In the case of Sample B, no additional PVP is added following the initial synthesis, and the large ZnO QD aggregates (100s of microns in size) scatter the visible light to the degree that the solution is nearly opaque. When the PVP:ZnO=100:1 as shown in Sample C, the solution becomes translucent because of the reduction of ZnO QD aggregate size, but the ZnO QD aggregates are still at the scale of hundreds of nanometers to several microns. As the amount of PVP increases to yield PVP:ZnO=200:1 (Sample D), the solution becomes clear, indicating that the ZnO QD aggregates have been decreased to below 100nm in size, where visible light is no longer scattered. As for Sample E, where even

more PVP is added, it shows similar transparency to Sample D, but the dispersion is slightly yellow. Dynamic light scattering in Figure 6.11 has been used to estimate the actual ZnO QD aggregate sizes in Samples D and E. The average size of ZnO QD aggregates in Sample D is estimated to be around 10nm with a fairly wide tail extending to 14nm, indicating that the dispersion contains a low percentage of individually dispersed ZnO QDs. In the case of Sample E, the 4-5nm average particle size points to single ZnO QDs dispersed in water. Therefore, by adjusting the amount of PVP used, ZnO QDs can be tuned from micron-sized aggregates down to single QDs in water. Figure 6.12 illustrates this concept schematically.

Sample A   Sample B   Sample C   Sample D   Sample E
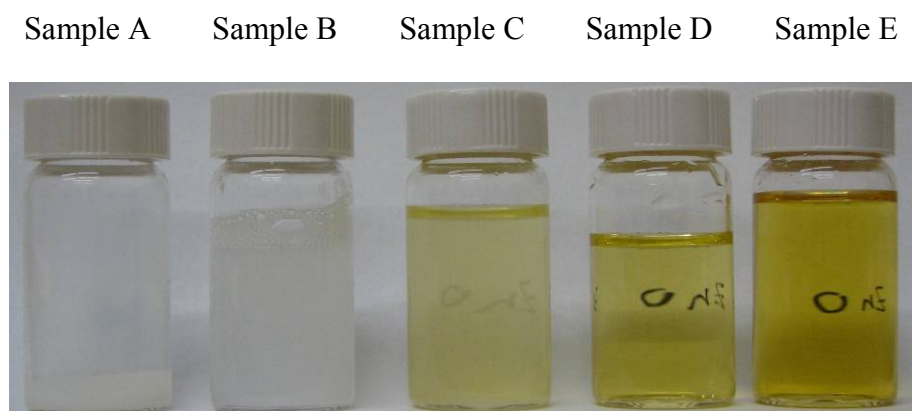
Figure 6.10. Photographic images of Sample A-E. The same marking is made on the opposite side of each jar so that the level of transparency can be qualitatively judged.
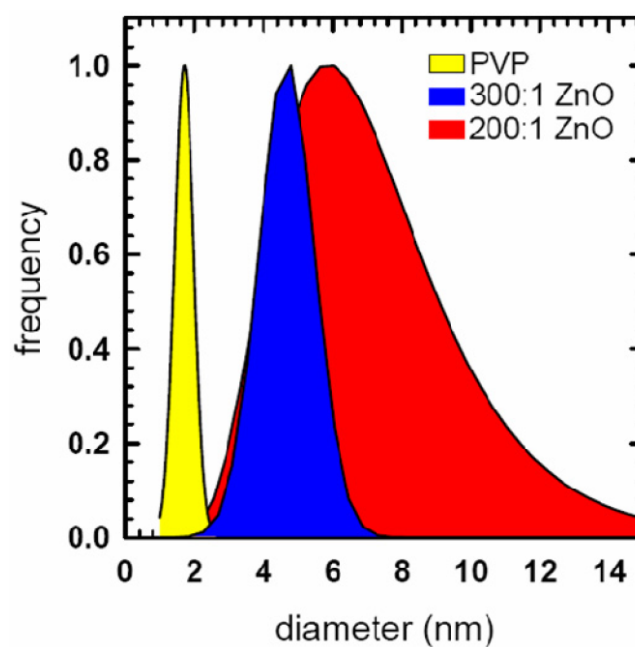
Figure 6.11. DLS of Samples D (PVP: ZnO = 200: 1), E (PVP: ZnO = 300: 1), and PVP dissolved in water.
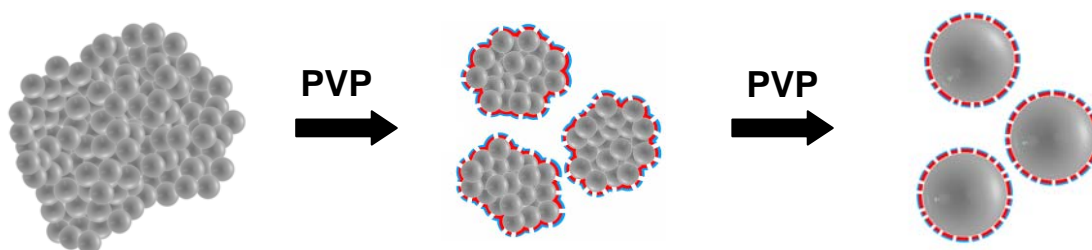
Figure 6.12. Schematic showing control of ZnO QD aggregate sizes in water through the addition of PVP.

6. 4.   Conclusions

Monodisperse colloidal ZnO QDs with an average particle size of 5.0 nm ($\sigma =$ 6%) were successfully synthesized in methanol through a size-focusing reaction by concentrating the reaction solutions. The major by-product of this reaction was also removed. Unwanted ions such as K^+ and Ac^- have been effectively removed through a modified precipitation-redispersion approach. The purified ZnO QDs can be further stabilized in methanol by adding a small amount of hexane. High-quality monodisperse ZnO QDs are of particular significance for many practical applications such as functional ZnO coatings, polymer/ZnO nanocomposites, and device fabrication. The current colloidal QDs can also serve as a model to investigate the structure-property relationship in various systems such as polymer/QD nanocomposites, which will be discussed in the next chapter.

PVP-capped ZnO QDs were prepared and purified using the same colloidal procedures with the existence of a small amount of PVP. Subsequently, the purified PVP-capped ZnO QDs were readily dispersed in water, and the degree of stabilization was controlled *via* the post-addition of PVP at different concentrations. Average ZnO QD aggregate sizes can be controlled from microns down to individual QDs in water, depending on the amount of PVP added. These tunable ZnO QD aggregates can be used as effective antimicrobial agents for biomedical applications and as a model to study the QD cytotoxicity effects. Furthermore, this approach is also applicable to any other colloidal system with inorganic nanoparticles for controlling the degrees of dispersion and aggregate sizes.

CHAPTER VII

DISPERSION OF LIGAND-FREE ZNO QUANTUM DOT IN POLYMERS[*]

7. 1.   Introduction

Semiconductor nanocrystals, also known as quantum dots (QDs), possess outstanding optical, electrical and optoelectronic properties that are of particular interest in many electronic, photonic, and biological applications *[4, 31, 50]*. These exceptionally useful characteristics arise from both quantum size effects and their enormous surface-to-volume ratio *[28]*. By varying QD diameter, the degree of quantum confinement is tuned, which defines their optical and electrical response; the large fraction of non-coordinated surface atoms dictates many of their thermodynamic properties. By incorporating QDs into polymers, a new type of inorganic/organic hybrids – polymer/QD nanocomposite is generated, which possess exceptional properties that both have. However, these promising characteristics are linked intimately with the degree to which the QDs are dispersed in the matrices.

As individual quantum dots increase in size, optical absorption and emission undergo a red-shift, which is generally observed in highly dispersed colloids *[8, 168]*. Likewise, in systems where colloidal aggregates are formed, QDs exhibit red-shifting as aggregate size increases *[7]*. It has been demonstrated that electronic energy transfer can

occur between neighboring QDs through long-range coupling at interparticle separations of up to 10 nm *[33, 34]*, and QDs begin to display bulk material properties when they come into direct contact and reach a critical aggregate size *[184]*, Moreover, similar phenomena have been observed in ligand-free QD powder *[183]* and highly aggregated ligand-free QDs in polymer matrices *[100]*. Therefore, in theory, tuning the degree of QD dispersion in polymers opens up a promising way to control properties of polymer nanocomposites containing QDs of one type.

Surface area-to-volume ratio drops abruptly as the degree of QD aggregation increases in polymer matrices, and this reduces their usefulness in many ways. For example, QD aggregation in polymers may affect adversely the efficiency of photovoltaic devices, such as solar cells, by reducing the interfacial area and thus decreasing power-conversion efficiency *[21, 22]*. Physical properties of polymer matrices, e.g. thermal stability, modulus, toughness, etc., may be significantly compromised by a reduction in the interfacial surface area resulting from QD aggregation *[89]*. Additionally, highly aggregated particulate matter within transparent matrices such as polymers inevitably causes substantial light scattering that restricts the use of transparent polymer nanocomposites to a limited set of optical applications *[91, 92]*.

A detailed literature review on the dispersion of QDs in polymers can be found in **Chapter II**. It should be noted here that, solution mixing is a straightforward approach to achieve better dispersion of inorganic nanofillers in polymers but it requires the particles to be stable in the dispersing solvent that is also miscible with the polymer

matrix *[51]*. Colloidal QDs are generally stabilized through surface modification using covalently bound ligands or adsorbed macromolecules *[8, 44, 84, 185]*. However, aggregation has still been frequently observed after solvent evaporation even though modified QDs are stable in such solvent *[88]*.

In this study, a completely new approach to disperse ZnO QDs into polymers down to individual QD level without using organic capping agents or surfactants (ligand-free) is introduced. Monodisperse ZnO QDs with high purity prepared in the last chapter were utilized. It has been found that the colloidal ligand-free ZnO QDs can be easily stabilized in polymers, such as thermosetting epoxy and thermoplastic poly(methyl methacrylate) (PMMA), *via* addition of exfoliated nanoplatelets (e.g. alpha-zirconium phosphate, ZrP) and that the dispersion state of ZnO QDs without organic capping agents can be tuned by controlling the amount of exfoliated nanoplatelets incorporated. Here, high-resolution transmission electron microscopy (TEM) reveals that the dispersion state of the QDs in the polymer matrix can be tuned from micron-sized aggregates down to individual QDs by adjusting nanoplatelet concentration. The polymer hybrid nanocomposites that contain well-dispersed QDs also exhibit nearly identical optical transmittance spectra to that of the neat epoxy samples. Additionally it has been found that, although QDs readily form aggregates when added to acetone and methanol, the presence of nanoplatelets at a sufficient volume fraction leads to QDs dispersion down to nanoscale clusters and likely individual dots in the organic solvent.

The mechanisms responsible for the nanoplatelet-assisted QD dispersion were investigated. Based our experimental results and dynamic and kinetic analyses, one

important mechanism involves nanoplatelets thermodynamically altering local matrix interactions with the QDs. Extensions of the approach described in this report may be ideal for a variety of applications, including but not limited to, photovoltaic devices, thermal and optical stabilizers, and anti-microbial coatings, wherein QD functionalization negatively impacts material performance.

7. 2.   Experimental

7. 2. 1. Preparation and Purification of Monodisperse ZnO QDs

Colloidal ZnO QDs were synthesized and purified according the method described in **Chapter VI**. The purified ZnO QDs with an average particle size of 5.0 nm were fully redispersed in methanol with a concentration of 0.4 M to be incorporated into epoxy.

7. 2. 2. Synthesis and Exfoliation of ZrP Nanoplatelets

ZrP nanoplatelets with a diameter of ~100 nm were used in this study (Figure 7.1A). They were synthesized and exfoliated in water according to methods detailed in **Chapter III**. The single exfoliated ZrP nanoplatelet shown in the TEM image in Figure 7.1B is representative of the typical shape the nanoplatelets used. By ultracentrifugation and redispersion, exfoliated ZrP nanoplatelets in aqueous solution were transferred into acetone to be mixed with epoxy resin and ZnO QDs *[141]*.
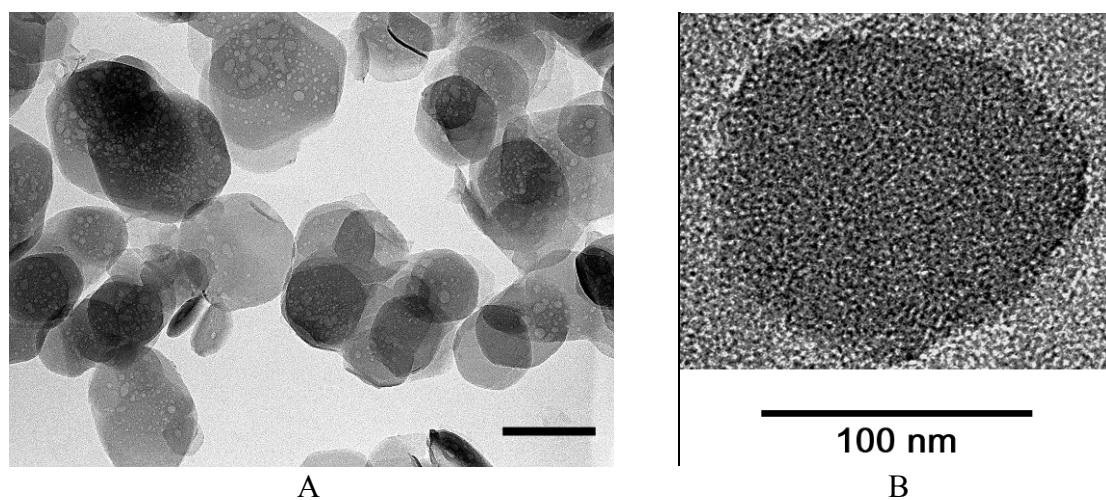
Figure 7.1. TEM image of (A) pristine ZrP nanoplatelets used in this study and (B) a exfoliated single-layer of ZrP nanoplatelet. The scale bar in (A) is 100 nm.

7. 2. 3. Incorporation of ZnO QDs and ZrP Nanoplatelets in Epoxy

To create the epoxy nanocomposites for studying the dispersion mechanism, diglycidyl ether of bisphenol-A (DGEBA) epoxy resin (DER^{TM} 332 epoxy resin, Dow Chemical Company) with an average epoxide equivalent weight of 174 was first dissolved in acetone containing exfoliated and dispersed ZrP nanoplatelets, and then a dispersion of purified ZnO QDs in methanol was added to the mixture. The solvents were then volatilized in a roto-vapor under vacuum at 80 °C for 1 hour. Following solvent evaporation, the epoxy mixture was clear and appeared to be free of QD aggregates; epoxy mixtures prepared without nanoplatelets were cloudy following this step. After being degassed at 100 °C for 1 hour, a stoichiometric amount of the curing agent 4,4'-diamino-diphenylsulfone (DDS, Sigma-Aldrich) was added to the epoxy. This

mixture was heated rapidly to 130 °C and held at that temperature until the DDS was fully dissolved. The mixed epoxy was then poured into a preheated glass mold coated with mold-release agent (Frekote44-NC, Henkel), cured in an oven at 180 °C for 2 hrs, post-cured at 220 °C for another 2 hrs, and then slowly cooled to room temperature. Samples containing both ZnO QDs and ZrP nanoplatelets are hereafter designated as either "epoxy/ZnO/ZrP" or "epoxy hybrid nanocomposites."

Epoxy hybrid nanocomposites with different volume fractions (ϕ_{ZnO} and ϕ_{ZrP}) of ZnO QDs and ZrP nanoplatelets were prepared for this study. For comparison purposes, neat epoxy samples without fillers and epoxy composites containing only ZnO QDs, designated as epoxy/ZnO, were also prepared by the same curing protocol described above.

7. 2. 4. Characterization

UV-vis spectra of neat epoxy and nanocomposites were recorded on an Ocean Optics USB2000-DT-Mini Spectrometer. The samples were cut and polished using sand papers of #1200, #2400, and #4000 sequentially to achieve sufficient surface smoothness for investigation. The final polish of the sample surfaces was done by using a 1-μm diamond paste on a polishing cloth for transmittance measurements. The sample thickness was prepared to be within 2 ± 0.05 mm.

Transmission electron microscopy (TEM) of epoxy nanocomposites was performed using a JEOL 2010 high-resolution TEM operated at 200 kV. All expoxy

samples were produced through ultramicrotomy (Reichert-Jung Ultracut-E microtome) to create thin sections of around 80 nm in thickness.

7. 3.   Results and Discussion

7. 3. 1. TEM Observations of QD Dispersion

TEM images of an epoxy/ZnO cross-section and various epoxy hybrid nanocomposites containing different QD and nanoplatelet volume fractions are given in Figure 7.2. Generally speaking, ligand-free colloidal ZnO QDs are unstable in epoxy resins *[190]*, thus large (100s of nanometers to microns) ZnO aggregates form after their incorporation into the matrix, as shown in Figure 7.2A. After adding exfoliated ZrP nanoplatelet s, however, nanoscale dispersion of ZnO QDs is achieved. At $\phi_{ZnO} = 0.004$ and $\phi_{ZrP} = 0.002$, QDs are well dispersed with the average 2D aggregate containing around 5 to 10 QDs (Figure 7.2B and its inset). If the QD concentration increases to $\phi_{ZnO}=0.008$ and the nanoplatelet loading is maintained at $\phi_{ZrP} = 0.002$, QDs are still homogeneously dispersed, but the average aggregate contains 10 to 20 particles (Figure 7.2C). On the other hand, if the nanocomposite is composed of either ZnO at $\phi_{ZnO} = 0.002$ and ZrP nanoplatelet s at $\phi_{ZrP} = 0.002$ (Figure 2d) or ZnO at $\phi_{ZnO} = 0.004$ and ZrP at $\phi_{ZrP} = 0.004$ (Figure 7.2E), the QDs reach a completely dispersed state, more or less. Insufficient nanoplatelet loading, e.g. $\phi_{ZnO} = 0.004$ with $\phi_{ZrP} = 0.0004$ (Figure 7.2F), led to large aggregate formation, similar to that observed in the epoxy/ZnO composite cross-section shown in Figure 7.2A.
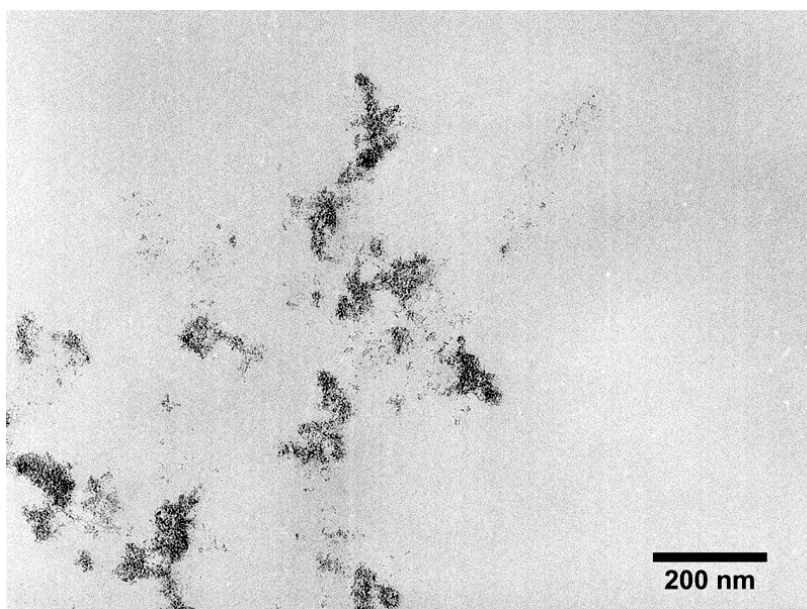
A
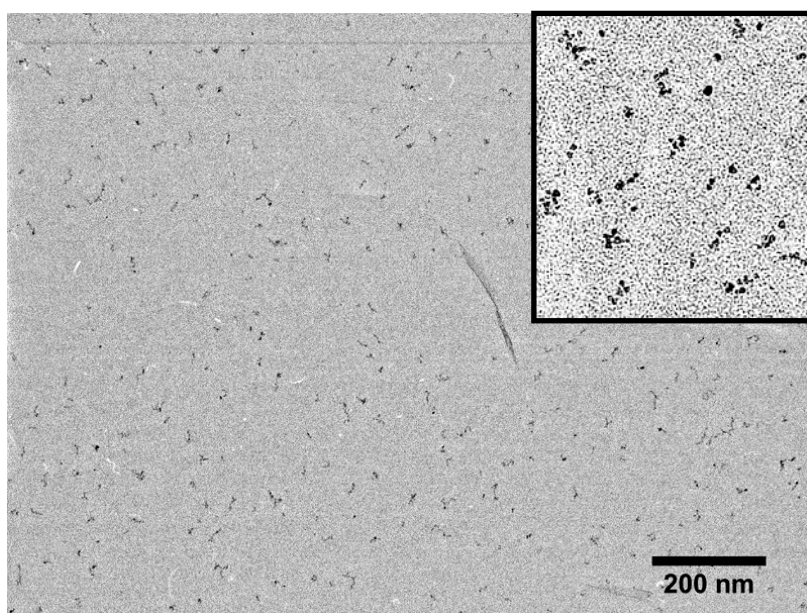
B

Figure 7.2. TEM images of epoxy nanocomposites. The insets are high-magnification images showing the representative QD aggregate sizes.
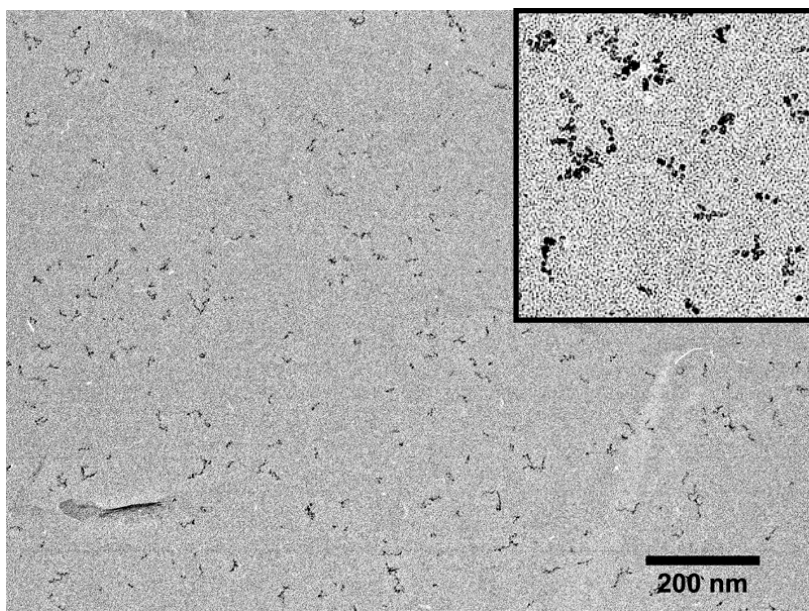
C
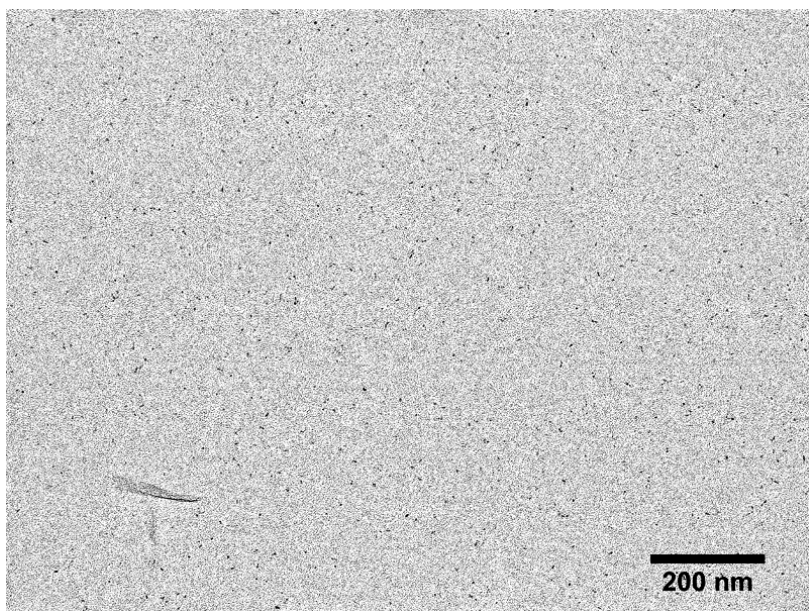
D

Figure 7.2. Continued.
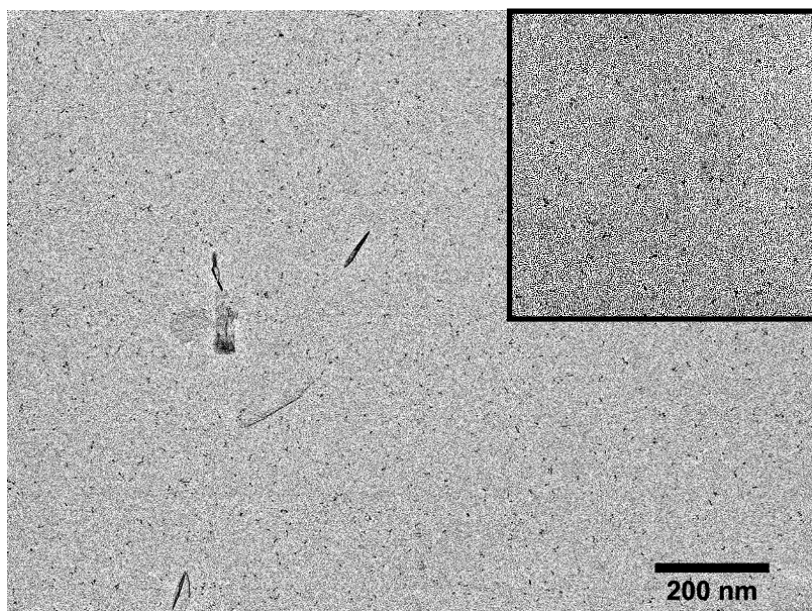
E
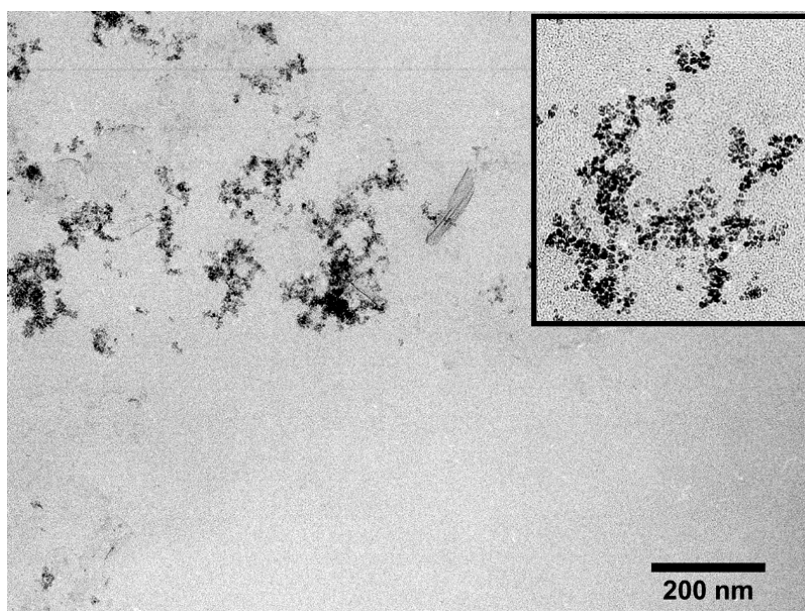
F

Figure 7.2. Continued.

7. 3. 2. Aggregate Size Estimation

To describe ZnO aggregate size in more quantitative terms, analysis of TEM images using ImageJ yielded two-dimensional radius of gyration (R_g^{2D}) estimates, which will be used later in this chapter to help explain the nature of the dispersion mechanism. Figure 7.3 shows the R_g^{2D} distributions found for each composite system. The maximum projected length of a diffusion-limited aggregate, L, from a 2D TEM image is related to R_g^{2D} through $L/3 \cong R_g^{2D}$. The three-dimensional radius of gyration (R_g^{3D}) of the aggregate can be estimated by $R_g^{3D} = 1.24 R_g^{2D}$ [191, 192]. It should be noted that these approximations are not valid for aggregates smaller than about five particles, so the estimates in Figure 7.3C and D are cluster sizes directly measured from TEM image.

A

B
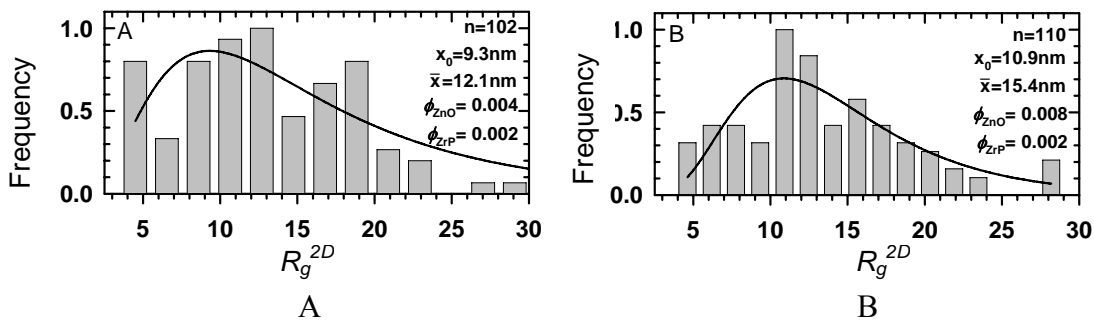
Figure 7.3. Distributions of R_g^{2D} found from analysis of TEM images, where n is the number of aggregates used to create each distribution. Log-normal fits are given for a-d to yield the value of the distribution's peak (x_0), and the arithmetic mean ($\bar{x}$) of the distribution is also given. (A) – (E) represent the analysis from the TEM images shown in Figure 7.2 B – F, respectively.
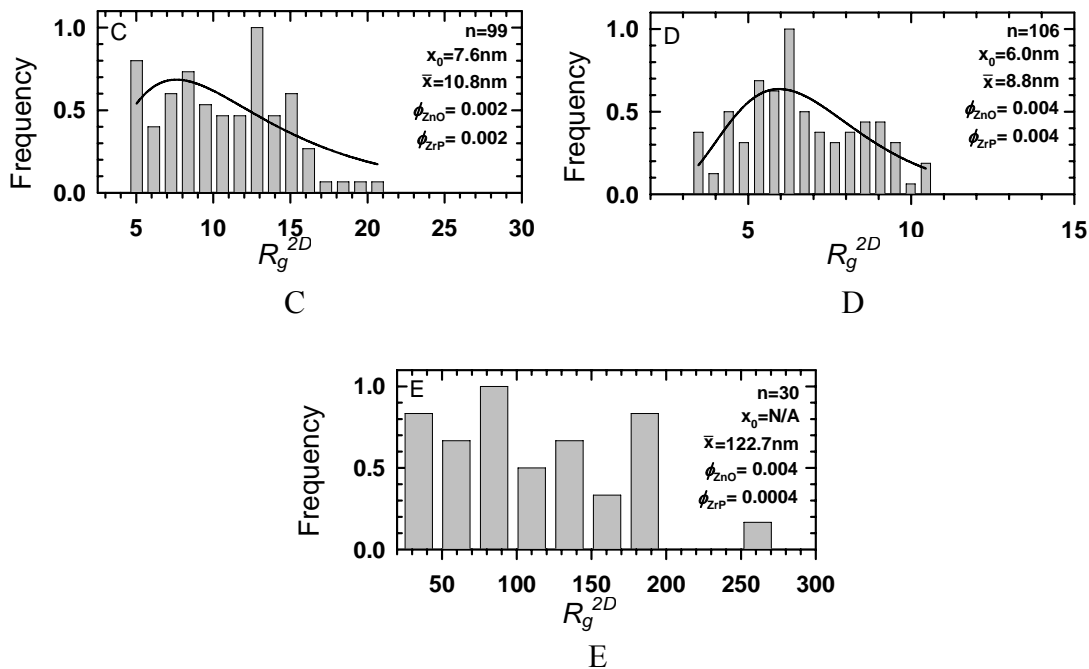
Figure 7.3. Continued.

7. 3. 3. Optical Transmittance Spectra

Figure 7.4A shows the light transmission spectra of neat epoxy, epoxy/ZnO, and epoxy/ZnO/ZrP specimens. The neat epoxy sample cuts off light below ~370 nm and reaches a maximum transmittance of about 91% within the range examined. The light transmittance T_m of a pure epoxy matrix for a monochromatic light is estimated by the following [193]:

$$T_m = (1-R)^2 \exp(-\alpha h) \tag{1}$$

Where R is the surface reflection and is defined by $R = (n-1)^2 / (n+1)^2$, α is the loss factor, h is the thickness of the specimen, and n is the refractive index of the neat epoxy matrix. The refractive index of a typical DGEBA/amine system varies from 1.54 to 1.58,

due to density variations *[194]*. Assuming $\alpha = 0$ and $n = 1.56$, the estimated maximum light transmittance of the neat epoxy should be about 90.5%, which is very close to our experimental finding of 91%. Therefore, α of our neat epoxy system approaches 0 for $\lambda > 600$ nm.
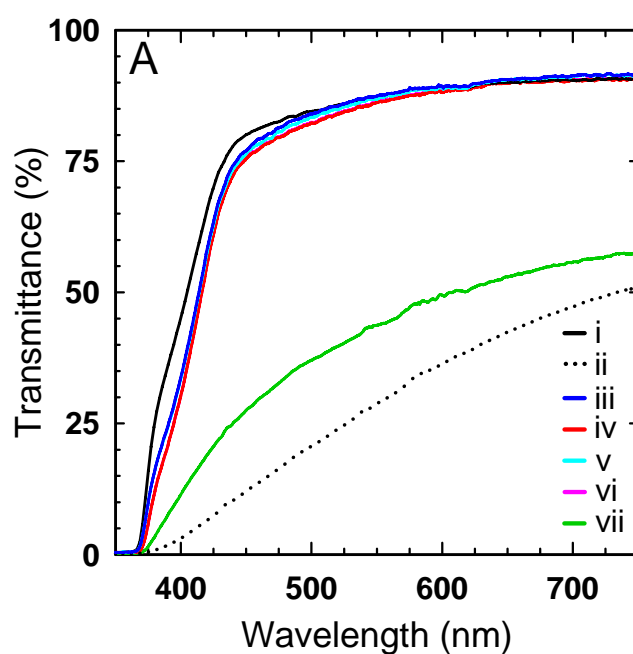
A

Figure 7.4. (A) Light transmission spectra of (**i**) neat epoxy, (**ii**) epoxy/ZnO (ϕ_{ZnO}=0.004), (**iii**) ϕ_{ZnO}=0.004 + exfoliated ZrP at ϕ_{ZrP}=0.002, (**iv**) ϕ_{ZnO}=0.008 + exfoliated ZrP ϕ_{ZrP}=0.002, (**v**) ϕ_{ZnO}=0.002 + exfoliated ZrP at ϕ_{ZrP}=0.002, (**vi**) ϕ_{ZnO}=0.004 + exfoliated ZrP at ϕ_{ZrP}=0.004, and (**vii**) ϕ_{ZnO}=0.004 + exfoliated ZrP at ϕ_{ZrP}=0.0004 and (B) photographic images of samples (**i**), (**ii**), and (**iii**).
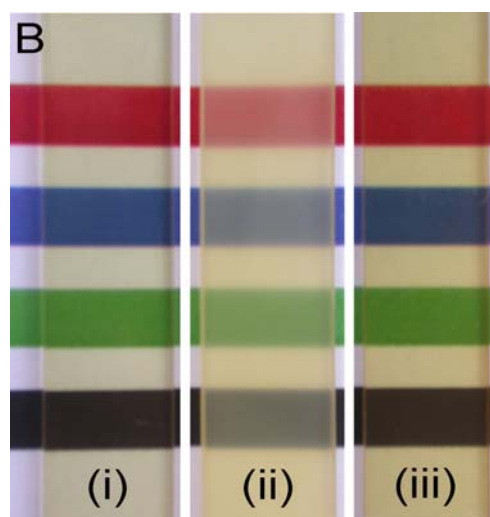
B

Figure 7.4. Continued.

All of the epoxy/ZnO/ZrP nanocomposites containing well-dispersed ZnO QDs and exfoliated ZrP NPs have transmittance spectra very similar to that of the neat epoxy system, except between 370 and 550 nm where epoxy/ZnO/ZrP specimens show a slightly red-shifted and attenuated transmittance. This is most likely due to the ZnO QDs absorbing light within this range. In sharp contrast, epoxy/ZnO nanocomposites containing large ZnO aggregates (see TEM in Figure 7.2A) exhibit a much lower transmittance than both the neat epoxy and hybrid nanocomposites, leveling off at ~55% near 600 nm and above. Photographic images of the neat epoxy, epoxy/ZnO, and an epoxy/ZnO/ZrP nanocomposite are given in Figure 4B. The specimen containing only ZnO QDs is translucent, while the epoxy hybrid nanocomposite filled with aggregates composed, on average, of about 10 QDs (see TEM in Figure 7.22B) is highly transparent

and similar to the neat epoxy. Qualitatively, the light transmission spectra and photographic images clearly demonstrate that the hybrid nanocomposites contain ZnO QDs with a much better degree of dispersion than that seen in the epoxy/ZnO system, which is in agreement with the TEM results.

As for the case of the epoxy hybrid nanocomposites where QDs are not well dispersed (Figure 2F) with less ZrP nanoplatelets, optical transmittance is still higher than that of the epoxy/ZnO nanocomposite, clearly indicating that exfoliated nanoplatelets impact the degree of QD dispersion, even at very low volume fractions. Based on the spectral data, if QDs are dispersed down to nanoscale aggregates containing fewer than 20 particles, light scattering and absorption within the range of visible wavelengths examined are minimal. Therefore, the transparency of the polymer matrices can be maintained, which is highly desirable for many composite applications.

7. 3. 4. Dispersion Mechanism

Nanoplatelet-assisted dispersion of ZnO QDs could involve a single or several chemical or physical mechanisms. For example, diffusing NPs could alter the kinetics of aggregate formation by physically disrupting the association of QDs (note that hydrodynamic mixing is not relevant here due to the tremendously low Reynolds number at these length scales (10^{-9}-10^{-7} m) and diffusive rates ($\sim 10^{-8}$ m/s)). In an alternative fashion, the ligand-free ZnO QDs could be passivated by an adsorbed layer of excess TBA that remains after the nanoplatelet exfoliation step. Furthermore, ZrP nanoplatelet s and/or excess TBA could be shifting the pH or interacting with the matrix

to sequester ZnO-phobic portions of the polymer. Various control experiments were conducted, therefore, to determine the extent to which any one of these factors plays a role in ZrP dispersing ZnO QDs at such low nanoplatelet volume fractions.

The most obvious control experiment to perform was to determine if excess TBA was behaving as a surfactant and absorbing onto the QD surface, thereby forming an electrosteric stabilizing layer that would facilitate QD dispersion. We prepared epoxy/ZnO samples with TBA^+OH^- but without NPs. More specifically, the samples contained ZnO at $\phi_{ZnO} = 0.004$ and TBA at a loading equal to that of the TBA mass used within the sample composed of exfoliated ZrP at $\phi_{ZrP} = 0.002$ (see cross-section shown in Figure 7.2B). Just as in the case of epoxy/ZnO, we observed large ZnO aggregates in HRTEM images and specimens were translucent with nearly identical optical properties to that of the epoxy/ZnO cross-section shown in Figure 2A and Figure 4A(ii), indicating that excess, freely diffusing TBA within the epoxy matrix is not responsible for ZnO QD stabilization.

To understand whether nanoplatelet s could be breaking up or slowing down the formation of QD aggregates in a physical or dynamic manner, several experiments were conducted. Here, the characteristic timescale of QD aggregate formation to the timescales of nanoplatelet and QD diffusion is estimated by assuming that the QD and nanoplatelet volume fractions within the current systems are below the limit that results in multiparticle hydrodynamic interactions and an associated increase in effective viscosity*[195]*.

In order to model the diffusive behavior of the 100 nm ZrP nanoplatelet s, their geometry can be approximated as oblate ellipsoids with principal dimensions of $2a$, $2b$, and $2c$ with $b = c$ and $b/a \gg 1$, where a represents nanoplatelet thickness and b is equivalent to nanoplatelet radius, r_{ZrP}. The friction factors take the following form[196]:

$$f_{\square} = 16\pi\mu_0 \left(a^2 - b^2\right) / \left[\left(2a^2 - b^2\right)S - 2a\right] \text{ and } f_{\perp} = 32\pi\mu_0 \left(a^2 - b^2\right) / \left[\left(2a^2 - 3b^2\right)S + 2a\right],$$

where μ_0 is the matrix/medium viscosity at infinite particle dilution and S is defined by

$$S = \left(2/\sqrt{b^2 - a^2}\right)\tan^{-1}\left(\sqrt{b^2 - a^2}/a\right).$$ As $b/a \rightarrow \infty$, the friction factors can be simplified to

$f_{\perp} = 32\mu_0 r_{ZrP}/3$ and $f_{\square} = 16\mu_0 r_{ZrP}$. The perpendicular and parallel diffusion coefficients of the nanoplatelets are then given by $D_{\perp} = kT/f_{\perp}$ and $D_{\square} = kT/f_{\square}$, and the effective diffusive coefficient of the ZrP nanoplatelets, $\bar{D}_{ZrP}$, is described as

$\bar{D}_{ZrP} = \left(D_{\square} + 2D_{\perp}\right)/3$ [197]. The diffusion coefficient of a spherical ZnO QD of radius r_{ZnO} with the Stokes-Einstein equation can be given by[198]:

$$D_{ZnO} = \frac{kT}{6\pi\mu_0 r_{ZnO}}. \tag{2}$$

The ratio of the diffusion coefficients of QDs to nanoplatelets s is, then,

$$\frac{D_{ZnO}}{\bar{D}_{ZrP}} = \frac{2}{\pi}\left(\frac{r_{ZrP}}{r_{ZnO}}\right). \tag{3}$$

From eq. 3, the diffusion coefficient of a 5 nm ZnO QDs is about 12.5 times greater than that of 100 nm ZrP nanoplatelets if the two species are freely diffusing. Once crosslinking is initiated, on the other hand, this ratio becomes invalid because nanoplatelet mobility is far more affected by local polymer entanglements than that of

QDs because of their geometry and size. As the matrix becomes more crosslinked, the diffusive rates of both colloidal species will drop significantly and eventually tend to zero. Because of the difference in diffusive rates, we can safely assume that nanoplatelets would be unable to substantially affect the formation of ZnO QD aggregates through purely kinetic means, especially if the clusters are formed on short timescales through diffusion-limited aggregation. Although we do not know the reaction rate of QD association, we observed the formation of QD aggregates within the epoxy resin when nanoplatelets are absent only moments after the addition of ZnO, so we can reasonably approximate the clustering as diffusion-limited. Further refuting the argument that QD clustering is physically disrupted by diffusing NPs, is the fact that an undisturbed and non-crosslinked epoxy resin mixture that we prepared with ZnO QDs at $\phi_{ZnO} = 0.004$ and exfoliated ZrP at $\phi_{ZrP} = 0.004$ has now remained devoid of visible QD clusters for over one year. Finally and most importantly, the observation of individually dispersed QDs and small clusters in our epoxy composites (Figure 2D and E) cannot be explained by nanoplatelet disruption of the QD aggregate formation.

Experimental results in the literature indicate that the diffusion coefficient of nanoparticles of this size, freely moving in polymer melts, can be up to 200 times greater than that predicted by eq. 2 [199], while nanoplatelet diffusion at infinite dilution is accurately predicted by the above analysis [200]. It has been shown with molecular dynamics simulations that the Stokes-Einstein equation is valid for nanometer-scale particles larger than the radius of gyration of the suspending polymer[201]. Because the contour length of DER 332 is approximately 2 nm [202], the QDs used in this study are

several times larger than the monomer's radius of gyration, so it is safe to assume eq. 3 is reasonable. Furthermore, any deviation from this model says that the QDs would be diffusing at faster rates than predicted, which bolsters the argument that the nanoplatelets cannot disrupt the QD aggregate formation through solely kinetic means.

When directly added to hexane, acetone, methanol, and deionized water, ZnO QDs aggregate and drop out of suspension. The observed rates of ZnO aggregate formation and sedimentation are quite different in these media and have the following ranking in order from slowest to fastest: methanol, acetone, DI water, and then hexane. Of interest is the fact that this order also follows the ranking of dipole moment magnitudes of these solvents, with methanol having the largest of the four. In the case of acetone and methanol, the addition of ZrP nanoplatelets prior to the addition of QDs prevents visible QD aggregates from ever forming, and nanoplatelets added after QD aggregates are allowed to form break large clusters up into much smaller aggregates. In contrast, ZrP nanoplatelets are ineffective at preventing QD aggregates from forming if the dispersion is produced in water or hexane. Optical transmittance spectra of dispersion experiments in acetone are given in Figure 7.5. The optical transmittance spectrum of ZnO QDs (3 mg·mL^{-1}) in acetone without the addition of nanoplatelets shows a significant attenuation (Figure 7.5, data iii), whereas the addition of ZrP nanoplatelets at 3 mg·mL^{-1} prevents or significantly reduces the formation of aggregates. After one year, this same suspension remains fairly stable (Figure 7.5, data vi) with only a small increase in average aggregate size, evidenced by the red-shifted spectrum.
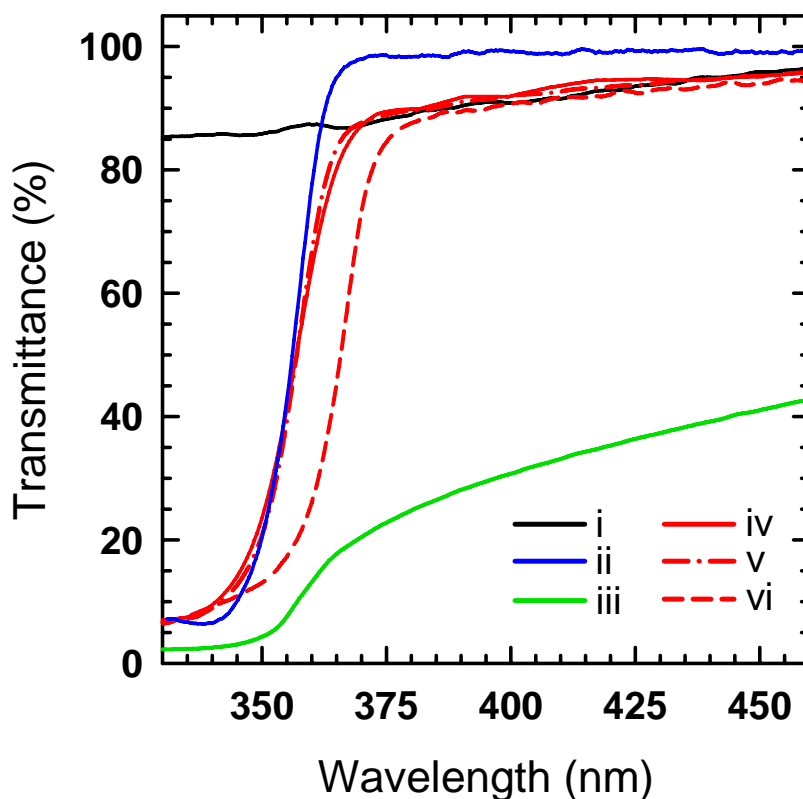
Figure 7.5. Optical transmittance spectra of (**i**) 100 nm exfoliated ZrP nanoplatelets dispersed in acetone, (**ii**) ZnO QDs dispersed in methanol, (**iii**) ZnO QDs in acetone, (iv) ZnO QDs + ZrP nanoplatelets in acetone at 0 hr, (**v**) ZnO QDs + ZrP nanoplatelets after 3 hr, (**vi**) ZnO QDs + ZrP nanoplatelets after 1 year. ZnO and ZrP are at concentrations of 3 mg/mL for all cases.

These experimental results with simple solvents are important because they show that the nanoplatelets are impacting the medium-QD interactions, but how NPs bring about this change is not obvious. One possible explanation is that nanoplatelets could be polarizing the medium in the vicinity of a QD. In the case of methanol and acetone, electrons on the oxygen atom are relatively mobile and these solvents have the potential

to become more electronegative in the presence of a nanoplatelet through dipole-dipole interactions, which would increase the interaction of the solvent with the Zn atoms on the surface of the QD. In the case of water and hexane, the dipole moments may be below the polarization threshold that enhances the polar bonding between the solvent and QDs to the point where the QDs redisperse. In the case of the epoxy used in our study, the monomer has two ethers on opposite ends of the molecule, which also have the potential to become highly polarized. Moreover, successful dispersions in other polymers with ether groups, e.g. DER 331 epoxy (later this chapter) and PMMA (next chapter), indicating polarizability may be the key characteristic for the approach to work.

To explore the possibility of nanoplatelets altering the pH of the dispersion, which could drastically shift the surface charge of the QDs and induce electrostatic stabilization, the pH values for various dispersions and solutions at different nanoplatelet and TBA concentrations is measured (Table 7.1). The differences between these measurements can be considered negligible, except for the case of TBA in acetone and water. Even so, the control experiments with TBA demonstrate that a large increase in pH does not lead to electrostatic stabilization, and the pH of ZrP modified with TBA in both acetone and water is roughly equivalent to that of ZnO QDs dispersed in methanol.

Table 7.1. Measured pH values for nanoplatelet and QD dispersions and TBA solutions at two different concentrations.

	0.3 mg/mL	3 mg/mL
ZrP (TBA) in H_2O	7.26	7.73
ZrP (TBA) in acetone	8.04	8.94
Non-exfoliated ZrP in H_2O	6.56	6.11
TBA^+OH^- in H_2O	10.82	–
TBA^+OH^- in acetone	12.22	–
ZnO in methanol	8.10	–

To begin to assert that nanoplatelets can locally alter QD-matrix interactions through a mechanism such as transient polarization of the medium, we must first evaluate the timescales for QD aggregate formation and NP influence on the surrounding medium as a function of ϕ_{ZnO} and ϕ_{ZrP}. For a monodisperse suspension of spherical particles, the average cluster mass is defined by[198]

$$\overline{M} = (R_g^{2D} / r_{ZnO})^{d_f} \qquad (4)$$

where R_g^{2D} is the projected radius of gyration of the aggregate, and d_f is the fractal dimension. Since we have no reasonable estimate of particle-particle potential, we can begin by making the conservative assumption that QD clusters form by diffusion-limited aggregation, creating fractal structures with $d_f \cong 1.8$ [203, 204]. The characteristic time, t_a, to form a cluster of average mass is calculated as[198]

$$t_a = t_d \left[(R_g^{2D} / r_{ZnO})^{d_f} - 1 \right]$$

(5)

where t_d is the time for doublet formation expressed by

$$t_d = \frac{\pi \mu_0 r_{ZnO}^3 W}{\phi_{ZnO} kT},$$

(6)

with the stability ratio, W, equal to 1 for diffusion-limited aggregation *[198]*. Note that in these calculations the viscosity was assigned a value of 5000 cp *[202]*. But, the accuracy of this parameter is not critical since viscosity is assumed to impact the diffusive behavior of nanoplatelets and QDs with the same linear dependence.

The other important timescale is that of NPs sampling their characteristic volume, which is related to $\bar{D}_{ZrP}$ and ϕ_{ZrP}. If one assumes that the ZrP nanoplatelets can redisperse QD aggregates within a surrounding volume defined by r_{ZrP}, then the timescale for a nanoplatelet to adequately sample its characteristic volume is given by eq. 5, where r_{ZrP} is substituted for r_{ZnO} and ϕ_{ZnO} is replaced by an effective nanoplatelet volume fraction ($\phi_{eff} = 4 r_{ZrP} / 3a$ with a defined as nanoplatelet thickness) that takes into account the difference between doublet formation of spheres and doublet formation of NPs with each nanoplatelet occupying a volume equal to that of a sphere of radius r_{ZrP}. Note that the timescale for rotational diffusion is not included in these analyses for two reasons: an analytical model of platelet diffusion for aspect ratios less than 0.3 is absent from the current literature and we are not able to predict the minimum separation

between a nanoplatelet and QD cluster at which solvent conditions are changed to a point where QDs return to a disperse state.

The plot in Figure 7.6 gives the relation between the projected radius of gyration of an average aggregate and its time for formation for the three experimental values of ϕ_{ZnO} that we examined with TEM. Three of the open symbols in Figure 7.6 correspond to the predicted times for a nanoplatelet to sample its characteristic volume at a given value of ϕ_{ZrP}. Therefore, the location of these points along each line defines the expected values of R_g^{2D} for given values of ϕ_{ZnO} and ϕ_{ZrP}. If we assume that the epoxy samples serve as a "fossilized" record of the dispersion state within the pre-crosslinked epoxy, the colored symbols in Figure 7.6 correspond to t_a estimated for average experimental values of R_g^{2D} obtained from TEM analyses (see Figure 7.2B – F and Figure 7.3A – E). The fact that experimental R_g^{2D} values are smaller than that predicted by the rudimentary analyses probably indicate that ZnO QD aggregates form under reaction-limited rather than diffusion-limited conditions. Nevertheless, these predictions are reasonably close to experimental t_a values, indicating that the assumptions may be fairly realistic. While this result does not validate the hypothesis, it helps to show that the proposed mechanism is a viable explanation of how ZrP nanoplatelets are able to disperse ZnO QDs in the solvents and polymeric systems investigated.
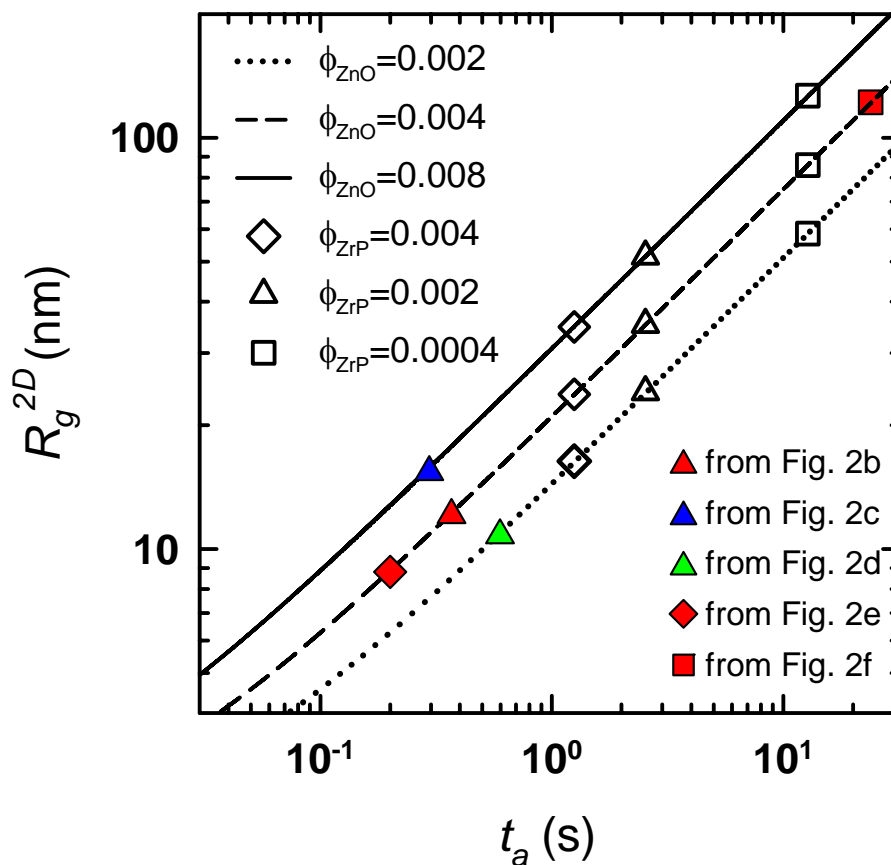
Figure 7.6. Characteristic time t_a for QD cluster formation of average R_g^{2D} for all ϕ_{ZnO} used in our studies. The open symbols ($\diamond$, $\triangle$, and $\square$) represent calculated times for ZrP nanoplatelets to sample their characteristic volume at different values of ϕ_{ZrP}. Open circles with labels correspond to R_g^{2D} values estimated from experimental results described in Figure 7.2B-F.

7. 3. 5. Effectiveness of Non-exfoliated Nanoplatelets

In another control experiment, non-exfoliated pristine ZrP crystals were used in hybrid nanocomposites to determine the importance of incorporating individually dispersed ZrP nanoplatelets. To prepare these composites, pristine ZrP was first

ultrasonicated in water to achieve a well-dispersed suspension of stacked ZrP platelets.

The samples were centrifuged, the supernatant was replaced with acetone,

ultrasonication was used again to redisperse and suspend the non-exfoliated

nanoplatelets, the nanoplatelets and ZnO were then incorporated into the epoxy resin,

and the samples were cured according to the aforementioned protocol. Figure 7.7 shows

TEM images of a hybrid nanocomposite cross-section composed of ZnO at $\phi_{ZnO} = 0.004$

and non-exfoliated ZrP NPs at $\phi_{ZrP} = 0.002$.
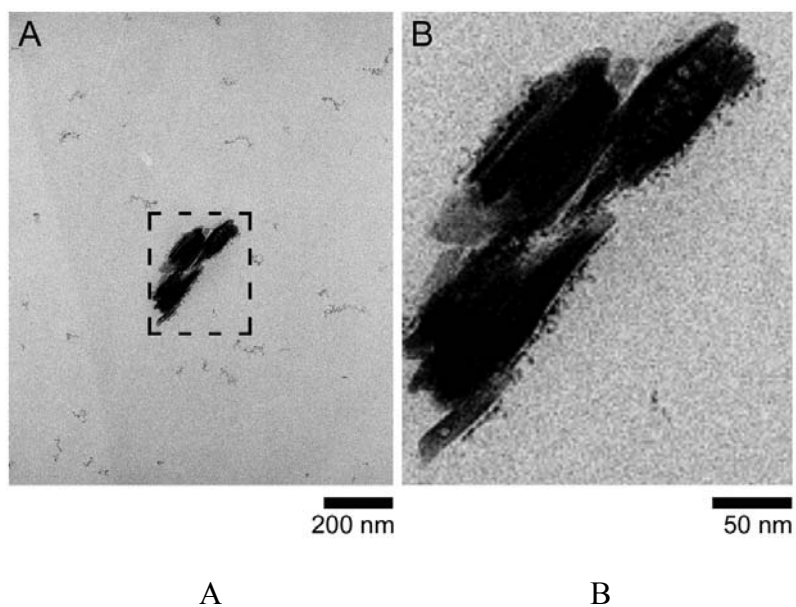
Figure 7.7. HRTEM images of an epoxy hybrid nanocomposite containing $\phi_{ZnO}=0.004$ + non-exfoliated ZrP nanoplatelets at $\phi_{ZrP}=0.002$. The overall degree of dispersion is captured in the (A) low-magnification image. In the (B) high-magnification image, the adsorption of QDs onto the ZrP surface is clearly visible. Optical transmittance spectra (C) of (i) neat epoxy (identical to Figure 7.3A(i)), (ii) epoxy with $\phi_{ZnO}=0.004$ + exfoliated ZrP nanoplatelets at $\phi_{ZrP}=0.002$ (identical to Figure 7.3A(iii)), and (iii) $\phi_{ZnO} = 0.004$ + non-exfoliated ZrP nanoplatelets at $\phi_{ZrP}=0.002$ (cross-section shown in (A) and (B) of this figure).
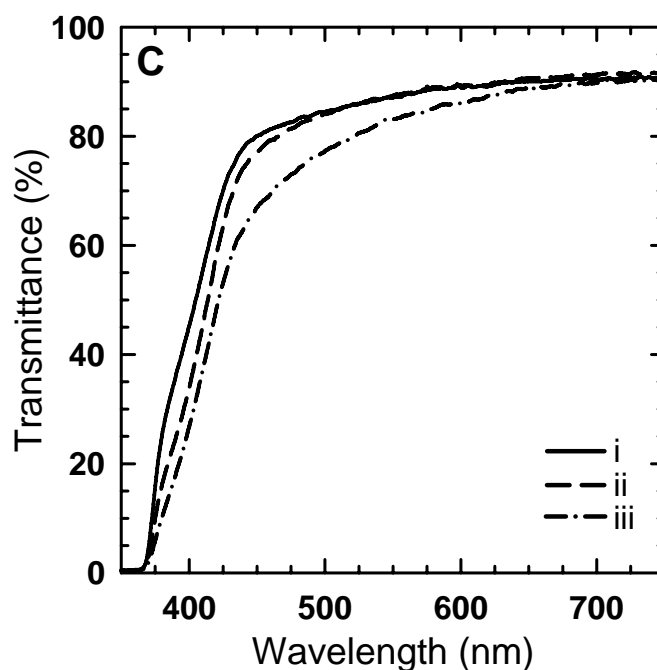
C

Figure 7.7. Continued.

Inside ZrP layers, hydrogen bonding between surface hydroxyl groups and crystalline water molecules holds the platelets together, and the surface of pristine ZrP is densely occupied by free hydroxyl groups that give rise to a negative surface charge *[189]*. With regard to colloidal ZnO QDs, it has been shown that, at a pH of ~8, anion vacancies exist on the surface of ZnO QDs, giving rise to a positive surface charge *[173]*. The pH of the ZnO dispersions in methanol was found to be 8.10, hence QDs do not associate with exfoliated nanoplatelets because adsorbed TBA$^+$ molecules impart a positive surface charge that repels the positively charged ZnO *[140]*. On the other hand, in the hybrid nanocomposites containing non-exfoliated ZrP, ZnO is electrostatically attracted to the surface of nanoplatelets (Figure 7.7). Interestingly, the remaining, non-

adsorbed ZnO in the epoxy matrix attained a semi-dispersed state, indicating that ZrP possibly affects the interaction of ZnO with the polymer even when it is not exfoliated into individual platelets. Another and perhaps more intuitive explanation is that the electrostatic adsorption of ZnO onto non-exfoliated ZrP significantly reduces the effective ϕ_{ZnO} within the epoxy matrix, and we are observing a degree of dispersion within a bulk of the matrix equivalent to a composite system with a much lower ZnO concentration. In other words, the non-exfoliated platelets are confining the QDs on their surface and depleting QDs from the remainder of the composite. Interestingly, the optical transmittance spectrum of this composite system is not too different from that of the neat epoxy (Figure 7.5C). This suggests that there is likely an enhanced degree of dispersion from the addition of ZrP.

7. 4.   Conclusions

A novel colloidal approach to disperse ligand-free ZnO QDs into polymeric matrices by utilizing nanoplatelets is introduced in this chapter. By adjusting the ratio between exfoliated nanoplatelets and QDs, the dispersion state of ligand-free ZnO QDs can be tuned from micro-sized aggregates to nano-scaled clusters, and even to individual level. From controlled experiments and dynamic analysis, a possible mechanism responsible for the nanoplatelet-assisted QD dispersion is proposed, that is, the presence of nanoplatelets affects QD-matrix and/or QD-QD interactions, perhaps through localized polarization of the medium, in such a way that the QD aggregation is strongly disrupted by the presence of nanoplatelets, the rate of which depends on the ratio

between the two. Our experimental findings suggest that the interaction of ZrP nanoplatelets with the polymer, and media such as acetone, changes the thermodynamic character of the matrix, thereby facilitating the dispersion of ZnO QDs through an increase in their favorable interaction with the surrounding medium. Furthermore, dispersion tuning is achieved at low volume fractions of exfoliated nanoplatelets due to the geometry of the nanoplatelets.

CHAPTER VIII

DISPERSION – PROPERTY RELATIONSHIP IN POLYMER/QD

NANOCOMPOSITES[*]

8. 1.   Introduction

One of the unique characteristics of the zero-dimensional quantum dots (QDs) is

their size-dependent electrical and optical properties, known as quantum size effects

[28], where the photogenerated electron-hole pair is three-dimensionally confined in the

dot boundary and the band-edge absorption and emission are functions of the QD size.

Extensive experimental and theoretical efforts have been made to explore the details of

the electronic structure in QDs with variation in sizes *[1, 6, 35, 36, 205]*,

Besides quantum size effects, the optical properties of QDs also depend strongly

on the inter-dot distance *[47]*, In systems where small colloidal QD aggregates form, the

optical absorption and photoluminescence have been shown to exhibit red-shifting as

compared to the highly dispersed QD colloids *[7]*, The dried QD powder aggregates also

exhibit similar photoluminescence to the bulk material *[183]*, Furthermore, it has been

demonstrated that electronic energy can be transferred in between organically capped

QDs at the inter-dot separation up to 10 nm through long-rang resonance *[33, 34]*, As

they become in direct contact each other to form a close-packed QD solid, QDs would

show similar optical properties to the bulk due to their strong coupling effect *[184]*, Therefore, in theory, the optical properties of monodisperse QDs are a function of their dispersion state in a medium such as in polymers, suggesting that the optical properties of polymer/QDs nanocomposites can be tuned by controlling the state of the QD dispersion. However, to date, the above phenomenon has not yet been experimentally shown due to the difficulty in obtaining the controlled dispersion of these inorganic QDs in polymers, especially without the use of organic capping agents *[51]*,

Base on the finding introduced in the previous chapter that the dispersion states of ligand-free ZnO QDs in polymers can be tuned *via* the use of exfoliated nanoplatelets (alpha-zirconium phosphate, ZrP), in this study, a systematic investigation on the tuning of optical properties of such polymer nanocomposites, which contain controlled dispersion of monodisperse ZnO QDs in epoxy, has been performed. The physical chemistry responsible for the observed optical property variations due to the state of QDs dispersion in polymers is discussed.

8. 2.   Experimental

8. 2. 1. Preparation ZnO QDs and ZrP Nanoplatelets

The details on the preparation of ZrP nanoplatelets and ZnO QDs can be found in the **Chapter III** and **VI**, respectively. The purified ZnO QDs with an average particle size of 5.0 nm were fully redispersed in methanol with a concentration of 0.4 M to be incorporated into epoxy. A small amount of the sample was taken out for optical

properties measurements. Several batches of ZnO QDs were prepared according to the above procedure to demonstrate consistency and for systematic investigations.

8. 2. 2. Preparation of Polymer/QD Nanocomposites

Diglycidyl ether of bisphenol A (DGEBA) epoxy resin (D.E.R.^{TM} 331 epoxy resin, The Dow Chemical Company) with an average epoxide equivalent weight of 190 was first dissolved in acetone with exfoliated ZrP nanoplatelets in a flask. Then, ZnO QDs were quickly added into the above solution after they were purified and redispersed in methanol. Subsequently, the solvents were removed in a rotovapor under vacuum at 80 °C.

After solvent evaporation, the epoxy resin containing both types of nanoparticles remained clear and was then cooled to room temperature. The curing agent, Ancamine 1618 (Air Products), was added into the epoxy resin according to the manufacture's recommendation. After mixing, the epoxy was poured into a pre-heated mold, cured at 80 °C for 24 hours, and then post-cured at 100 °C for three hours in an oven. After curing, the sample was left in the oven and cooled to room temperature. Epoxy sample containing both types of nanofillers is designated as epoxy hybrid nanocomposite. Epoxy hybrid nanocomposites with 0.5 wt.% of exfoliated ZrP nanoplatelets and 0.5, 1.0, 1.5, and 2.0 wt.% of ZnO QDs were obtained, labeled as samples **b**, **c**, **d**, and **e**, respectively. Epoxy samples cured with 1.0 and 2.0 wt.% of ZnO QDs, designated as epoxy/ZnO nanocomposites, were also prepared, and labeled as samples **f** and **g**, respectively. For comparison purposes, a neat epoxy sample without fillers, labeled as

sample **a**, and an epoxy sample cured with only 0.5 wt. % of exfoliated ZrP nanoplatelets, labeled as sample **h**, were also prepared through the same curing procedure. For clarity, the model systems utilized for the present study are listed in Table 8.1.

Table 8.1. Epoxy samples used in this study

| Sample | Filler concentration | | Name |
	ZnO QDs (wt.%)	ZrP nanoplatelets (wt.%)	
a	0	0	Neat epoxy
b	0.5	0.5	Epoxy hybrid nanocomposites
c	1.0	0.5	Epoxy hybrid nanocomposites
d	1.5	0.5	Epoxy hybrid nanocomposites
e	2.0	0.5	Epoxy hybrid nanocomposites
f	1.0	0	Epoxy/ZnO nanocomposites
g	2.0	0	Epoxy/ZnO nanocomposites
h	0	0.5	Epoxy/ZrP nanocomposites

Thermoplastics/QD nanocomposites were prepared using polymethyl methacrylate (PMMA, M_n=80,500, Sumitomo Chemical Co., Japan). PMMA was dissolved in acetone with exfoliated ZrP nanoplatelets first, and then the ZnO/methanol was added with stirring. The solution mixture was clear throughout, indicating a homogeneous dispersion of ZnO QDs in the solution. Subsequently, the solution was cast on a Petri-dish and the solvents were evaporated under vacuum at room temperature to obtain the film sample. The PMMA nanocomposite samples containing both nanofillers are designated as PMMA hybrid nanocomposite films or PMMA/ZnO/ZrP nanocomposite films.

In this study, PMMA hybrid nanocomposite films with various concentrations of ZnO QDs and ZrP nanoplatelets were prepared. For reference, neat PMMA film and PMMA containing only ZnO QDs (designated as PMMA/ZnO nanocomposite film) were also prepared by the same procedure. The thicknesses of all the films were controlled to around 30 μm by adjusting the concentration and amount of solution utilized. After solvent evaporation, the film samples were heated at 120 °C under vacuum for 2 hours to remove any solvents trapped in the polymers.

8. 2. 3. Characterization

High resolution transmission electron microscopy (TEM) observations of polymer nanocomposites were carried out using a JEOL 2010 HR-TEM operated at 200 kV. The polymer samples were prepared by using Reichert-Jung Ultracut-E microtome with thin section thicknesses of around 70-100 nm.

UV-vis spectra of the colloidal ZnO QDs, polymer nanocomposites were recorded on a Hitachi (model U-4100) UV-vis-NIR spectrophotometer under both absorbance and transmittance modes. The cured epoxy samples were cut and then polished using sand papers of #1200, #2400, and #4000 in sequence to achieve surface smoothness for investigation. Final polishing of the sample surface was done by using 1 μm diamond paste on a cloth for optical property measurements. The sample thickness was prepared to be within 2 ± 0.05 mm. Photoluminescence (PL) spectra were recorded using a PTI QM-4/2006 spectrofluorometer. A photon counter was used for detection. Optical measurements of PMMA nanocomposites were carried out directly using the film samples.

8. 3.   Results and Discussion

8. 3. 1. Optical Properties of Monodisperse ZnO QDs

Monodisperse ZnO QDs were synthesized and purified as described in Chapter X. Figure 8.1 shows the optical absorption spectra of three batches of colloidal ZnO QDs prepared using the same procedure, which were also used to prepare the epoxy nanocomposites containing ZnO QDs in this study. These three batches of colloidal ZnO QDs have identical optical absorption spectra with an absorption onset at 359 nm, which is significantly blue-shifted when compared against the absorption onset of the bulk ZnO (370 nm at room temperature). Therefore, all the ZnO QDs prepared in different batches have reproducible optical properties in colloids before being incorporated into epoxy.
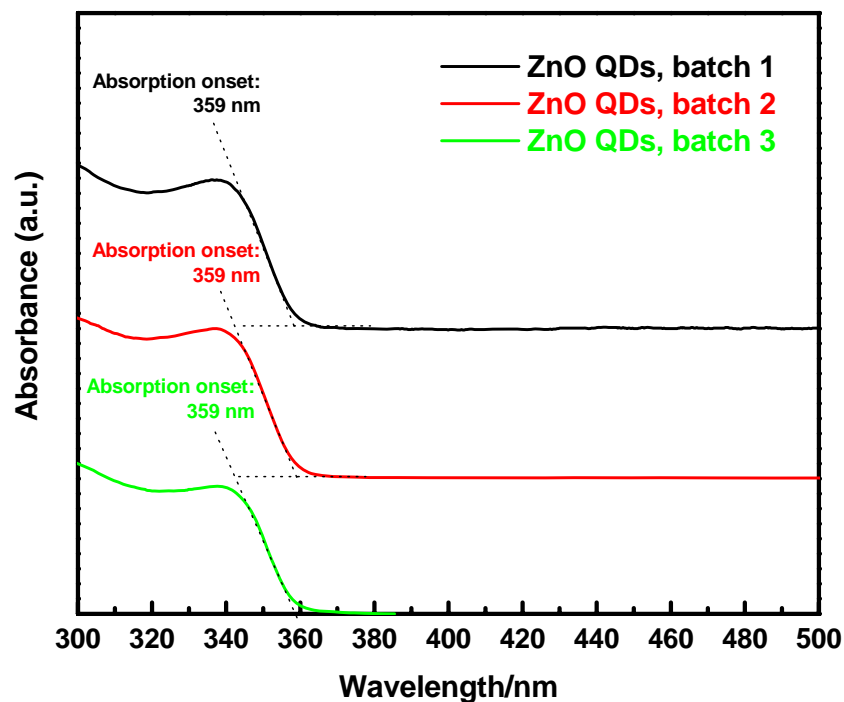
Figure 8.1. Optical absorption spectra of three batches of colloidal ZnO QDs obtained from the same synthetic procedure.

Generally, when a semiconductor absorbs a photon with energy higher than its bandgap, an electron–hole pair is created at the conduction and valence band, respectively. The bandgap energy of a semiconductor is the lowest energy gap between the valence band and the conduction band necessary to create an electron-hole pair. The bandgap energy of a semiconductor nanocrystal in a dispersed colloid can be determined experimentally from the optical absorption onset in the UV-vis spectrum[206]. The optical absorption onsets of three batches of colloidal ZnO QDs used in this study were determined from their UV-vis spectra (Figure 8.1). All these three batches of ZnO QDs

in colloids have the same absorption onset at 359.0 nm (corresponding to the bandgap energy of 3.45 eV), which is blue-shifted when compared to that of the bulk ZnO (3.35 eV at room temperature).

The size-dependent bandgap energy of a semiconductor nanocrystal can be obtained using an effective mass model *[2]*, where the bandgap energy E^* (eV) can be approximated by

$$eE^* = eE_g^{bulk} + \frac{\hbar^2 \pi^2}{2r^2}\left(\frac{1}{m_e^* m_0} + \frac{1}{m_h^* m_0}\right) - \frac{1.8e^2}{4\pi\varepsilon\varepsilon_0 r} + \text{smaller terms}$$

(1)

where E_g^{bulk} is the bulk band gap energy (eV), $\hbar$ is Plank's constant, r is the QD radius, m_e^* is the effective mass of electron, m_h^* is the effective mass of hole, m_0 is the mass of free electron, e is the charge of the electron, ε is the relative permittivity, ε_0 is the permittivity of free space, and the smaller terms are usually negligible. As for the case of ZnO, $m_e^* = 0.24$, $m_h^* = 0.45$, and $\varepsilon = 3.7$ are applied *[1]*. Eq. 1 is a simple one-band effective mass model. It shows good approximation for small bandgap semiconductor materials, such as CdSe. However, for the larger bandgap semiconductors, such as CdS, it usually fails to give correct prediction for QD radius $r > 3.0$ nm due to the strong electron-hole interaction, but gives a good approximation for sufficiently small QDs.*[2]* In this study, Eq. 1 was applied to check its validity for ZnO QDs. The calculation based on $r = 2.50$ nm (obtained from the TEM statistical analysis in **Chapter VI**) yields the bandgap energy $E^* = 3.454$ eV, which is close to that of 3.453 eV determined from the absorption onset in Figure 8.1. Moreover, a more accurate simulation for the

bandgap energy of ZnO QDs using a multi-band effective mass model *[207]* shows similar results to this simple one-band effective mass model shown in Eq. 1 at the QD radius from 1.50 to 2.50 nm. The experimental results obtained from the optical absorption spectra and the TEM images conducted in this study are consistent with the above theoretical calculations. This further validates the excellent correlation among the optical properties, the bandgap energies, and the sizes of our colloidal ZnO QDs. Therefore, monodisperse ZnO QDs with high purity prepared in this study is ideal for studying optical properties of QDs in polymers.

8. 3. 2. Dispersion State of ZnO QDs in Epoxy

Figure 8.2 shows the photographic images of samples **a-h**. Without an addition of exfoliated nanoplatelets, samples **f** and **g** are translucent. The higher the concentration of ZnO QDs, the lower transparency the epoxy/ZnO nanocomposites exhibit. However, after adding exfoliated ZrP nanoplatelets, samples **b-e** become highly transparent, which are similar to the neat epoxy (sample **a**). Figure 8.3 shows the TEM images of samples **b-g**. In samples **f** and **g**, no exfoliated nanoplatelets have been added and ZnO QDs form large aggregates in epoxy, which accounts for the low transparency shown in Figure 8.2. However, with the presence of exfoliated nanoplatelets, ZnO QDs are well dispersed in epoxy, which explains the high transparency of epoxy hybrid nanocomposites.
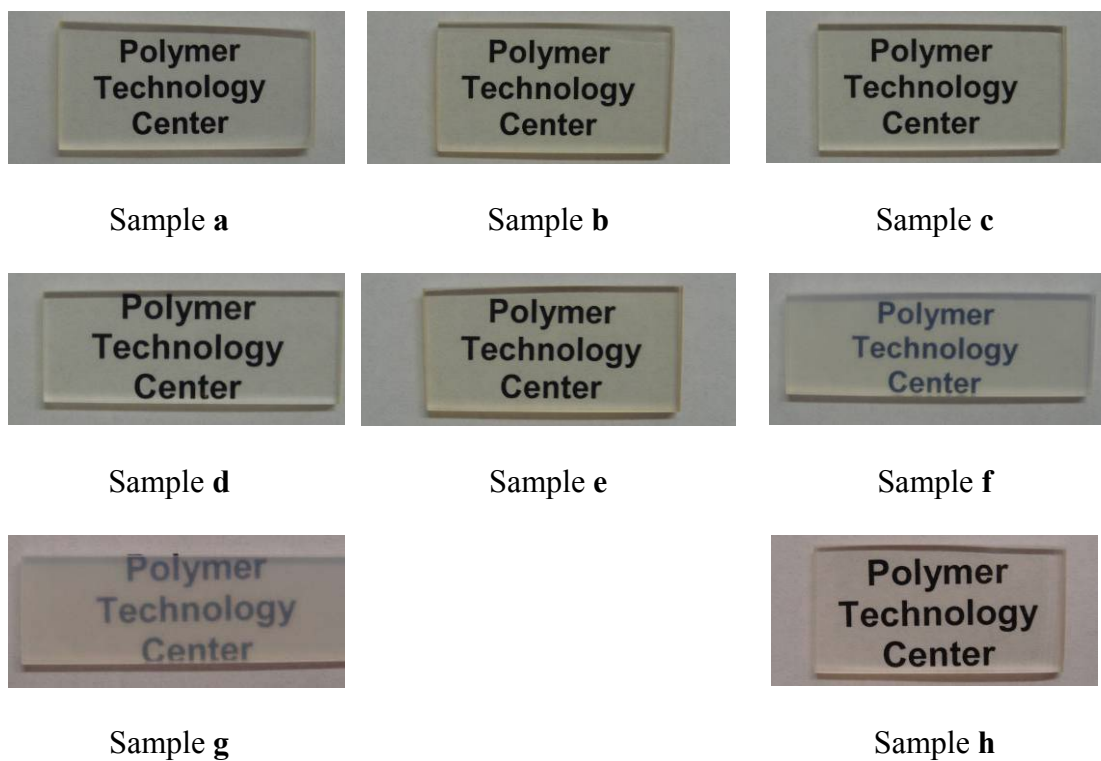
Figure 8.2. Photographic images of samples **a-h.**

The TEM images of samples **b-e** shown in Figure 8.3 indicate that most of ZnO QDs are individually dispersed in epoxy. In a glance, it appears that a small potion of QDs is packed close to each other. Upon detailed analysis, no aggregation of ZnO is present. In fact, when ZnO QDs are dispersed in solvents, they exhibit intensive Brownian motions due to their extremely small size, but keep dispersed because of the presence of electrical double-layer repulsion and other repulsive forces. In other words, the Zn QDs are dynamically dispersed. When ZnO QDs are incorporated into epoxy and cured, unlike in colloidal solution, they are "frozen" in the cured epoxy matrix. A separate study based on organically capped QDs *[8]* and cryo-TEM observation of a dispersed colloidal system *[208]* also show a similar dispersion state as shown in Figure 8.3. Therefore, it is plausible to claim that based on the TEM observations shown in Figure 8.3, ZnO QDs with addition of exfoliated nanoplatelets can well disperse ZnO QDs in epoxy. The dispersion mechanisms of QDs in polymers by using exfoliated nanoplatelets have been discussed in the previous chapter.
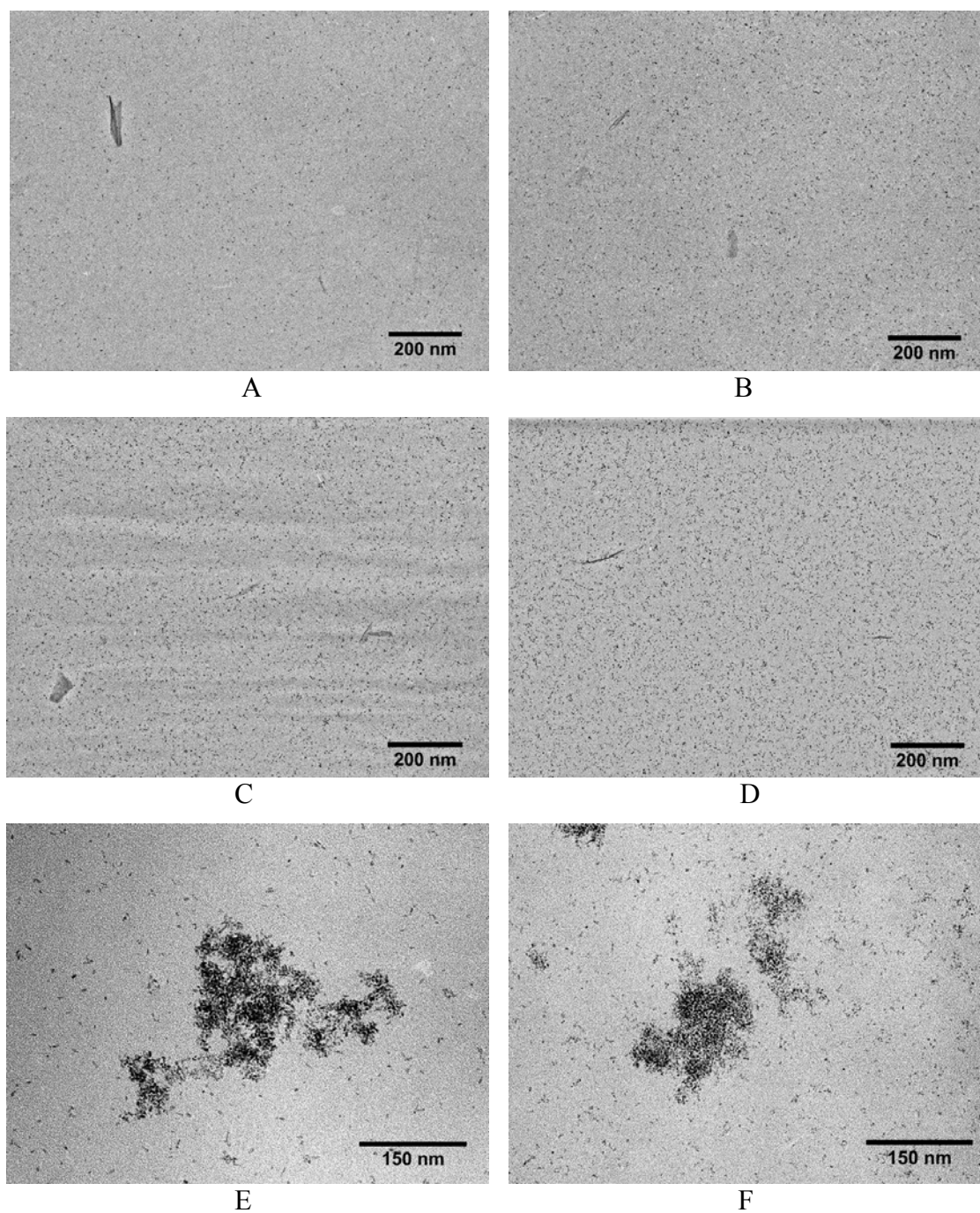
Figure 8.3. HR-TEM images of (A-F) samples **b-g**. In the epoxy hybrid nanocomposites (samples **b-e**), ZnO quantum dots are well dispersed, not aggregated. But in the epoxy/ZnO nanocomposites (samples **f** and **g**), large QD aggregates are seen.

8. 3. 3. Optical Spectra of Monodisperse ZnO QDs in Epoxy

Figure 8.4A shows the UV-vis spectra of samples **a-g** in transmittance mode with wavelengths ranging from 250 to 850 nm. For clarity, the UV-vis spectra of samples **a** and **h** are plotted separately and shown in Figure 8.4B. The transmittance of sample **a** having wavelengths above 300 nm increases with the wavelength and saturates at around 91 % as the wavelength > 600 nm. Sample **h** shows the same UV-vis spectrum as sample **a**, indicating that the incorporation of exfoliated nanoplatelets (0.5 wt. %) does not alter the optical properties of the epoxy matrix.

Transmittance of samples **b-e** at wavelengths longer than 600 nm is similar to that of sample **a**, indicating the good dispersion of ZnO QDs (Figure 8.3) and high transparency (Figure 8.2). Moreover, samples **b-e** show high UV-absorption efficiency at wavelengths between 300 nm and 360 nm. Samples **b-e** also exhibit a sharp UV-vis spectra transmittance onsets, indicating that the epoxy hybrid nanocomposites do not scatter lights to any appreciable extent in the visible range of the spectra. As for the epoxy/ZnO nanocomposites, samples **f** and **g** also exhibit UV absorption at wavelengths below 370 nm. However, they show much less transmittance after the UV absorption than samples **a-e**. The higher the concentration of ZnO QDs in epoxy, the lower transmittance the epoxy/ZnO nanocomposite exhibits, which agrees well with the visual observation shown in Figure 8.2. In addition, unlike samples **a-e**, the transition from UV to visible light range for samples **f** and **g** is broad. This is due to the presence of large QD aggregates, which scatter a substantial amount of lights.
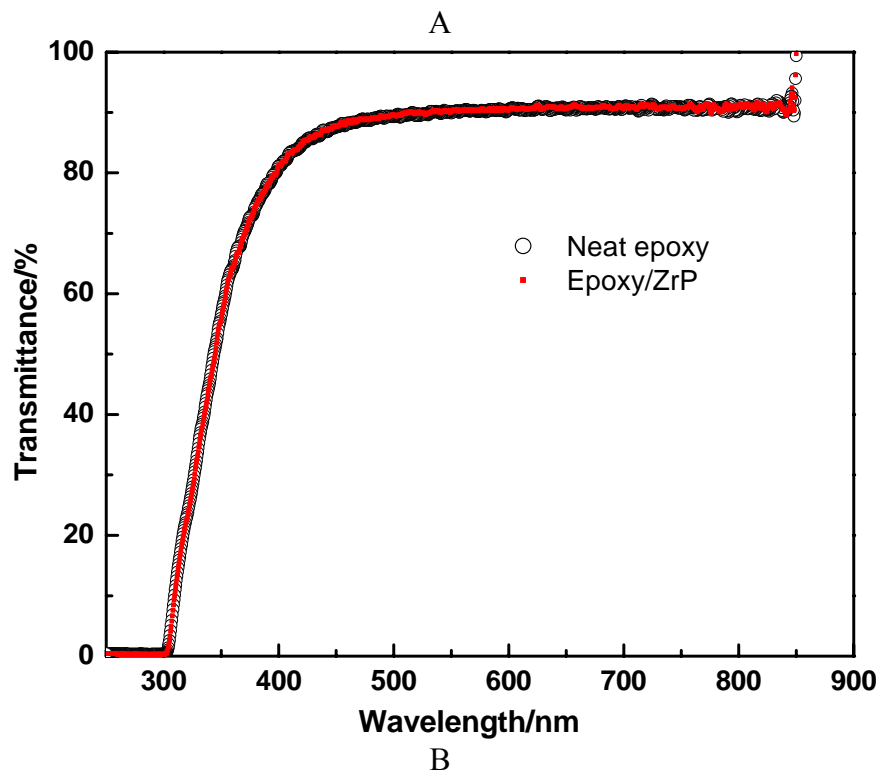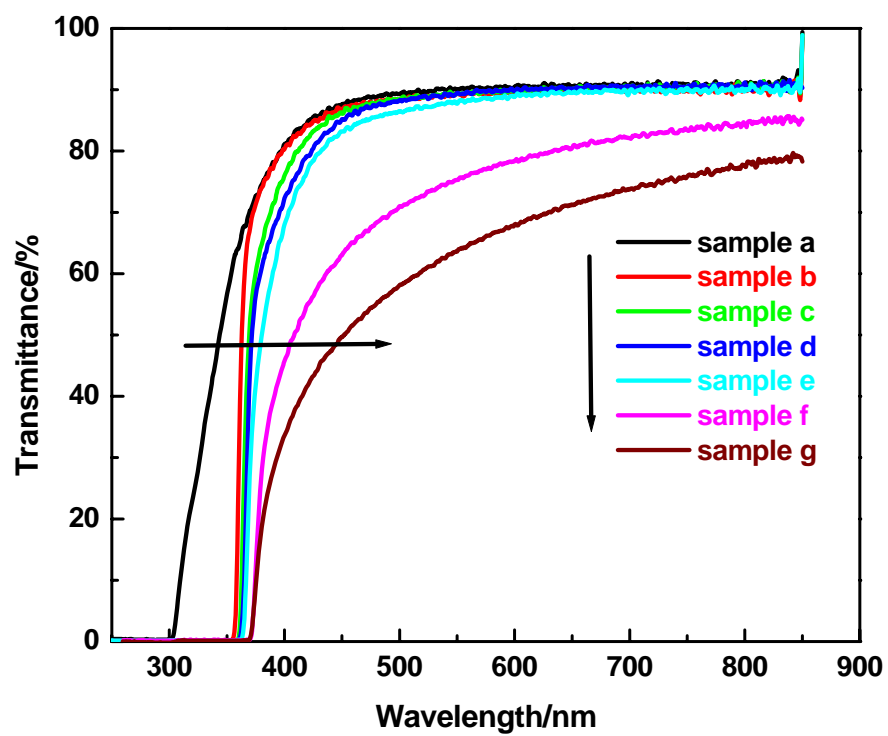
Figure 8.4. UV-vis spectra of (A) samples **a-g** and (B) samples **a** and **h** in the transmittance mode with air as the background.

Interestingly, samples **b-g** also show shifting of the transmittance onsets (Figure 8.4A). The transmittance onsets of samples **b-e** show red-shifting as the ZnO concentration increases. Furthermore, the transmittance onsets of samples **f** and **g** are almost the same, but have been red-shifted compared to those of samples **b-e**. Figure 8.5 shows the UV-vis spectra for samples **b-g** at wavelengths between 330 nm and 400 nm, with the spectrum of sample **h** utilized as the background. A similar shifting of the absorption onsets can also be seen. The absorption onsets of samples **b-g** are determined to be 358.4, 362.5, 366.3, 367.5, 370.7, and 370.8 nm, respectively.
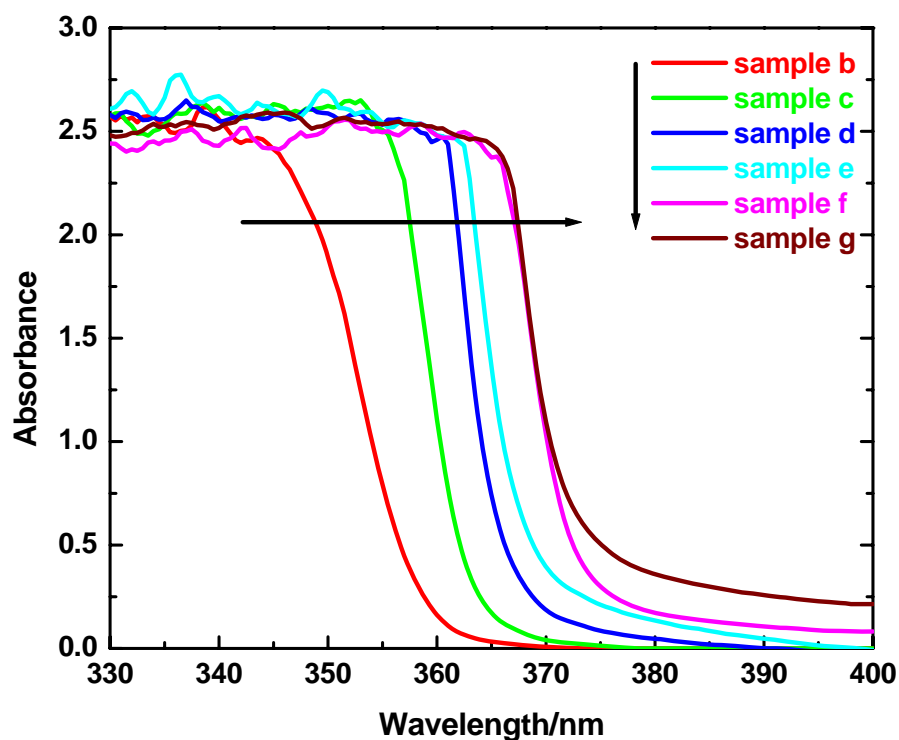
Figure 8.5. UV-vis spectra of samples **b-g** in the absorbance mode with sample **h** as the background.

As shown in Figure 8.4B, the neat epoxy and the epoxy that contains 0.5 wt.% of exfoliated ZrP nanoplatelets (i.e., sample **h**) show identical UV-vis spectra, indicating that the light scattering or absorption from the exfoliated ZrP nanoplatelets in epoxy is negligible. In addition, the optical absorption spectra of the epoxy hybrid nanocomposites (Figure 8.5) were obtained using sample **h** as the background. Therefore, it is evident that the presence of exfoliated ZrP nanoplatelets would not affect our analyses of the optical properties of ZnO QDs in epoxy.

After being incorporated into epoxy with an aid exfoliated ZrP nanoplatelets, the ZnO QDs with a concentration of 0.5 wt.% (sample **b**) show an absorption onset at 358.4 nm (Figure 8.5), corresponding to a bandgap energy of 3.459 eV, which is slightly blue-shifted compared to that of the ZnO QDs in colloids (3.453 eV). This variation may be due to the difference in the medium surrounding the ZnO QDs. Fonoberov and Balandin *[207]* applied a multi-band effective mass model to ZnO QDs and showed that in a medium with higher dielectric constant, ε_{ext}, ZnO QDs show a slightly lower bandgap than in a lower ε_{ext} medium. This phenomenon may be due to the interaction of QDs with different media through dipole-dipole interaction. In our case, methanol has a dielectric constant of 32.66, while a typical epoxy has a dielectric constant of less than 10, which is much smaller than methanol. Therefore, the difference in dielectric constant of the media appears to account for the slight blue-shift of the absorption onset in epoxy compared with that in the colloids.

Figure 8.6 shows the optical photoluminescence spectra of samples **b-g** having an excitation wavelength of 320 nm. All the samples tested show complete UV

emissions from ZnO QDs. The emission peaks of samples **b-e** are 363.9, 370.1, 376.3, and 379.2 nm, respectively, which exhibit red-shifting as ZnO concentration increases. The emission peaks of samples **f** and **g** are around 386.2, and 387.3 nm, which are both similar to that of the bulk ZnO.
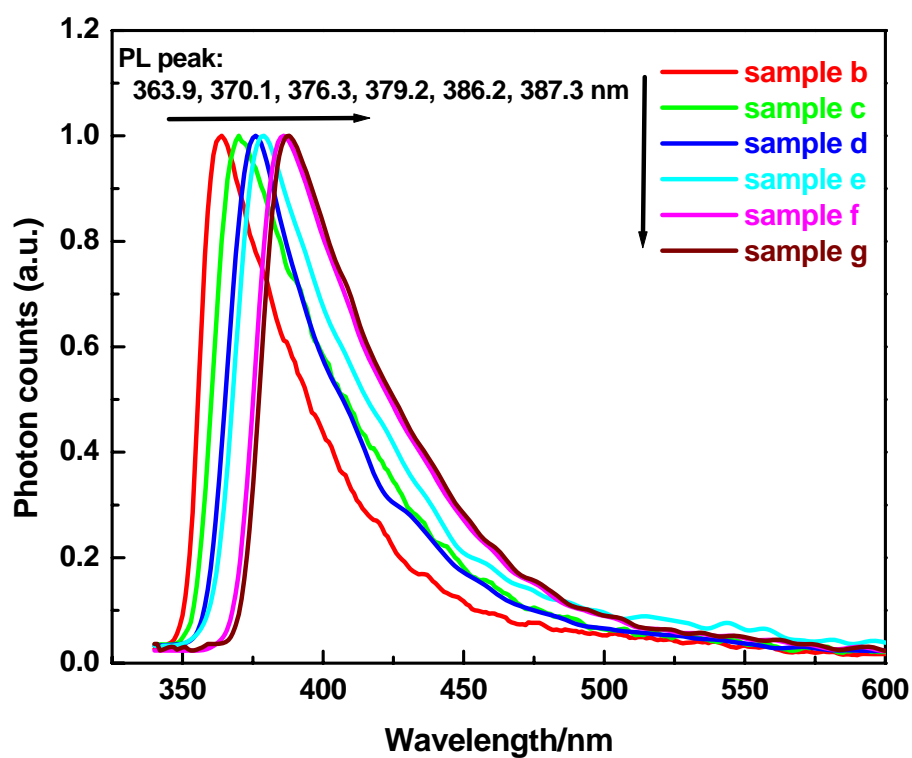
Figure 8.6. Optical photoluminescence spectra of samples **b-g** with an excitation wavelength of 320 nm.

8. 3. 4. Relationship between QD Dispersion and Optical Properties

The observed red-shift of the absorption onset as the QD concentration is increased in the epoxy hybrid nanocomposites (samples **b-e**, Figure 8.5) can be explained by the coupling effect of colloidal QDs when the distance between the particles is reduced. It has been shown that the QD separation in a close-packed QD solid can be tuned by using different organic capping agents. With the inter-dot distances between 5 and 100 Å, electronic energy can be transferred between the neighboring QDs through long-range dipole-dipole resonance (weak coupling). This will lead to red-shifting of photoluminescence, but the optical absorption spectrum remains unchanged. Only when inter-dot spacing is much smaller will significant interactions between adjacent QDs take place through quantum mechanical tunneling to dramatically modify the optical and electronic properties of QDs (strong coupling). This will cause a significant red-shifting of both optical absorption and photoluminescence. When the organic capping agents are removed and the QDs becomes directly in contact with each other, the QD solids would show similar optical properties of the bulk (quenching of the quantum size effects) *[47, 209]*. Similar phenomenon has also been seen in the organic capping agent-free ZnO QD powders obtained by drying the colloids *[183]*. Therefore, based on the above analysis, the optical properties of QDs should be a function of inter-dot distance. This phenomenon is unambiguously demonstrated here in this study in the case of QDs dispersion in polymer matrices.

As shown in Figure 8.3, when the concentration of ZnO QDs in the epoxy hybrid nanocomposites is 0.5 wt. % (sample **b**), the ZnO QDs are individually dispersed in

epoxy and the average inter-dot distance is greater than 20 nm. Based on Figures 8.1 and 8.5, the optical absorption spectra of ZnO QDs at low concentrations do not change before and after dispersion in epoxy, except for the medium effect. Therefore, there is no observable QD coupling effect when 0.5 wt.% of ZnO QDs is well dispersed in epoxy.
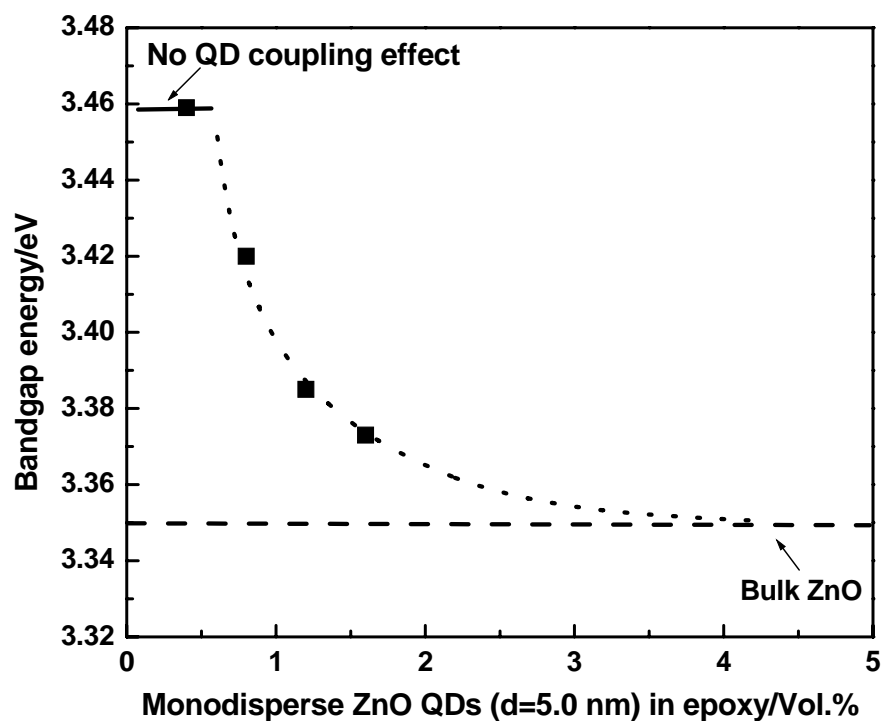
Figure 8.7. The relationship between bandgap energy and the concentration of mono-sized ZnO QDs in epoxy.

However, when the concentration of well dispersed ZnO QDs in epoxy is increased, the inter-dot distance will become closer to each other and red-shifting of the optical absorption onset begins to occur, indicating that strong QD coupling effect takes

place and alters the optical properties of the epoxy hybrid nanocomposites significantly. The bandgap energies of samples **c-e** are 3.420, 3.385, and 3.373 eV, respectively, which correspond to red-shifting of 39, 74, and 86 meV, in reference to sample **b** where no QD coupling effect is present. In Figure 8.7, the bandgap energy of well dispersed ZnO QDs (5.0 nm in diameter) in epoxy as a function of the QD concentration is plotted. A volume percentage is used in this plot to illustrate the packing state of QDs in epoxy. The volume percentages of ZnO QDs in samples **b-e** are estimated to be ~ 0.4, 0.8, 1.2, and 1.6 vol.%, respectively. Also, the bandgap energies of the bulk ZnO and uncoupled ZnO QDs are indicated in Figure 8.7 as a reference. This plot depicts a general tendency for the change of the bandgap energy of monodisperse colloidal QDs well dispersed in polymers with respect to the QD concentration.

Meanwhile, as shown in Figure 8.7, it is surprised to note that a significant decrease in bandgap energy or a strong QD coupling occurs at the concentration of ZnO QDs of around 1 vol.% in epoxy. A simple calculation based on 1 vol.% of 5-nm ZnO QDs in epoxy yields an average QD separation distance of around 15 nm. According to TEM shown in Figure 4, the observed inter-dot distances for 0.8 and 1.2 vol.% of ZnO QDs in epoxy (samples **c** and **d**) are around 20 and 10 nm, respectively. Therefore, the theoretical calculation and experimental finding agree well with each other. This, in turn, helps to demonstrate that our ZnO QDs have been well dispersed in epoxy with the aid of exfoliated nanoplatelets. As already discussed earlier, usually, for a large inter-dot separation, weak quantum coupling occurs in between the organically capped QDs; for a large reduction in bandgap energy to occur, the inter-dot distance is

typically < 5 Å *[47]*. However, in case of our ZnO QDs in epoxy, a strong QD coupling takes place at a relatively large average inter-dot distance of around 10-15 nm. The apparent contradiction between the literature results and the current study may be due to 1) the nature of ZnO QDs prepared or 2) the surrounding medium effect, or both. It has been suggested that in organically capped QD solids, the organic capping agents serve as the media for QDs. Electrons or holes are transferred through the ligands bonded on the surface of QDs at a relatively large inter-dot separation *[209]*. However, in the case of the ZnO QDs used in this study, no organic capping agent is used and the surface is only covered by a small fraction of acetate after purification *[190]*. It is most likely that electrons or holes are transferred directly from dot to dot through the epoxy network. The epoxy in this study was cured based on DGEBA and amine which contain numerous lone pair electrons (i.e., O and N) and conjugated π bondings (i.e., benzene ring). Therefore, these electron-rich groups may facilitate the electronic energy transfer between QDs in epoxy.

When no nanoplatelets are incorporated, the colloidal ZnO QDs without organic capping agents form aggregates in epoxy as shown in the TEM images of samples **f** and **g** (Figure 8.3). In this case, a strong QD coupling effect takes place and the absorption onsets of such samples are expected to be the same as the bulk ZnO. Indeed, according to Figure 8.5, the absorption onsets of samples **f** and **g** (370.7 and 370. 8 nm, respectively) are very close to that of the bulk ZnO (~ 370 nm). Moreover, after the absorption onset, the light-scattering effect in sample **f** is seen to be more significant than that in sample **g**, indicating that the QD aggregation in sample **g** with a high QD

concentration is more significant than that in sample **f** having a low QD concentration. This agrees with the TEM observations shown in Figure 8.3.

As for luminescence, normally, without using organic capping agents, ZnO QDs in colloids exhibit two emissions as shown in Figure 8.8. One is relatively sharp but weak peak in the UV range due to the recombination of electrons and holes at the near band edges. The other is a broad and strong peak as green emission. This visible emission is generally believed to be due to the existence of oxygen vacancies on the ZnO surface *[182]*. By using organic capping agents, such as polyvinyl pyrrolidone, capped ZnO QDs shows quenched green emission and enhanced UV emission due to the surface passivation of the oxygen vacancies *[185]*. Interestingly, after being embedded into epoxy, ZnO QDs also exhibit complete UV-emission even without using organic capping agents. Previously, we have demonstrated that the acetate ions bonded on the surface of ZnO QD powder passivate the oxygen vacancies, leading to the quenched visible emission and enhanced UV emission *[183]*. Therefore, the complete UV-emission from the epoxy nanocomposites containing ZnO QDs seen in this study can also be explained by the existence of acetate ions on the surface of ZnO QDs.

Compared with the PL of ZnO QDs in colloids shown in Figure 8.8, the PL peak of sample **b** is slightly blue-shifted, which may also be due to the medium effect as already discussed earlier. By considering both PL and absorption spectra of sample **b**, it is clear that there is no QD coupling effect when 0.5 wt.% of ZnO QDs are well dispersed in epoxy because both of the spectra have no red-shift in reference to those of ZnO QDs in colloids, except for a small change due to the medium effect. However, as

the concentration of well dispersed ZnO QDs in epoxy increases, the PL peak shows red-shifting, suggesting the occurrence of the QD coupling effect. In the case of samples **f** and **g**, where ZnO QD aggregates are formed, both of the PL peaks are similar to that of the bulk ZnO *[183]*.
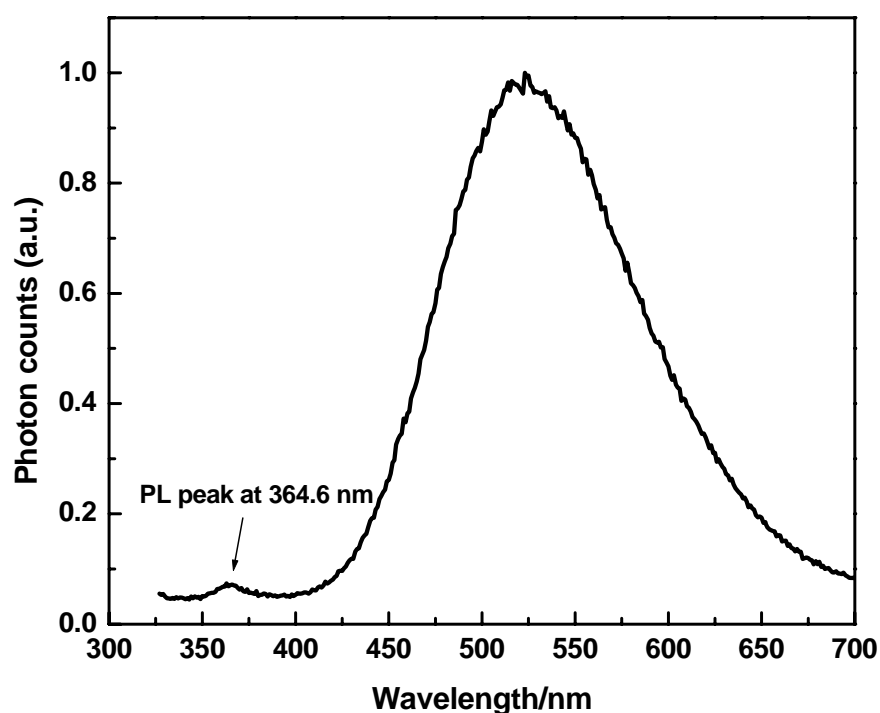
Figure 8.8. Optical photoluminescence spectrum of ZnO QDs in colloids.

Figure 8.9 shows the Stokes shift of the PL peak with respect to the absorption onset in samples **b-e**. The Stokes shifts of no QD coupling effect and QD aggregation (samples **f** and **g**) are also indicated in the plot. This Stokes shift increases as the QD concentration in epoxy increases and a strong QD coupling effect can also be seen at the

QD concentration of lower than 1 vol%. This agrees with the observation from the bandgap reduction shown in Figure 8.7. The Stokes shift from semiconductor nanocrystals is a complex phenomenon and may be dependent of the nanocrystal size and shape *[10, 209]*. However, the origin of the Stokes shift in QDs still remains unclear *[210]*.
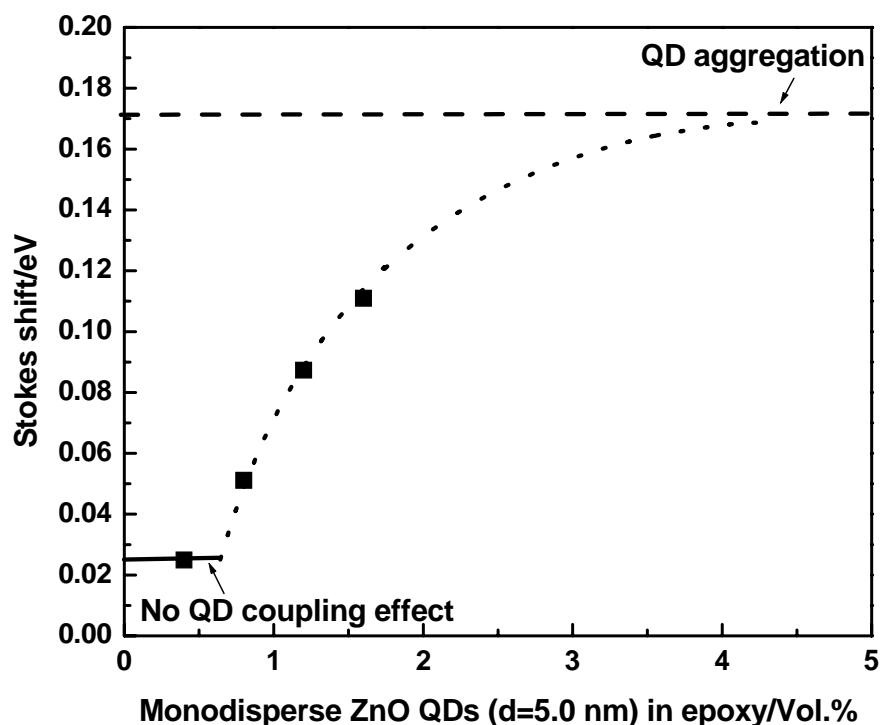
Figure 8.9. The relationship between Stokes shift (the energy between absorption onset and PL peak) and the concentration of monodisperse ZnO QDs in epoxy.

8. 3. 5. Dispersion and Optical Properties of Monodisperse ZnO QDs in PMMA

Figure 8.10 shows the TEM images of PMMA/ZnO nanocomposites and PMMA/ZnO/ZrP nanocomposites with various nanofiller concentrations. Purified ZnO

QDs form large aggregates in PMMA without using ligands or exfoliated nanoplatelets (Figure 8.10A and B) similar to those found in the epoxy/ZnO nanocomposites. However, with the existence of a small amount of exfoliated ZrP nanoplatelets (0.5 wt.%) the size of QD aggregates is dramatically reduced as shown in Figure 8.10C – F. Under a fixed concentration of exfoliated ZrP nanoplatelets at 0.5 wt.%, the QD aggregate size is found to become smaller as the QD concentration decreases (3.0 wt.% to 0.5 wt.%), indicating that the higher the ratio of exfoliated nanoplatelet to QDs, the better QD dispersion can be achieved. Since the PMMA hybrid nanocomposites were also prepared through solution mixing, this phenomenon can be explained by the same mechanism that has been discussed in the last chapter as in the case of epoxy hybrid nanocomposites, that is, the colloidal diffusion of the nanoplatelets alters the interaction of QDs with their surrounding in such a way that QDs becomes thermodynamically stable in colloids.
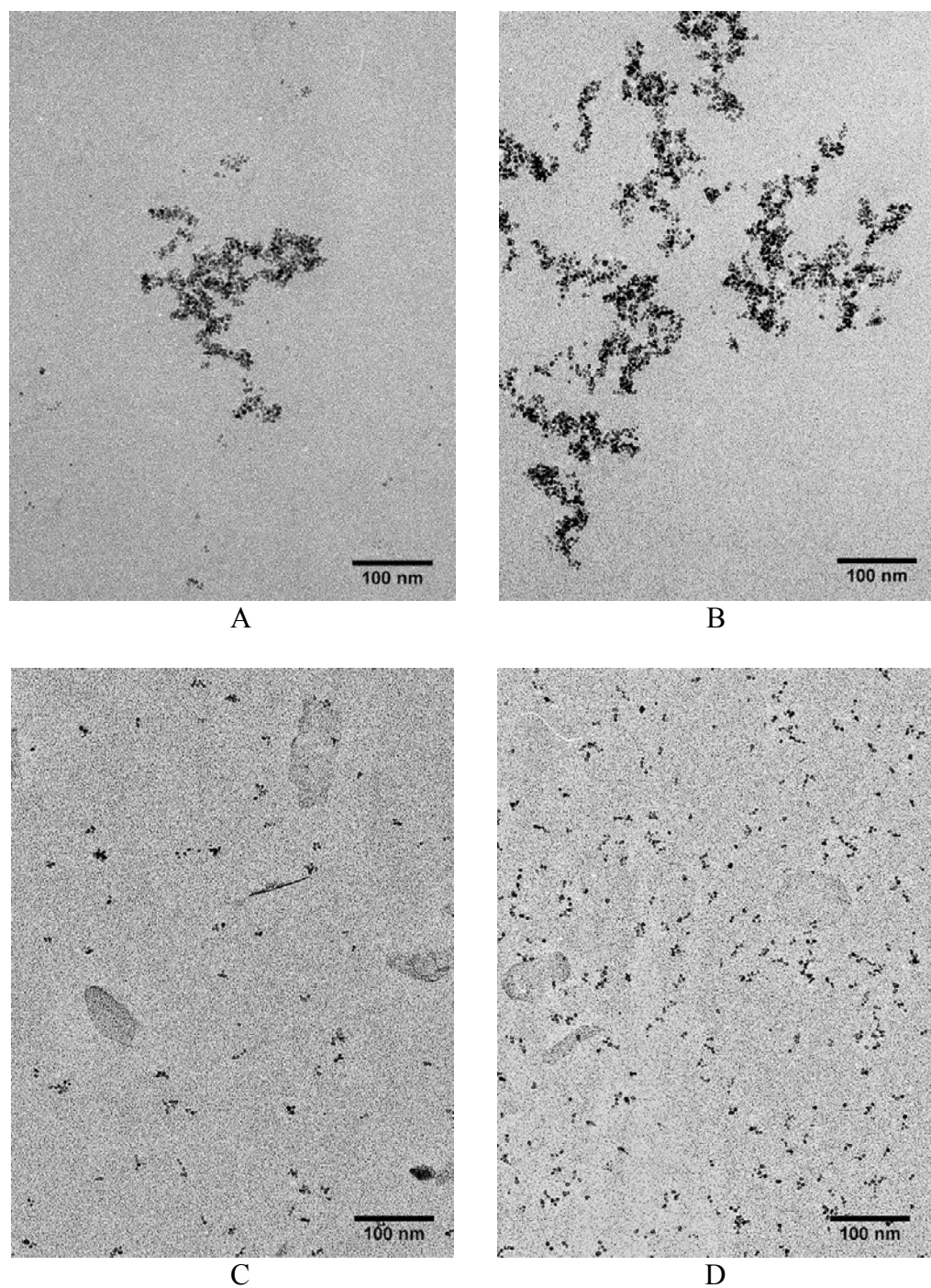
Figure 8.10. TEM images of PMMA/ZnO nanocomposites containing (A) 1.0 wt.% and (B) 2.0 wt.% of ZnO QDs and PMMA/ZnO/ZrP nanocomposites containing 0.5 wt.% of exfoliated ZrP nanoplatelets and (C) 0.5 wt.%, (D), 1.0 wt.%, (E) 2.0 wt.%, and (F) 3.0 wt.% of ZnO QDs.

E

F
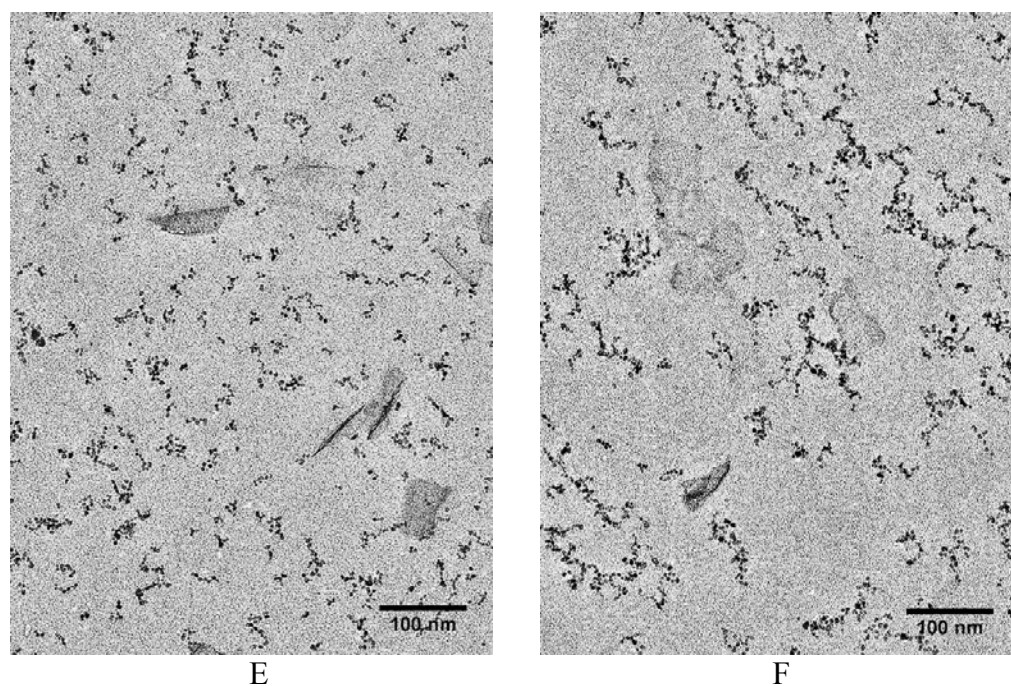
Figure 8.10. Continued.

The UV-vis spectra of the PMMA hybrid nanocomposite films are shown in Figure 8.11. The neat PMMA film is transparent to the UV and visible lights in the range tested. However, the PMMA hybrid nanocomposites absorb UV lights below 360 – 370 nm due to the prestence of ZnO QDs. The higher the concentration of ZnO QDs, the more UV lights the PMMA hybrid nanocomposite films can absorb. Each PMMA hybrid nanocomposite film shows a sharp transition at the absorption onset, indicating a good dispersion of the nanofillers. It can also be observed from the UV-vis spectra that the absorption onset is red-shifted as the QD concentration increases, which is also due to the QD coupling effect discussed in the case of epoxy hybrid nanocomposites earlier. Moreover, at the visible light range, all the PMMA hybrid nanocomposite films show a

similar transparency to the neat PMMA film, which also suggests the good dispersion of the nanofillers. This agrees with the TEM observations shown in Figure 8.10.
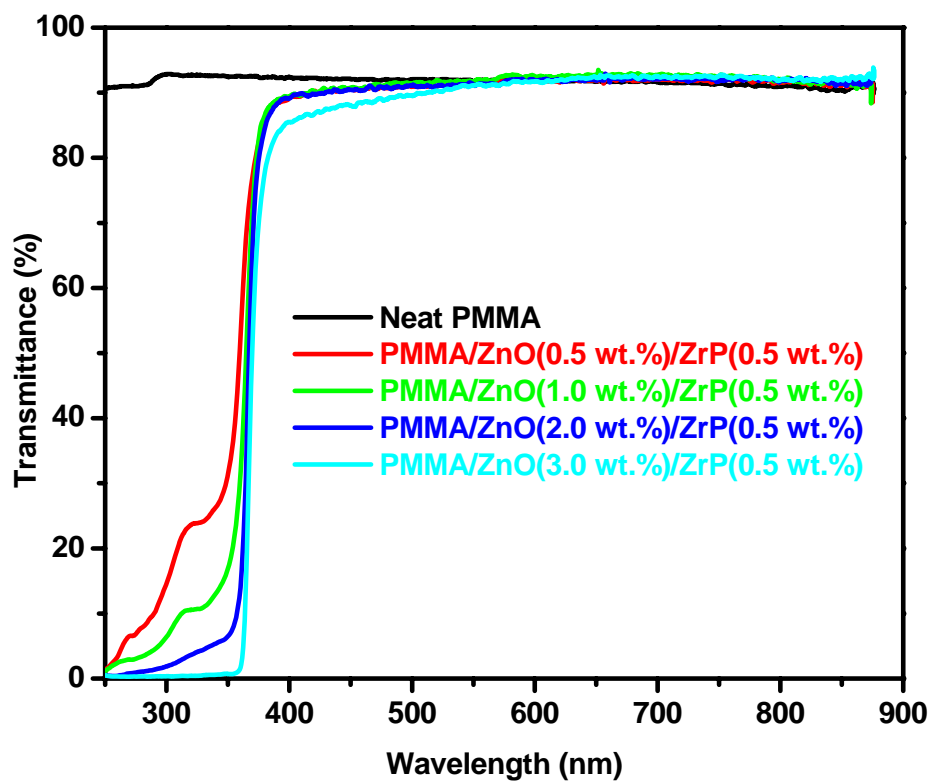
Figure 8.11. UV-vis spectra of the neat PMMA and the PMMA hybrid nanocomposite films. The thickness of all the film samples is around 100 μm.

Figure 8.12 shows the photoluminescence spectra of the PMMA hybrid nanocomposite film and the PMMA/ZnO nanocomposite film. Similar to the epoxy nanocomposites, the emission peaks of the PMMA hybrid nanocomposite films exhibit

red-shifting with the increase of the QD concentration, which can also be explained by the QD coupling effect. The PMMA/ZnO nanocomposite film shows a similar emission as the bulk ZnO at around 390 nm. Moreover, all the film samples show only one UV fluorescence that is the bandgap emission from ZnO QDs, indicating that the surface defects of ZnO QDs have been well passivated in the PMMA films.
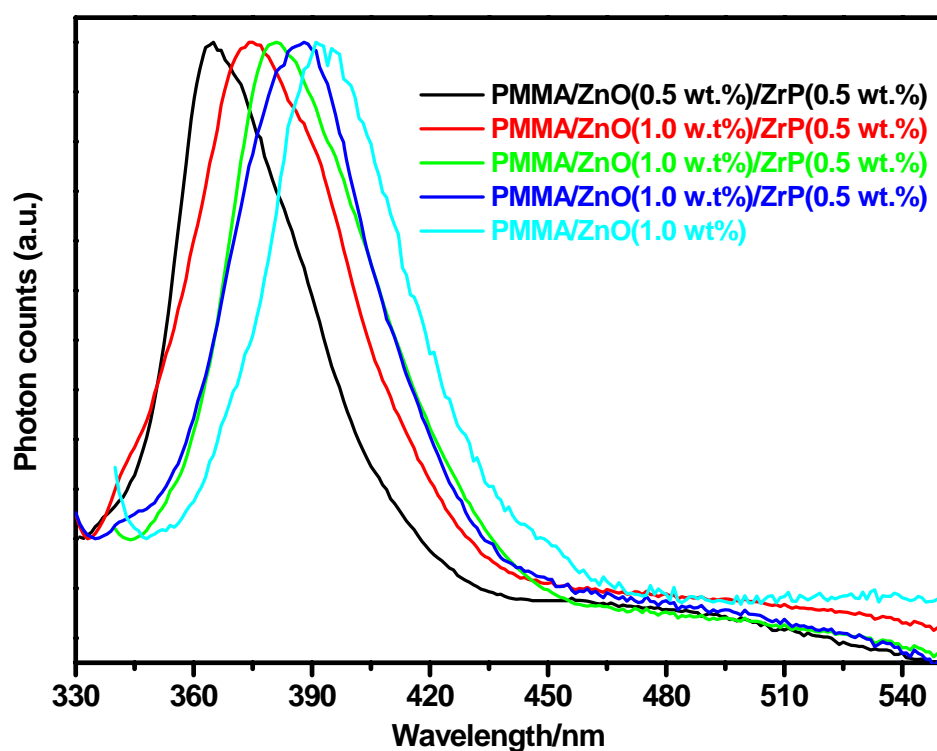
Figure 8.12. Photoluminescence of the PMMA/ZnO/ZrP and PMMA/ZnO nanocomposite films. The thickness of all the film samples is around 100 μm.

8. 4.   Conclusions

Dispersion – optical property relationship in polymer/QD nanocomposites has been systematically investigated based on two polymer-based hybrid nanocomposites with tunable QD dispersion states. The polymer hybrid nanocomposites are highly transparent and show UV-absorption properties. TEM images indicate that ZnO QDs have been individually dispersed in epoxy and in PMMA. The hybrid nanocomposites exhibit strong UV-emission, as well. The red-shifting of the absorption onset and PL peak is observed as the QD concentration increases, indicating a strong QD coupling effect in the polymer matrix. The current study is of particular interest in understanding the mechanisms responsible for the optical property changes in QD-containing polymer nanocomposites, and should help in establishing guidelines for designing polymer/inorganic nanocomposites with desired optical and electronic properties.

CHAPTER IX

CONCLUDING REMARKS AND FUTURE RECOMMENDATIONS

The research efforts in this dissertation include: (**i**) stable dispersion of two representative colloidal nanomaterials – 0-dimensional (0-D) quantum dots (QDs) and 1-dimensional (1-D) carbon nanotubes (CNTs) – in water, organic solvents, and polymers; and (**ii**) self-assembly of 2-dimensional (2-D) colloidal nanoplatelets into liquid crystalline structures and their phase transition study.

A simple and effective nanoplatelet-assisted strategy for controlling dispersion of QD and CNT has been developed and systematically studied. With an aid of exfoliated nanoplatelets, QDs and CNTs can be dispersed down to an individual level in solvents and polymers, and the dispersion level has been found to depend on nanoplatelet-to-QD or nanoplatelet-to-CNT ratios. Special attention has been placed on dispersing QDs and CNTs in polymer matrices to study their structure-property relationship. Physical and mechanical properties of the nanocomposites prepared have been found to depend on the dispersion state of the nanofillers.

Colloidal 2-D nanoplatelets self-assemble into liquid crystalline structures upon increasing their concentrations. By controlling the synthetic condition and exfoliation chemistry, colloidal nanoplatelets with uniform thickness at various aspect ratios have been prepared, and their formation of colloidal liquid crystals has been systematically investigated through optical microscopy (OM), transmission electron microscopy (TEM), and X-ray diffraction (XRD).

9. 1. Dispersion of QDs

Monodisperse ZnO QDs with a diameter of 5.0 nm have been synthesized and purified in methanol through a simple colloidal approach. The purified ZnO QDs are found to be stable in methanol for at least 48 hr upon addition of a small amount of hexane. The purified ZnO QDs can be transferred into water using polyvinyl pyrrolidone (PVP). Dynamic light scattering (DLS) results show that ZnO QDs have been made to be individually dispersed in water for a long period of time (over a year) and the QD aggregate size can be controlled by the amount of PVP utilized.

Exfoliated α-zirconium phosphate (ZrP) nanoplatelets have been utilized to disperse purified ZnO QDs in organic solvents and polymers without using surfactants and ligands. The dispersion state of QDs is tuned from micron-sized aggregates to nanometer-scale clusters and even down to individual level upon increasing the concentration of exfoliated nanoplatelets. The QD dispersion states are characterized through TEM and UV-vis spectroscopy. Experimental observations and analysis suggest that the presence of exfoliated nanoplatelets alters the QD-QD and QD-medium interactions such that the QD dispersion free energy is significantly lowered, thus thermodynamically stable in organic solvents and polymers.

Dispersion – property relationship in polymer/QD nanocomposites has also been systematically studied. The nanoplatelet-assisted QD dispersion approach is used to prepare model nanocomposites with controlled QD dispersions. The optical absorption and emission are found to be red-shifted when the QD concentration is increased in highly dispersed polymer nanocomposites. In case of highly aggregated QDs in

polymers, the optical properties of QDs are similar to the bulk. The dispersion-dependent optical properties of polymer/QD nanocomposites can be explained by the QD coupling effect, namely, the band-gap energy of QDs is decreased when they are getting close to each other such that the photo-excited electrons and holes can tunneling between QDs through the medium.

9. 2.   Debundling and Dispersion of CNTs

Dispersing CNTs, including single-walled CNTs (SWNTs) and multi-walled CNTs (MWNTs) in water, has been performed by utilizing exfoliated ZrP nanoplatelets. Under mild sonication, both types of CNTs can be dispersed down to individual level in a short period of time. The proposed dispersion mechanisms involve a sequence of events: (**a**) bonding between exfoliated nanoplatelets and CNTs through electrostatic attraction; (**b**) gathering and concentrating sonication energy by the 2-D exfoliated nanoplatelets onto the nanotube aggregates and bundles; (**c**) physically pulling off nanotube aggregates, entanglements, and bundles; and (**d**) stabilizing newly dispersed CNTs through attaching onto exfoliated nanoplatelets. Such dispersed CNTs can maintain their stability in water for several months. Since this approach does not involve chemical functionalization of nanotube side-walls, the physical properties such as optical and electrical properties have been preserved. The dispersion and physical properties are characterized through TEM, UV-vis-NIR, and Raman spectroscopy.

By using the above nanoplatelet-assisted CNT dispersion concept, a drying – redispersion approach has been developed to transfer the aqueous dispersion of CNTs into organic solvents. In this matter, highly exfoliated epoxy/CNT nanocomposites can be easily prepared through solution mixing. TEM observations show that both SWNTs and MWNTs can be well dispersed in polymer matrices through this method. Mechanical testing suggests that polymer nanocomposites containing a small amount of well-dispersed CNTs (only 0.4 wt.%) exhibit exceptional modulus and strength improvements without compromising their ductility.

9. 3.   Self-assembly of Colloidal Nanoplatelets

Self-assembly of colloidal nanoplatelets with uniform thickness and various aspect ratios has been systematically investigated by using a set of model nanoplatelet systems. Pristine layered ZrP nanoplatelets with various diameters have been prepared by controlling the synthetic conditions. Through full exfoliation of these pristine ZrP, monolayer platelets with identical thickness are obtained. Upon increasing the volume fraction of these monolayer platelets in aqueous suspensions, an isotropic (I) – nematic (N) transition has been observed. The experimental results suggest that the volume fraction at the I – N transition and the width of the I – N coexisting region depend on the platelet aspect ratio. A higher aspect ratio leads to a lower transition volume fraction and a narrower coexisting region. In addition, the experimental data have been compared with theoretical model and shown promising correlation.

An unusual smectic (S) arrangement of colloidal platelets is also found after the formation of the N phase. The S crystal has features of a layered structure and multiple platelets in each layer, which have been characterized through OM, TEM, and XRD. The aspect ratio effect on the formation of the smectic phase has also been studied. Moreover, some general conditions for the formation of the smectic crystals have been discussed.

9. 4.   Recommendations for Future Work

In order to further verify the generality of the approaches developed and the phenomena observed in this dissertation, the following work is suggested.

9. 4. 1. Nanoplatelet-assisted Dispersion of QDs

A novel approach that utilizes exfoliated nanoplatelets to disperse ligand-free QDs has been experimentally investigated. Dynamic analysis on the dispersion mechanisms suggests that the presence of nanoplatelets alters the free energy of QD mixing in organic solvents and polymers in such a way that QDs can interact favorably with the media to achieve a thermodynamically stable dispersion, which depends on the ratio between nanoplatelets and QDs. However, a detailed explanation on how the nanoplatelets change the QD-QD and QD-media interactions need to be addressed through computer simulation. Moreover, simulations may help establish generalized criteria for achieving stable QD dispersion using nanoplatelets.

In terms of experimental efforts, the nanoplatelet effect on the QD aggregation rates should be performed to investigate if there is any kinetic factor involved in the

nanoplatelet-assisted dispersion mechanisms. In addition, other combinations of nanoplatelets and QDs may also be carried out to verify if this dispersion approach is general to all cases.

9. 4. 2. Dispersion of CNTs Using Nanoplatelets

The nanoplatelet-assisted CNT dispersion approach introduced in **Chapter IV** may have a tremendous impact on the large-scale application of CNTs because this method can fully debundle and disperse CNTs into individual level with minimal side-wall damages. In the current study, a model platelet system – ZrP nanoplatelets – has been used to investigate the dispersion capability and mechanisms. However, ZrP is a synthetic compound, which is relatively expensive. In order to meet the industrial interests, cheaper inorganic platelets are suggested, such as natural clay. A systematic study on the CNT dispersion using clay should be carried out. Many factors such as types of clay, exfoliation mechanisms, as well as solution pH, ionic strength, etc., should be addressed.

9. 4. 3. Self-assembly and Phase Transition of Colloidal Platelets

A model colloidal 2-D platelet system has been introduced using exfoliated ZrP nanoplatelets with uniform thickness and various aspect ratios. These platelets self-assemble into colloidal liquid crystals upon increasing concentrations and their phase behaviors have been systematically studied. However, another important factor – the

diameter polydispersity – has not been fully explored. In order to verify many theories, uniform platelets should be prepared.

Another important phenomenon observed in the current study is the formation of the smectic phase. This phase is unique because it has not been experimentally seen in both disk-like molecular liquid crystals and plate-like colloidal liquid crystals. In **Chapter III**, some possible conditions for the smectic phase formation based on experimental results have been discussed. However, simulations should be performed to validate these proposed criteria and understand the smectic phase transition. Moreover, colloidal systems have been increasingly utilized to study many atomic and molecular phenomena. It is highly recommended to design experiments using disk-like molecules or supermolecules based on the current results to obtain the smectic phase of molecular liquid crystals.

REFERENCES

[1]   L. E. Brus, *Journal of Chemical Physics* **1984**, *80*, 4403.

[2]   L. Brus, *Journal of Physical Chemistry* **1986**, *90*, 2555.

[3]   L. Spanhel, A. Henglein, H. Weller, *Berichte Der Bunsen-Gesellschaft-Physical Chemistry Chemical Physics* **1987**, *91*, 1359.

[4]   A. P. Alivisatos, *Science* **1996**, *271*, 933.

[5]   M. P. Pileni, *Accounts of Chemical Research* **2008**, *41*, 1799.

[6]   A. L. Efros, M. Rosen, *Annual Review of Materials Science* **2000**, *30*, 475.

[7]   L. Spanhel, M. A. Anderson, *Journal of the American Chemical Society* **1991**, *113*, 2826.

[8]   C. B. Murray, D. J. Norris, M. G. Bawendi, *Journal of the American Chemical Society* **1993**, *115*, 8706.

[9]   L. Manna, E. C. Scher, A. P. Alivisatos, *Journal of the American Chemical Society* **2000**, *122*, 12700.

[10]   X. G. Peng, L. Manna, W. D. Yang, J. Wickham, E. Scher, A. Kadavanich, A. P. Alivisatos, *Nature* **2000**, *404*, 59.

[11]   C. Pacholski, A. Kornowski, H. Weller, *Angewandte Chemie-International Edition* **2002**, *41*, 1188.

[12]   L. Manna, D. J. Milliron, A. Meisel, E. C. Scher, A. P. Alivisatos, *Nature Materials* **2003**, *2*, 382.

[13]   E. C. Scher, L. Manna, A. P. Alivisatos, *Philosophical Transactions of the Royal Society of London Series a-Mathematical Physical and Engineering Sciences* **2003**, *361*, 241.

[14]   Y. N. Xia, P. D. Yang, Y. G. Sun, Y. Y. Wu, B. Mayers, B. Gates, Y. D. Yin, F. Kim, Y. Q. Yan, *Advanced Materials* **2003**, *15*, 353.

[15]   A. G. Kanaras, C. Sonnichsen, H. T. Liu, A. P. Alivisatos, *Nano Letters* **2005**, *5*, 2164.

[16]   Y. Narukawa, Y. Kawakami, M. Funato, S. Fujita, S. Fujita, S. Nakamura, *Applied Physics Letters* **1997**, *70*, 981.

[17]   W. U. Huynh, X. G. Peng, A. P. Alivisatos, *Advanced Materials* **1999**, *11*, 923.

[18]   J. Lee, V. C. Sundar, J. R. Heine, M. G. Bawendi, K. F. Jensen, *Advanced Materials* **2000**, *12*, 1102.

[19]   A. D. Yoffe, *Advances in Physics* **2001**, *50*, 1.

[20]   S. Coe, W. K. Woo, M. Bawendi, V. Bulovic, *Nature* **2002**, *420*, 800.

[21]   W. U. Huynh, J. J. Dittmer, A. P. Alivisatos, *Science* **2002**, *295*, 2425.

[22]   W. J. E. Beek, M. M. Wienk, R. A. J. Janssen, *Advanced Materials* **2004**, *16*, 1009.

[23]   V. C. Sundar, H. J. Eisler, T. Deng, Y. T. Chan, E. L. Thomas, M. G. Bawendi, *Advanced Materials* **2004**, *16*, 2137.

[24]   W. J. E. Beek, M. M. Wienk, R. A. J. Janssen, *Advanced Functional Materials* **2006**, *16*, 1112.

[25] I. Gur, N. A. Fromer, C. P. Chen, A. G. Kanaras, A. P. Alivisatos, *Nano Letters* **2007**, *7*, 409.

[26] M. C. LeMieux, M. Roberts, S. Barman, Y. W. Jin, J. M. Kim, Z. N. Bao, *Science* **2008**, *321*, 101.

[27] D. L. Klein, R. Roth, A. K. L. Lim, A. P. Alivisatos, P. L. McEuen, *Nature* **1997**, *389*, 699.

[28] A. P. Alivisatos, *Journal of Physical Chemistry* **1996**, *100*, 13226.

[29] D. W. Bahnemann, J. Kern, C. Kormann, M. R. Hoffmann, *Abstracts of Papers of the American Chemical Society* **1987**, *193*, 23.

[30] L. Brus, *Ieee Journal of Quantum Electronics* **1986**, *22*, 1909.

[31] L. Brus, *Applied Physics a-Materials Science & Processing* **1991**, *53*, 465.

[32] M. Haase, H. Weller, A. Henglein, *Journal of Physical Chemistry* **1988**, *92*, 482.

[33] C. R. Kagan, C. B. Murray, M. G. Bawendi, *Physical Review B* **1996**, *54*, 8633.

[34] C. R. Kagan, C. B. Murray, M. Nirmal, M. G. Bawendi, *Physical Review Letters* **1996**, *76*, 1517.

[35] D. J. Norris, M. G. Bawendi, *Physical Review B* **1996**, *53*, 16338.

[36] D. J. Norris, A. L. Efros, M. Rosen, M. G. Bawendi, *Physical Review B* **1996**, *53*, 16347.

[37] L. Spanhel, H. Weller, A. Henglein, *Journal of the American Chemical Society* **1987**, *109*, 6632.

[38] Y. Wang, N. Herron, *Journal of Physical Chemistry* **1991**, *95*, 525.

[39] S. A. Empedocles, M. G. Bawendi, *Science* **1997**, *278*, 2114.

[40]   A. P. Alivisatos, W. W. Gu, C. Larabell, *Annual Review of Biomedical Engineering* **2005**, *7*, 55.

[41]   X. H. Gao, Y. Y. Cui, R. M. Levenson, L. W. K. Chung, S. M. Nie, *Nature Biotechnology* **2004**, *22*, 969.

[42]   D. Bimberg, N. N. Ledentsov, J. A. Lott, *Mrs Bulletin* **2002**, *27*, 531.

[43]   D. C. Look, *Materials Science and Engineering B-Solid State Materials for Advanced Technology* **2001**, *80*, 383.

[44]   X. G. Peng, J. Wickham, A. P. Alivisatos, *Journal of the American Chemical Society* **1998**, *120*, 5343.

[45]   Y. Yin, A. P. Alivisatos, *Nature* **2005**, *437*, 664.

[46]   C. B. Murray, C. R. Kagan, M. G. Bawendi, *Science* **1995**, *270*, 1335.

[47]   C. B. Murray, C. R. Kagan, M. G. Bawendi, *Annual Review of Materials Science* **2000**, *30*, 545.

[48]   P. Alivisatos, *Nature Biotechnology* **2004**, *22*, 47.

[49]   W. C. W. Chan, S. M. Nie, *Science* **1998**, *281*, 2016.

[50]   X. Michalet, F. F. Pinaud, L. A. Bentolila, J. M. Tsay, S. Doose, J. J. Li, G. Sundaresan, A. M. Wu, S. S. Gambhir, S. Weiss, *Science* **2005**, *307*, 538.

[51]   G. Kickelbick, *Progress in Polymer Science* **2003**, *28*, 83.

[52]   P. M. Ajayan, J. M. Tour, *Nature* **2007**, *447*, 1066.

[53]   R. H. Baughman, A. A. Zakhidov, W. A. de Heer, *Science* **2002**, *297*, 787.

[54]   S. Berber, Y. K. Kwon, D. Tomanek, *Physical Review Letters* **2000**, *84*, 4613.

[55] H. J. Dai, J. H. Hafner, A. G. Rinzler, D. T. Colbert, R. E. Smalley, *Nature* **1996**, *384*, 147.

[56] H. J. Dai, E. W. Wong, C. M. Lieber, *Science* **1996**, *272*, 523.

[57] A. C. Dillon, K. M. Jones, T. A. Bekkedahl, C. H. Kiang, D. S. Bethune, M. J. Heben, *Nature* **1997**, *386*, 377.

[58] S. Frank, P. Poncharal, Z. L. Wang, W. A. de Heer, *Science* **1998**, *280*, 1744.

[59] J. Kong, N. R. Franklin, C. W. Zhou, M. G. Chapline, S. Peng, K. J. Cho, H. J. Dai, *Science* **2000**, *287*, 622.

[60] C. Liu, Y. Y. Fan, M. Liu, H. T. Cong, H. M. Cheng, M. S. Dresselhaus, *Science* **1999**, *286*, 1127.

[61] P. Poncharal, Z. L. Wang, D. Ugarte, W. A. de Heer, *Science* **1999**, *283*, 1513.

[62] C. Rutherglen, P. Burke, *Nano Letters* **2007**, *7*, 3296.

[63] R. Saito, G. Dresselhaus, M. S. Dresselhaus, *Physical properties of carbon nanotubes*, Imperial College Press, London **1998**.

[64] S. J. Tans, M. H. Devoret, H. J. Dai, A. Thess, R. E. Smalley, L. J. Geerligs, C. Dekker, *Nature* **1997**, *386*, 474.

[65] A. Thess, R. Lee, P. Nikolaev, H. J. Dai, P. Petit, J. Robert, C. H. Xu, Y. H. Lee, S. G. Kim, A. G. Rinzler, D. T. Colbert, G. E. Scuseria, D. Tomanek, J. E. Fischer, R. E. Smalley, *Science* **1996**, *273*, 483.

[66] E. W. Wong, P. E. Sheehan, C. M. Lieber, *Science* **1997**, *277*, 1971.

[67] Y. Saito, M. Okuda, M. Tomita, T. Hayashi, *Chemical Physics Letters* **1995**, *236*, 419.

[68]   D. S. Bethune, C. H. Kiang, M. S. Devries, G. Gorman, R. Savoy, J. Vazquez, R. Beyers, *Nature* **1993**, *363*, 605.

[69]   M. Terrones, *Annual Review of Materials Research* **2003**, *33*, 419.

[70]   C. P. Deck, K. Vecchio, *Carbon* **2005**, *43*, 2608.

[71]   J. Liu, A. G. Rinzler, H. J. Dai, J. H. Hafner, R. K. Bradley, P. J. Boul, A. Lu, T. Iverson, K. Shelimov, C. B. Huffman, F. Rodriguez-Macias, Y. S. Shon, T. R. Lee, D. T. Colbert, R. E. Smalley, *Science* **1998**, *280*, 1253.

[72]   V. C. Moore, M. S. Strano, E. H. Haroz, R. H. Hauge, R. E. Smalley, J. Schmidt, Y. Talmon, *Nano Letters* **2003**, *3*, 1379.

[73]   J. L. Bahr, J. M. Tour, *Journal of Materials Chemistry* **2002**, *12*, 1952.

[74]   S. Banerjee, T. Hemraj-Benny, S. S. Wong, *Advanced Materials* **2005**, *17*, 17.

[75]   A. Clearfield, *Current Opinion in Solid State & Materials Science* **1996**, *1*, 268.

[76]   A. Clearfield, *Current Opinion in Solid State & Materials Science* **2002**, *6*, 495.

[77]   J. C. P. Gabriel, P. Davidson, *Colloid Chemistry 1* **2003**, *226*, 119.

[78]   G. J. Vroege, H. N. W. Lekkerkerker, *Reports on Progress in Physics* **1992**, *55*, 1241.

[79]   F. M. van der Kooij, H. N. W. Lekkerkerker, *Journal of Physical Chemistry B* **1998**, *102*, 7829.

[80]   T. Pellegrino, L. Manna, S. Kudera, T. Liedl, D. Koktysh, A. L. Rogach, S. Keller, J. Radler, G. Natile, W. J. Parak, *Nano Letters* **2004**, *4*, 703.

[81]   B. Dubertret, P. Skourides, D. J. Norris, V. Noireaux, A. H. Brivanlou, A. Libchaber, *Science* **2002**, *298*, 1759.

[82]   S. Pathak, S. K. Choi, N. Arnheim, M. E. Thompson, *Journal of the American Chemical Society* **2001**, *123*, 4103.

[83]   H. Mattoussi, J. M. Mauro, E. R. Goldman, G. P. Anderson, V. C. Sundar, F. V. Mikulec, M. G. Bawendi, *Journal of the American Chemical Society* **2000**, *122*, 12142.

[84]   S. W. Kim, S. Kim, J. B. Tracy, A. Jasanoff, M. G. Bawendi, *Journal of the American Chemical Society* **2005**, *127*, 4556.

[85]   W. Z. Guo, J. J. Li, Y. A. Wang, X. G. Peng, *Chemistry of Materials* **2003**, *15*, 3125.

[86]   F. Pinaud, D. King, H. P. Moore, S. Weiss, *Journal of the American Chemical Society* **2004**, *126*, 6115.

[87]   W. C. Sheng, S. Kim, J. Lee, S. W. Kim, K. Jensen, M. G. Bawendi, *Langmuir* **2006**, *22*, 3782.

[88]   J. B. Hooper, K. S. Schweizer, *Macromolecules* **2006**, *39*, 5133.

[89]   D. Sun, N. Miyatake, H. J. Sue, *Nanotechnology* **2007**, *18*, 215606.

[90]   M. M. Demir, M. Memesa, P. Castignolles, G. Wegner, *Macromolecular Rapid Communications* **2006**, *27*, 763.

[91]   Y. Q. Li, S. Y. Fu, Y. W. Mai, *Polymer* **2006**, *47*, 2127.

[92]   V. Khrenov, M. Klapper, M. Koch, K. Mullen, *Macromolecular Chemistry and Physics* **2005**, *206*, 95.

[93]   M. M. Demir, K. Koynov, U. Akbey, C. Bubeck, I. Park, I. Lieberwirth, G. Wegner, *Macromolecules* **2007**, *40*, 1089.

[94]   M. M. Demir, P. Castignolles, U. Akbey, G. Wegner, *Macromolecules* **2007**, *40*, 4190.

[95]   H. Althues, R. Palkovits, A. Rumplecker, P. Simon, W. Sigle, M. Bredol, U. Kynast, S. Kaskel, *Chemistry of Materials* **2006**, *18*, 1068.

[96]   M. Abdullah, I. W. Lenggoro, K. Okuyama, F. G. Shi, *Journal of Physical Chemistry B* **2003**, *107*, 1957.

[97]   M. Abdullah, T. Morimoto, K. Okuyama, *Advanced Functional Materials* **2003**, *13*, 800.

[98]   W. U. Huynh, J. J. Dittmer, W. C. Libby, G. L. Whiting, A. P. Alivisatos, *Advanced Functional Materials* **2003**, *13*, 73.

[99]   X. W. Du, Y. S. Fu, J. Sun, X. Han, J. Liu, *Semiconductor Science and Technology* **2006**, *21*, 1202.

[100]   H. M. Xiong, X. Zhao, J. S. Chen, *Journal of Physical Chemistry B* **2001**, *105*, 10169.

[101]   M. J. O'Connell, S. M. Bachilo, C. B. Huffman, V. C. Moore, M. S. Strano, E. H. Haroz, K. L. Rialon, P. J. Boul, W. H. Noon, C. Kittrell, J. P. Ma, R. H. Hauge, R. B. Weisman, R. E. Smalley, *Science* **2002**, *297*, 593.

[102]   M. S. Strano, V. C. Moore, M. K. Miller, M. J. Allen, E. H. Haroz, C. Kittrell, R. H. Hauge, R. E. Smalley, *Journal of Nanoscience and Nanotechnology* **2003**, *3*, 81.

[103] M. J. O'Connell, P. Boul, L. M. Ericson, C. Huffman, Y. H. Wang, E. Haroz, C. Kuper, J. Tour, K. D. Ausman, R. E. Smalley, *Chemical Physics Letters* **2001**, *342*, 265.

[104] A. A. Mamedov, N. A. Kotov, M. Prato, D. M. Guldi, J. P. Wicksted, A. Hirsch, *Nature Materials* **2002**, *1*, 190.

[105] M. Zheng, A. Jagota, E. D. Semke, B. A. Diner, R. S. Mclean, S. R. Lustig, R. E. Richardson, N. G. Tassi, *Nature Materials* **2003**, *2*, 338.

[106] F. Liang, J. M. Beach, P. K. Rai, W. H. Guo, R. H. Hauge, M. Pasquali, R. E. Smalley, W. E. Billups, *Chemistry of Materials* **2006**, *18*, 1520.

[107] Y. Maeda, S. Kimura, Y. Hirashima, M. Kanda, Y. F. Lian, T. Wakahara, T. Akasaka, T. Hasegawa, H. Tokumoto, T. Shimizu, H. Kataura, Y. Miyauchi, S. Maruyama, K. Kobayashi, S. Nagase, *Journal of Physical Chemistry B* **2004**, *108*, 18395.

[108] S. Giordani, S. D. Bergin, V. Nicolosi, S. Lebedkin, M. M. Kappes, W. J. Blau, J. N. Coleman, *Journal of Physical Chemistry B* **2006**, *110*, 15708.

[109] J. H. Rouse, *Langmuir* **2005**, *21*, 1055.

[110] J. Chen, M. A. Hamon, H. Hu, Y. S. Chen, A. M. Rao, P. C. Eklund, R. C. Haddon, *Science* **1998**, *282*, 95.

[111] A. Hirsch, *Angewandte Chemie-International Edition* **2002**, *41*, 1853.

[112] Y. P. Sun, K. F. Fu, Y. Lin, W. J. Huang, *Accounts of Chemical Research* **2002**, *35*, 1096.

[113] V. Georgakilas, K. Kordatos, M. Prato, D. M. Guldi, M. Holzinger, A. Hirsch, *Journal of the American Chemical Society* **2002**, *124*, 760.

[114] E. T. Mickelson, C. B. Huffman, A. G. Rinzler, R. E. Smalley, R. H. Hauge, J. L. Margrave, *Chemical Physics Letters* **1998**, *296*, 188.

[115] R. K. Saini, I. W. Chiang, H. Q. Peng, R. E. Smalley, W. E. Billups, R. H. Hauge, J. L. Margrave, *Journal of the American Chemical Society* **2003**, *125*, 3617.

[116] E. T. Thostenson, Z. F. Ren, T. W. Chou, *Composites Science and Technology* **2001**, *61*, 1899.

[117] T. X. Liu, I. Y. Phang, L. Shen, S. Y. Chow, W. D. Zhang, *Macromolecules* **2004**, *37*, 7214.

[118] A. R. Bhattacharyya, T. V. Sreekumar, T. Liu, S. Kumar, L. M. Ericson, R. H. Hauge, R. E. Smalley, *Polymer* **2003**, *44*, 2373.

[119] E. J. Siochi, D. C. Working, C. Park, P. T. Lillehei, J. H. Rouse, C. C. Topping, A. R. Bhattacharyya, S. Kumar, *Composites Part B-Engineering* **2004**, *35*, 439.

[120] X. F. Zhang, T. Liu, T. V. Sreekumar, S. Kumar, V. C. Moore, R. H. Hauge, R. E. Smalley, *Nano Letters* **2003**, *3*, 1285.

[121] C. A. Mitchell, R. Krishnamoorti, *Macromolecules* **2007**, *40*, 1538.

[122] J. Zhu, H. Q. Peng, F. Rodriguez-Macias, J. L. Margrave, V. N. Khabashesku, A. M. Imam, K. Lozano, E. V. Barrera, *Advanced Functional Materials* **2004**, *14*, 643.

[123] F. Dalmas, L. Chazeau, C. Gauthier, K. Masenelli-Varlot, R. Dendievel, J. Y. Cavaille, L. Forro, *Journal of Polymer Science Part B-Polymer Physics* **2005**, *43*, 1186.

[124] L. M. Clayton, A. K. Sikder, A. Kumar, M. Cinke, M. Meyyappan, T. G. Gerasimov, J. P. Harmon, *Advanced Functional Materials* **2005**, *15*, 101.

[125] M. Moniruzzaman, J. Chattopadhyay, W. E. Billups, K. I. Winey, *Nano Letters* **2007**, *7*, 1178.

[126] J. Zhu, J. D. Kim, H. Q. Peng, J. L. Margrave, V. N. Khabashesku, E. V. Barrera, *Nano Letters* **2003**, *3*, 1107.

[127] P. G. d. Gennes, J. Prost, *The physics of liquid crystals*, Clarendon Press, Oxford University Press, Oxford, New York **1993**.

[128] F. M. van der Kooij, K. Kassapidou, H. N. W. Lekkerkerker, *Nature* **2000**, *406*, 868.

[129] I. Langmuir, *Journal of Chemical Physics* **1938**, *6*, 873.

[130] J. A. C. Veerman, D. Frenkel, *Physical Review A* **1992**, *45*, 5632.

[131] M. A. Bates, D. Frenkel, *Journal of Chemical Physics* **1998**, *109*, 6193.

[132] M. A. Bates, D. Frenkel, *Journal of Chemical Physics* **1999**, *110*, 6553.

[133] W. Strepp, S. Sengupta, A. Lohrer, P. Nielaba, *Computer Physics Communications* **2002**, *147*, 370.

[134] W. Strepp, S. Sengupta, P. Nielaba, *Physical Review E* **2001**, *63,* 046106.

[135] H. H. Wensink, G. J. Vroege, *Physical Review E* **2002**, *65,* 031716.

[136] A. B. D. Brown, S. M. Clarke, A. R. Rennie, *Langmuir* **1998**, *14*, 3129.

[137] J. Zhang, L. Y. Luan, W. X. Zhu, S. Y. Liu, D. J. Sun, *Langmuir* **2007**, *23*, 5331.

[138] J. C. P. Gabriel, F. Camerel, B. J. Lemaire, H. Desvaux, P. Davidson, P. Batail, *Nature* **2001**, *413*, 504.

[139] N. Wang, S. Y. Liu, J. Zhang, Z. H. Wu, J. Chen, D. J. Sun, *Soft Matter* **2005**, *1*, 428.

[140] H. N. Kim, S. W. Keller, T. E. Mallouk, J. Schmitt, G. Decher, *Chemistry of Materials* **1997**, *9*, 1414.

[141] L. Y. Sun, W. J. Boo, D. H. Sun, A. Clearfield, H. J. Sue, *Chemistry of Materials* **2007**, *19*, 1749.

[142] K. Suzuki, M. Yamaguchi, M. Kumagai, S. Yanagida, *Chemistry Letters* **2003**, *32*, 28.

[143] L. A. Girifalco, M. Hodak, R. S. Lee, *Physical Review B* **2000**, *62*, 13104.

[144] K. Esumi, T. Fujii, T. Hosokawa, H. Honda, *Carbon* **1998**, *36*, 470.

[145] K. J. Ziegler, Z. N. Gu, H. Q. Peng, E. L. Flor, R. H. Hauge, R. E. Smalley, *J. Am. Chem. Soc.* **2005**, *127*, 1541.

[146] T. J. Mason, J. P. Lorimer, *Sonochemistry: Theory, applications and uses of ultrasound in chemistry*, John Wiley & Sons, New York **1988**.

[147] F. Hennrich, R. Krupke, S. Lebedkin, K. Arnold, R. Fischer, D. E. Resasco, M. Kappes, *Journal of Physical Chemistry B* **2005**, *109*, 10567.

[148] K. J. Ziegler, U. Rauwald, Z. N. Gu, F. Liang, W. E. Billups, R. H. Hauge, R. E. Smalley, *Journal of Nanoscience and Nanotechnology* **2007**, *7*, 2917.

[149] P. M. Ajayan, L. S. Schadler, C. Giannaris, A. Rubio, *Advanced Materials* **2000**, *12*, 750.

[150] J. N. Coleman, U. Khan, Y. K. Gun'ko, *Advanced Materials* **2006**, *18*, 689.

[151] M. J. Biercuk, M. C. Llaguno, M. Radosavljevic, J. K. Hyun, A. T. Johnson, J. E. Fischer, *Applied Physics Letters* **2002**, *80*, 2767.

[152] T. Kashiwagi, E. Grulke, J. Hilding, K. Groth, R. Harris, K. Butler, J. Shields, S. Kharchenko, J. Douglas, *Polymer* **2004**, *45*, 4227.

[153] S. Peeterbroeck, F. Laoutid, B. Swoboda, J. M. Lopez-Cuesta, N. Moreau, J. B. Nagy, M. Alexandre, P. Dubois, *Macromolecular Rapid Communications* **2007**, *28*, 260.

[154] J. Sandler, M. S. P. Shaffer, T. Prasse, W. Bauhofer, K. Schulte, A. H. Windle, *Polymer* **1999**, *40*, 5967.

[155] A. Allaoui, S. Bai, H. M. Cheng, J. B. Bai, *Composites Science and Technology* **2002**, *62*, 1993.

[156] B. X. Yang, K. P. Pramoda, G. Q. Xu, S. H. Goh, *Advanced Functional Materials* **2007**, *17*, 2062.

[157] T. V. Sreekumar, T. Liu, B. G. Min, H. Guo, S. Kumar, R. H. Hauge, R. E. Smalley, *Advanced Materials* **2004**, *16*, 58.

[158] S. Peeterbroeck, M. Alexandre, J. B. Nagy, C. Pirlot, A. Fonseca, N. Moreau, G. Philippin, J. Delhalle, Z. Mekhalif, R. Sporken, G. Beyer, P. Dubois, *Composites Science and Technology* **2004**, *64*, 2317.

[159] L. Liu, J. C. Grunlan, *Advanced Functional Materials* **2007**, *17*, 2343.

[160] C. Y. Tang, L. X. Xiang, J. X. Su, K. Wang, C. Y. Yang, Q. Zhang, Q. Fu, *Journal of Physical Chemistry B* **2008**, *112*, 3876.

[161] M. Moniruzzaman, F. M. Du, N. Romero, K. I. Winey, *Polymer* **2006**, *47*, 293.

[162] W. J. Boo, L. Y. Sun, J. Liu, A. Clearfield, H. J. Sue, M. J. Mullins, H. Pham, *Composites Science and Technology* **2007**, *67*, 262.

[163] Z. L. Wang, *Journal of Physics-Condensed Matter* **2004**, *16*, R829.

[164] Z. L. Wang, J. H. Song, *Science* **2006**, *312*, 242.

[165] U. Ozgur, Y. I. Alivov, C. Liu, A. Teke, M. A. Reshchikov, S. Dogan, V. Avrutin, S. J. Cho, H. Morkoc, *Journal of Applied Physics* **2005**, *98*.

[166] L. Spanhel, *Journal of Sol-Gel Science and Technology* **2006**, *39*, 7.

[167] Z. L. Wang, *Materials Today* **2007**, *10,* 20.

[168] U. Koch, A. Fojtik, H. Weller, A. Henglein, *Chemical Physics Letters* **1985**, *122*, 507.

[169] E. A. Meulenkamp, *Journal of Physical Chemistry B* **1998**, *102*, 5566.

[170] M. S. Tokumoto, S. H. Pulcinelli, C. V. Santilli, A. F. Craievich, *Journal of Non-Crystalline Solids* **1999**, *247*, 176.

[171] M. S. Tokumoto, S. H. Pulcinelli, C. V. Santilli, V. Briois, *Journal of Physical Chemistry B* **2003**, *107*, 568.

[172] M. S. Tokumoto, V. Briois, C. V. Santilli, S. H. Pulcinelli, *Journal of Sol-Gel Science and Technology* **2003**, *26*, 547.

[173] P. V. Kamat, B. Patrick, *Journal of Physical Chemistry* **1992**, *96*, 6829.

[174] S. Sakohara, L. D. Tickanen, M. A. Anderson, *Journal of Physical Chemistry* **1992**, *96*, 11086.

[175] P. Hoyer, H. Weller, *Journal of Physical Chemistry* **1995**, *99*, 14096.

[176] S. Sakohara, M. Ishida, M. A. Anderson, *Journal of Physical Chemistry B* **1998**, *102*, 10169.

[177] C. Reichardt, *Solvents and solvent effects in organic chemistry*, Wiley-VCH, Weinheim **2003**.

[178] E. Hosono, S. Fujihara, T. Kimura, H. Imai, *Journal of Sol-Gel Science and Technology* **2004**, *29*, 71.

[179] B. Cheng, E. T. Samulski, *Chemical Communications* **2004**, *8*, 986.

[180] A. Matsumoto, T. Ishikawa, T. Odani, H. T. Oikawa, S. Okada, H. Nakanishi, *Macromolecular Chemistry and Physics* **2006**, *207*, 361.

[181] A. van Dijken, E. A. Meulenkamp, D. Vanmaekelbergh, A. Meijerink, *Journal of Luminescence* **2000**, *90*, 123.

[182] A. van Dijken, E. A. Meulenkamp, D. Vanmaekelbergh, A. Meijerink, *Journal of Luminescence* **2000**, *87-9*, 454.

[183] R. D. Yang, S. Tripathy, Y. T. Li, H. J. Sue, *Chemical Physics Letters* **2005**, *411*, 150.

[184] M. V. Artemyev, A. I. Bibik, L. I. Gurinovich, S. V. Gaponenko, U. Woggon, *Physical Review B* **1999**, *60*, 1504.

[185] L. Guo, S. H. Yang, C. L. Yang, P. Yu, J. N. Wang, W. K. Ge, G. K. L. Wong, *Chemistry of Materials* **2000**, *12*, 2268.

[186] Y. Kojima, A. Usuki, M. Kawasumi, A. Okada, Y. Fukushima, T. Kurauchi, O. Kamigaito, *Journal of Materials Research* **1993**, *8*, 1185.

[187] M. Alexandre, P. Dubois, *Materials Science & Engineering R-Reports* **2000**, *28*, 1.

[188] E. P. Giannelis, *Advanced Materials* **1996**, *8*, 29.

[189] A. Clearfield, *Annual Review of Materials Science* **1984**, *14*, 205.

[190] D. Z. Sun, M. H. Wong, L. Y. Sun, Y. T. Li, N. Miyatake, H. J. Sue, *Journal of Sol-Gel Science and Technology* **2007**, *43*, 237.

[191] U. O. Koylu, G. M. Faeth, T. L. Farias, M. G. Carvalho, *Combustion and Flame* **1995**, *100*, 621.

[192] A. M. Brasil, T. L. Farias, M. G. Carvalho, *Journal of Aerosol Science* **1999**, *30*, 1379.

[193] H. Iba, T. Chang, Y. Kagawa, *Composites Science and Technology* **2002**, *62*, 2043.

[194] E. Chailleux, M. Salvia, N. Jaffrezic-Renault, V. Matejec, I. Kasik, *Smart Materials & Structures* **2001**, *10*, 194.

[195] G. K. Batchelor, *Journal of Fluid Mechanics* **1976**, *74*, 1.

[196] H. Shimizu, *Journal of Chemical Physics* **1962**, *37*, 765.

[197] H. Brenner, D. W. Condiff, *Journal of Colloid and Interface Science* **1974**, *47*, 199.

[198] W. B. Russel, D. A. Saville, W. R. Schowalter, *Colloidal dispersions*, Cambridge University Press, New York **1989**.

[199] A. Tuteja, M. E. Mackay, S. Narayanan, S. Asokan, M. S. Wong, *Nano Lett.* **2007**, *7*, 1276.

[200] F. M. van der Kooij, A. P. Philipse, J. K. G. Dhont, *Langmuir* **2000**, *16*, 5317.

[201] J. Liu, D. P. Cao, L. Q. Zhang, *Journal of Physical Chemistry C* **2008**, *112*, 6653.

[202] B. Ellis, *Chemistry and technology of epoxy resins*, Blackie Academic & Professional, London ; New York **1993**.

[203] P. Meakin, *Phys. Rev. Lett.* **1983**, *51*, 1119.

[204] M. Kolb, R. Botet, R. Jullien, *Phys. Rev. Lett.* **1983**, *51*, 1123.

[205] J. B. Xia, *Physical Review B* **1989**, *40*, 8500.

[206] S. Monticone, R. Tufeu, A. V. Kanaev, *Journal of Physical Chemistry B* **1998**, *102*, 2854.

[207] V. A. Fonoberov, A. A. Balandin, *Journal of Nanoelectronics and Optoelectronics* **2006**, *1*, 19.

[208] M. Silvander, G. Karlsson, K. Edwards, *Journal of Colloid and Interface Science* **1996**, *179*, 104.

[209] B. S. Kim, M. A. Islam, L. E. Brus, I. P. Herman, *Journal of Applied Physics* **2001**, *89*, 8127.

[210] D. O. Demchenko, L. W. Wang, *Physical Review B* **2006**, *73,* 155326.

VITA

Dazhi Sun received his Bachelor's and Master's degrees in chemical engineering from Tsinghua University (Beijing, China) in 2002 and 2005, respectively. He entered Texas A&M University in September 2005 for his Ph.D. in Materials Science and Engineering. His research interests include synthesis of inorganic nanostructures, colloidal dispersion, self-assembly, nanostructures for device applications, and polymer nanocomposites. He plans to work in academia after graduation. He likes swimming and watching Discover, National Geographic, and Science Channels in his spare time.

Dazhi Sun may be reached at Center for Functional Nanomaterials, Brookhaven National Laboratory, Upton, New York 11973, USA. His email address is dazhsun@gmail.com.